IMPROVED APPLICATIONS OF FILTERED RAYLEIGH SCATTERING

By

Chad Duane Carpenter

Dissertation
Submitted to the Faculty of
Graduate School of Vanderbilt University
in partial fulfillment of the requirements
for the degree of

DOCTOR OF PHILOSOPHY
in
Mechanical Engineering
March 31st, 2020
Nashville, Tennessee

Approved:

Robert W. Pitz, PhD
Joseph Wehrmeyer, PhD
Haoxiang Luo, PhD
Richard Peters, PhD
Alvin Strauss, PhD

DEDICATION

For the limitless support along this difficult path and always reminding me that "life is far too important to be taken seriously", I dedicate this to Jackie. I could not have asked for a better partner, travel companion, and best friend.

ACKNOWLEDGEMENTS

I would like to thank my advisor at Vanderbilt, Dr. Robert W. Pitz. Thank you for your guidance and flexibility in these works. You provided an environment that allowed us to run with our ideas and fail as many times as we needed to learn. I would also like to thank my fellow associates and friends at Vanderbilt: Darren Tinker, Garrett Marshall, Marsalis Pullen, and Harshini Devathi. Every one of you provided comradery, collaboration, and so much laughter through my time at Vanderbilt, and I cannot give enough praise for the teammates that you are.

I would also like to acknowledge all the sources for experimental and financial support on my research and time spent at Vanderbilt. Many thanks goes to Dr. Campbell D. Carter of Air Force Research Laboratory, Wright-Patterson AFB and Dr. Joseph A. Wehrmeyer of Arnold Engineering Development Complex for their support on this work through their advice and loan of equipment. Additional appreciation goes to the Air Force Office of Scientific Research and Dr. Chiping Li for the funding of my research (grant FA9550-15-0512). Of course, I would also like to thank Vanderbilt's Department of Mechanical Engineering for the opportunity and assistance through this process.

TABLE OF CONTENTS

LIST OF TABLES

LIST OF FIGURES

LIST OF COMMON VARIABLES

a	particle radius
A.U.	arbitrary unit
A_c	apparent contaminant area
A_f	flame area
CR	Contaminant Rejection filter
CW	continuous wave
D	mass diffusivity
d_c	apparent contaminant diameter
$\bar{F}_{j,k}$	flame image with background subtraction
$F_{j,k}$	flame image at pixel j and k
FRS	filtered Rayleigh scattering
FWHM	full-width half-max
$I(v)$	spectral intensity
I_0	incident light intensity
iCR	iterative Contaminant Rejection filter
iCR >> Med	iterative Contaminant Rejection filter followed by median filter
I_M	intensity of accumulated filtered Mie scattering
I_{max}	maximum particle intensity
I_R	intensity of accumulated filtered Rayleigh scattering
I_R / I_M	intensity ratio of filtered Rayleigh scattering to filtered Mie scattering
k	flame stretch
K	wavenumber
l	mean free path
Le	Lewis Number
L_f	filter size
m	index of refraction
M	molecular mass
N	total number density
ND_M	number density of particles for Mie scattering
ND_R	number density of gas for Rayleigh scattering
OD	optical density
P	pressure
PIV	particle image velocimetry
r	radial coordinate
$\bar{R}_{j,k}$	flame image with background subtraction
r_i	Rayleigh scattering distribution
$R_{j,k}$	reference image at pixel j and k
S^*	signal ratio for filtered Rayleigh scattering
SNR	signal-to-noise ratio
T	Temperature

TH	threshold
u_{nozzle}	Nozzle exit velocity
x	dimensionless size parameter
x_i	ith species mole fraction
y	Rayleigh scattering parameter (inverse Knudsen number)
z	axial coordinate

α	thermal diffusivity
δ	standard deviation
Θ	scattering angle
λ	light wavelength
λ	light wavelength
μ	average intensity
ν	centerline frequency
ρ_v	polarization ratio
σ_M	Mie scattering cross-section
σ_R	Rayleigh scattering cross-section
$\tau(\nu)$	iodine transmission
Φ	equivalence ratio

CHAPTER I

INTRODUCTION AND REVIEW OF PAST RESEARCH

Combustion remains a staple method of energy generation for many industries. The various applications result in a wide range of flame conditions such as laminar or turbulent flames as well as premixed or diffusion flames. In order to further our understanding of combustion, many non-intrusive optical diagnostic techniques have been developed to characterize the flames in terms of species concentrations, temperature, velocity, etc. However, each flame condition can present unique challenges for measuring particular flame characteristics.

Observing the temperature field of the flame structure can provide further insight into flame stretch and diffusion. Many methods have been developed for the thermometry of reacting flows, and laser Rayleigh scattering has been a common strategy due to the inherent high signal and reliable signal to temperature relation [1, 2]. However, some combustion fields are created inside metallic walls that can provide undesirable noise due to the incident light reflecting off the burner walls. For combustion of liquid fuels, the gaseous flow can contain unburnt fuel droplets that also produce intense scatter from the incident light. Additionally, some flows may intentionally possess solid particles that can be used for Particle Image Velocimetry (PIV) calculations. These particles, along with the liquid droplets and burner walls give off Mie scattering that is several orders of magnitude more intense than Rayleigh scattering. Mie scattering diminishes the quality of

images for Rayleigh scattering interpretation and can often saturate the pixels on a camera. Fortunately, filtered Rayleigh scattering (FRS) provides a method to mitigate the undesired Mie scattering in combusting fields [1-5].

A series of investigations were conducted on various aspects of the filtered Rayleigh scattering method. FRS was applied to steady, tubular flames as well as contaminant-laden turbulent flame kernels. Improvements were made on the experimental design, methods of experimentation, and FRS data processing. The remaining chapter provides further background into the application of filtered Rayleigh scattering and the flames analyzed by its application for these studies.

1.1 Filtered Rayleigh Scattering

The theory of Rayleigh scattering is applied to light reflection from bodies that are smaller than the wavelength of the light they are interacting with, such as gaseous molecules. The criteria for Rayleigh scattering is commonly defined as when the dimensionless size parameter, *x*, is much less than 1 as seen in Eq (1). In this equation, *a* is the spherical particle radius, λ_0 is the incident wavelength with respect to vacuum, and m_0 represents the refractive index of the surrounding medium. Gaseous vapor falls into this criterion while light scatter from larger liquid droplets or solid particles is observed through the theory of Mie scattering.

$$x = \frac{2\pi a}{\lambda_0 / m_0} \ll 1 \; for \; Rayleigh \tag{1}$$

The Rayleigh scattering regime has been utilized by Laser Rayleigh Scattering (LRS) to optically determine various gas properties such as pressure, temperature, and velocity [1, 2]. In this technique, a gas flow of interest is stimulated by a laser, and the

scattering light intensity is measured by a downstream detector, which is then related to a gas property. Only the measurement of temperature using Rayleigh scattering will be considered for the studies discussed in this paper. Pitz et al were the first to use Laser Rayleigh Scattering (LRS) for measuring temperature based on LRS spectral width [6] using the derived the relation between gas temperature, *T*, and total spectral intensity, *I(v)*, of Rayleigh scattering for low pressure or high temperatures often described as the kinetic regime such that $y = \lambda/2\pi l << 1$ where λ and *l* represent the wavelength and mean free path, respectively. Equation (2) describes this relation with *C* representing optical calibration, I_0 as incident intensity, *N* as total number density, x_i is the species mole fraction, σ_i is the Rayleigh scattering cross-section, and r_i is the scattering distribution for a particular i^{th} gas species. The scattering distribution is dependent upon the gas temperature, *T*, gas pressure, *P*, molecular mass, *M*, angle of observation relative to incident light, *Θ*, and centerline frequency, *v*. The Rayleigh profile can be computed by the Tenti S6 model [7]. An example of the Rayleigh profile of air at various temperatures is provided in Figure 1 along with the respective *y* values. For each Rayleigh profile computed, the Rayleigh cross-section must also be determined. Equation (3) can be used to determine the differential Rayleigh cross-section from wavelength, *λ*, molecular number density, *N*, depolarization ratio, ρ_v, and index of refraction, *m*, of the i^{th} species. McManus et al. [8] has experimentally confirmed the mole-fraction-weighted averaged FRS signal.

$$I(v) = CI_oN\sum_i x_i\sigma_i r_i(T, P, M_i, \theta, v) \tag{2}$$

$$\sigma_i = \frac{4\pi^2(m_i - 1)^2}{\lambda^4 N^2} \sin^2\theta \, \frac{3}{3 - 4\rho_v} \tag{3}$$

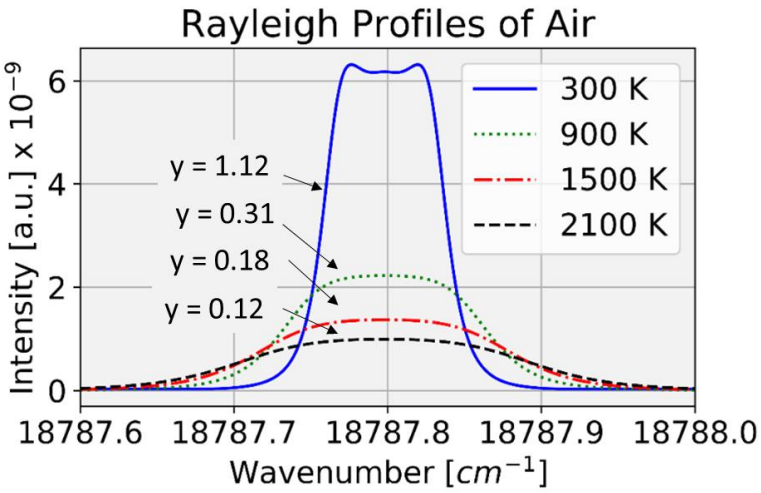

Figure 1: Rayleigh profile of air at various temperatures at 90° observation when stimulated by 532 nm light with FWHM = 0.003 cm^{-1}

When laser Rayleigh scattering is applied to gaseous fields containing liquid droplets, solid particles, or metallic walls, intense Mie scattering can reach the downstream detector and saturate the detector pixels. Fortunately, the Mie scattering from these artifacts maintains a spectral width similar to that of the incident light. For example, Mie scattering will have a full-width half-max (FWHM) of 0.003 cm^{-1} if the particles are stimulated by a laser with a FWHM of 0.003 cm^{-1}. While Mie scattering maintains similar line-width, Rayleigh scattering is broadened relative to the incident light due to the random thermal motion of the gas. As seen in Figure 1, the LRS spectrum of 300 K air at 90° scattering has an approximate FWHM of 0.05 cm^{-1} when stimulated with 0.003 cm^{-1} and continues to broaden as temperature rises. This difference in spectral width between the Mie scattering and Rayleigh scattering enables a spectrally thin notch filter to block out the Mie scattering light while allowing the broadened Rayleigh scatter to pass through.

Molecular gases can produce such thin notch filters at particular wavenumbers due to molecular absorption. These molecular filters can be placed just upstream of the detector in order to filter out the Mie scattering while allowing Rayleigh scattering to reach the detector. For example, if the incident light is produced by a frequency doubled Nd:YAG laser (532 nm), a molecular iodine filter would be used to absorb the Mie scattering. Forkey et al. [9] established a model for I_2 transmission near the 532 nm wavelength and an example is provided in Figure 2 below. Ultraviolet FRS has been conducted using mercury filters [10], but this method was not considered for the investigations in this paper.

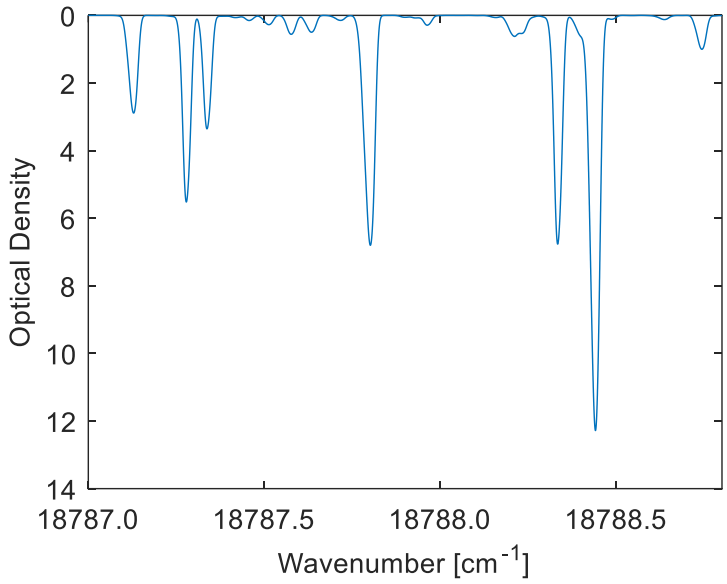

Figure 2: Forkey's model of molecular iodine transmission (1 Torr, 85°C)

As seen in Figure 2, several bands of high optical density (OD) are available for filtering Mie scattering. When the centerline of the incident light is tuned at or near the center of these optically thick bands, the intensity captured by the detector, $S(v)$, is a convolution of the scattering light, $I(v)$, and the molecular transmission, $\tau(v)$. This

convolution is depicted in Figure 3 and further described in Eq (4). One can see that if the molecular filter has adequate optical density and the band of optical density is spectrally wider than the Mie scattering profile, the Mie scatter intensity is completely absorbed while the broadened Rayleigh scatter, outside of the optically thick transmission band, passes through to the detector.

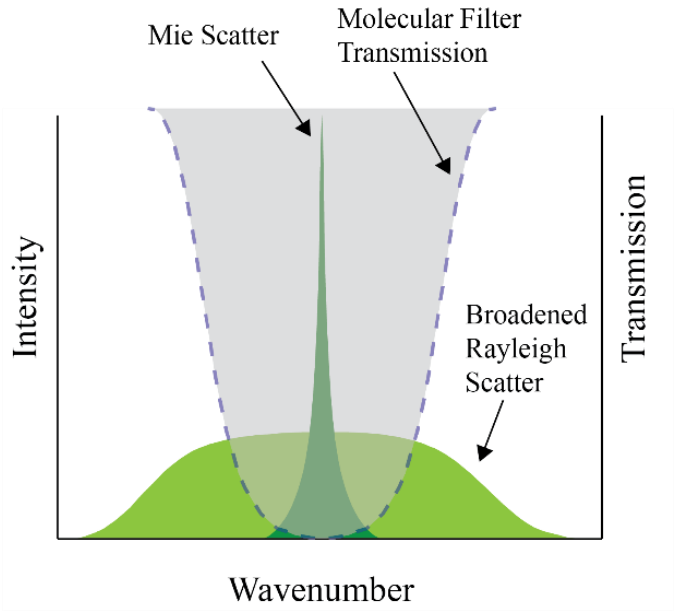

Figure 3: Qualitative example of the Mie scatter, Rayleigh scatter, and molecular filter transmission

$$S(v) = \int_{-\infty}^{+\infty} I(v')\tau(v - v')dv' \tag{4}$$

However, the intensity captured by the detector also needs to be adjusted by the dark background signal, $B_{j,k}$. In order to remove the constraints of optical constants, the signal detected in a flame image, $F_{j,k}$, can be normalized by a reference signal at known conditions, $R_{j,k}$, (typically ambient room temperature and pressure). The normalized signal, S^*, can be calculated on a per pixel basis using Eq. (5) where j and k represent the corresponding pixels.

$$S^* = \frac{F_{j,k} - B_{j,k}}{R_{j.k} - B_{j,k}} \tag{5}$$

Through the combination of Eq (2) – Eq (5), the relation of normalized intensity and temperature can be derived as seen in Eq (6). An example of the relation is provided in Figure 4 for a temperature range of N_2.

$$S_{j,k} = \frac{F_{j,k} - B_{j,k}}{R_{j,k} - B_{j,k}} \propto \frac{T_R}{T_F} \sum_i x_i \sigma_i \int_{-\infty}^{+\infty} r_i(T_F, v') \tau(v - v') dv \tag{6}$$

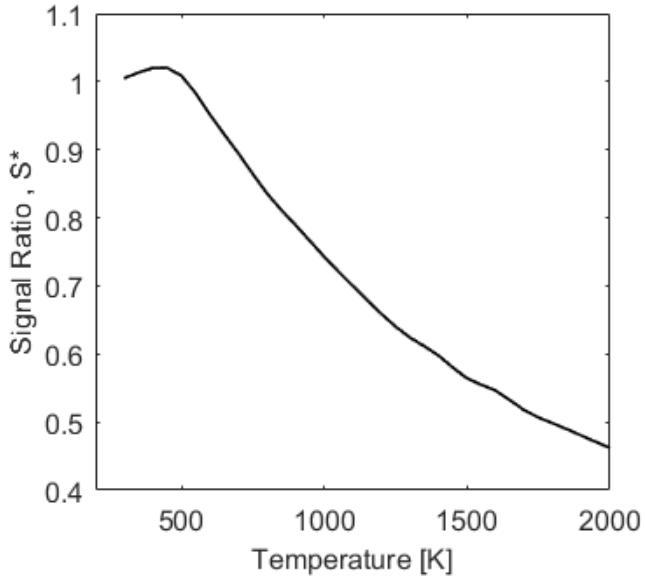

Figure 4: FRS Signal Ratio vs. Temperature Relation for N_2

A quick analysis of the derivation reveals that the FRS signal is nearly inversely related to temperature with some additional non-linear affects due to the temperature dependence in the Rayleigh distribution. Additionally, the relation is dependent upon the choice of transmission band of the molecular filter as each one has a different maximum optical density and spectral width. The relation is also dependent upon the laser centerline placement with the transmission band as well as the molecular filter conditions [11, 12].

As mentioned before, the Mie scattering profile is dependent upon the spectral width of the incident light. For a seeded, pulsed Nd:YAG, the spectral width is approximately 0.003 cm^{-1} for current manufacturers. Since these lasers are not spectrally pure (e.g. spectrally purity ~ 0.999), the realistic maximum optical density of the molecular filter is less than the values predicted by Forkey's model (e.g. a maximum OD of 3 is achieved when Forkey's model predicts an OD of 6). Fortunately, prior studies have increased spectral purity of pulsed Nd:YAG lasers by use of an external Fabry-Perot etalon [13, 14]. The external etalon is placed downstream of the laser and acts as a band-pass filter. To achieve the desired wavelength of the band-pass filter effect, the etalon face is rotated relative to the laser direction, which simulates a wavelength tuning of the etalon due to the change of distance that the light travels through the etalon.

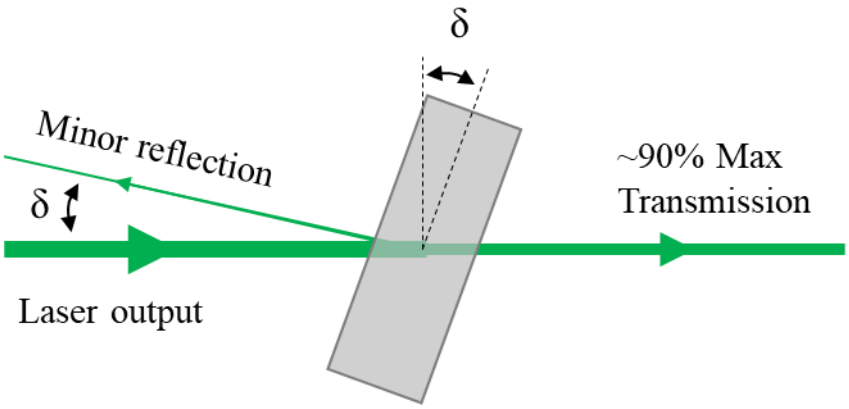

Figure 5: Rotated Etalon to Improve Spectral Purity

This increase in spectral purity of the incident light leads to a decrease of spectral width for Mie scattering that renders the molecular filter more effective in preventing Mie scattering from reaching the detector. For example, if the use of the external etalon improves the optical density from 3 to 4, then 10x less Mie scattering is detected.

External etalons may not be required to improve the spectral purity for some lasers. When an inherently high spectral purity laser is used, such as a tuneable continuous wave laser, the theoretical optical density, predicted by Forkey's model, is approached [13]. Additionally, more spectrally pure laser can have less broadband light that would leak through a molecular filter. A qualitative example of the full-width half max (FWHM) reduction as well as the broadband light reduction is provided in Figure 6. One can see that as both FWHM and broadband decrease, less light energy exists outside the transmission band of a molecular iodine filter.

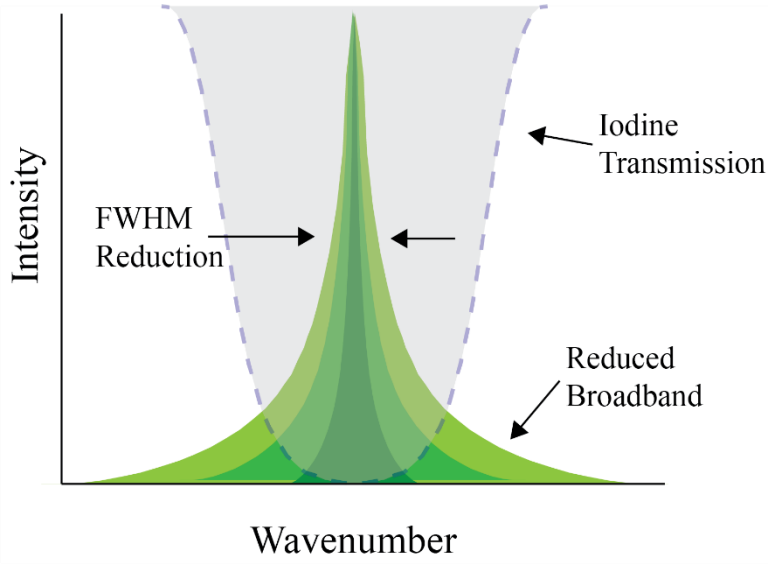

Figure 6: Reduced Broadband and Full-Width Half Max with Increased Spectral Purity

In the first investigation discussed, FRS is applied with a continuous wave laser in order to provide the high spectral purity incident light to enable low wall scatter noise detected inside of the burner. The continuous wave FRS was applied to a lean, premixed H_2-air tubular flame at $k = 200s^{-1}$ and $\Phi = 0.25$ where k and Φ represent the flame stretch and equivalence ratio, respectively. Further details of tubular flames and previous applicable investigations of them are discussed in sub-chapter 1.2. The results of the FRS

data is compared to the previous Raman spectroscopy data and numerical simulations. Additional measurements of the axial structure of the tubular flame were also achieved using continuous wave FRS. An inherent advantage of using continuous wave incident light on a steady flame is the low power needed to achieve an integrated signal as long as the camera gate can be adjusted accordingly. In this study, the continuous wave light was formed into a planar sheet to observe the axial structure. Prior attempts of achieving planar measurements with pulsed laser methods have resulted in damaged windows due to the rapid nanosecond scale pulse (and high power) of pulsed Nd:YAG lasers. The investigation demonstrates the first known use of continuous wave FRS for temperature measurement in a flame as well as the first FRS application for temperature measurement of a cellular, tubular flame.

Pulsed lasers have been used exclusively with past FRS experiments. While some advancements of the pulsed FRS strategy have been made, such as the use of an external etalon, an adequate comparison has not been made between the pulsed strategies. Considering the addition of another FRS strategy, the continuous wave FRS that is discussed later, the FRS methods would benefit from a comparative analysis. Three methods were applied to the same cellular, tubular flames for observation in a steady flame subject to wall scatter. Discussion is provided on the experimental advantages and peculiarities of three filtered Rayleigh methods: pulsed FRS, pulsed FRS with an external etalon, and continuous wave FRS.

The remaining investigations pivot the perspective to FRS applications on contaminant-laden flows. FRS measurements were attempted on turbulent flame kernels with the objective of obtaining simultaneous temperature and velocity fields using

simultaneous FRS and PIV. However, difficulties were experienced with large contaminants in the flow producing intense Mie scattering prior to attempting any PIV seeding. The intense Mie scattering severely reduced the data quality from the raw images obtained. Fortunately, digital image processing provides a great tool to reduce in the impact of Mie scattering. A new digital filtering method was developed to specifically mitigate the Mie scattering captured in the images and greatly increase the data quality. Sub-chapter 1.3 provides more insight into the digital filtering previously attempted with filtered Rayleigh scattering.

The trouble with the contaminated flow discussed prior motivated a final study into a thorough analysis of FRS experimental design, specifically for experiments that anticipate particles or droplets in the flow. A survey of the FRS literature results in poorly defined criteria for successful FRS measurements that are subject to Mie scattering. A final investigation was conducted into the relative filtered intensities for Rayleigh scattering and Mie scattering for various particle size and number densities. Anticipated intensity ratio values were determined from the Rayleigh and Mie scattering theoretical models, and adequate optical density was determined for a range of conditions and experimental considerations. With the necessary concepts of filtered Rayleigh scattering already discussed, a more developed background on Mie scattering is provided in sub-chapter 1.4

1.2 Tubular Flames

Laminar flames are often studied, for ease of experimentation or simulation, as the first step in understanding further complex conditions. Fortunately, some steady,

laminar flames can be placed in configurations that stress phenomena often seen in turbulent or unsteady flames. Tubular flames offer such a configuration where flame stretch, often seen in turbulent flames, is observable at steady-state conditions [15]. Additionally, the knowledge of diffusional properties and their influence on preferential diffusion can be tested in tubular flames, both experimentally and numerically [16-22]. Unfortunately, some past temperature measurements of lean, premixed H_2-air tubular flames do not agree with numerical simulations [23-24].

Tubular flames are created using a tubular burner that contains an axisymmetric, inward facing nozzle to create an axisymmetric flow with exhaust ports at the top and bottom of the burner. A schematic of the burner and a geometric reference of the flow is provided in Figure 7. Reactants, such as hydrogen and air, are mixed upstream to deliver a premixed combustible flow at the center of the burner axis. Additional inward facing co-flow nozzles complement the premixed reactants on the top and bottom of the burner. The co-flow is matched with the same flow velocity as the reactant flow to prevent mixing of the two flow layers. The co-flows also provides an insulation layer between the inner combusting mixture and the metal burner in order to keep the burner at reasonable temperatures. Water is supplied through an open circuit water jacket around the burner for further cooling needs.

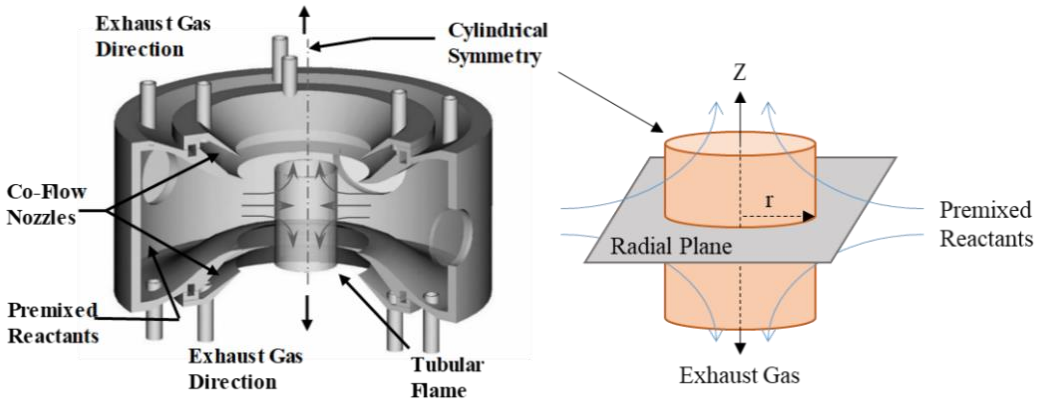

Figure 7: Tubular Burner

As seen in Figure 7, the premixed reactants exit the inner nozzle at a horizontal, radial plane denoted by *r* in the figure. The flowing reactants form a stagnation point at the central axis, labeled as *z*, before flowing out the top or bottom exhaust port. The gas velocity at the nozzle exit is dictated by the desired flame stretch. Flame stretch (*k*) is defined as the change in flame area over time (*dA/dt*) divided by the unit area (*A*) as seen in Eq (7). The flame stretch for an axisymmetric flow can be further described with a nozzle exit velocity (u_{nozzle}) and nozzle radius (*R*) for radius of interest (*r*) with $0 < r < R$ [16]. As the radius (*r*) approaches 0, the cosine operator in Eq (7) can be approximate as 1 resulting in the simplification of flame stretch on the right of Eq (7).

$$k = \frac{1}{A}\frac{dA}{dt} = |u_{nozzle}|\frac{\pi}{R}\cos\left(\frac{\pi}{2}\frac{r^2}{R^2}\right) \cong |u_{nozzle}|\frac{\pi}{R} \tag{7}$$

Tubular flames are commonly operated at high stretch values (k >100 s^{-1}) in order to avoid buoyancy affecting the flame structure. However, the fuel choice and equivalence ratio (Φ) of the premixed flow can also influence the flame structure. For example, a lean, premixed CH_4-air tubular flame exhibits a tangentially continuous flame structure while a lean, premixed H_2-air flame exhibits a cellular structure [25].

Schematics of these flame structures are provided in Figure 8. The cellular structure occurs in flames where the Lewis number (*Le*), ratio of the mixture thermal diffusivity (α) to the limiting reactant's mass diffusivity (D), is less than one (e.g. $Le = \alpha/D < 1$).

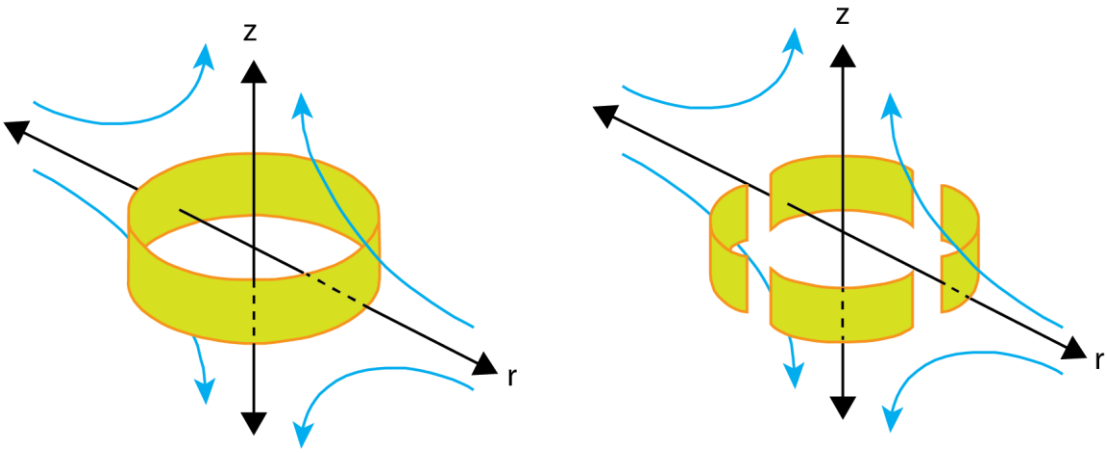

Figure 8: Tubular flames and Cellular Formation

The cellular structure is due to the preferential diffusion occurring in the tubular flames. For premixed CH_4-air flames, mild preferential diffusion occurs at some conditions, but wrinkles in the continuous CH_4-air flame are observed [25, 26] instead of the cellular nature of H_2-air flames. For lean, premixed H_2-air flames, the lighter hydrogen molecules are capable of diffusing faster than the larger oxygen and nitrogen molecules. For analysis purposes, the cellular flames are often analyzed across two radial lines: Reaction Zone and Extinction Zone. These particular radial lines have been superimposed on a chemiluminescence image of a lean, premixed H_2-air flame at $k=200s^{-1}$ and $\Phi=0.25$ [27] in Figure 9. The reaction zone is a radial profile across the center of a curved flame cell while the extinction zone distinguishes the radial profile between flame cells.

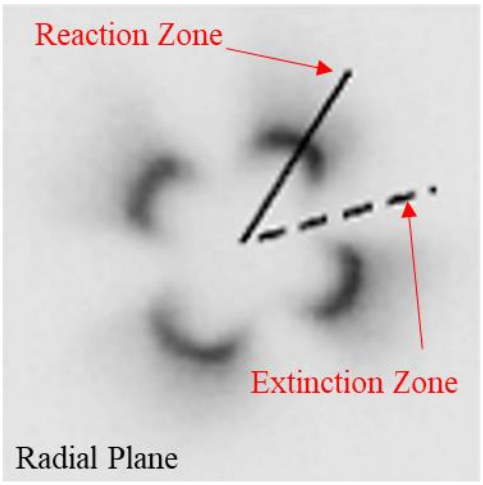

Figure 9: Reaction Zone and Extinction Zone of Cellular Flames in Tubular Burner

While distinct cells of chemiluminescence are observed, the areas between the cells (e.g. extinction zones) are not void of reactions or high temperature. Hall and Pitz [23] used Raman spectroscopy to measure the species and temperature of lean, premixed H_2-air flames at $k=200s^{-1}$ and $\Phi=0.25$. These results were then paired with direct numerical simulation (DNS) of the same conditions [24, 28] using the Burke mechanism [29]. The temperature results have been reproduced in Figure 10. The 4-cell structure can be clearly seen in the 4 lobes of the temperature profile. In between the lobes, high temperatures remain although slightly lower than the peak temperatures seen in the lobe centers. However, the numerical simulation under predicts the peak temperature of the lobes by approximately 200 K.

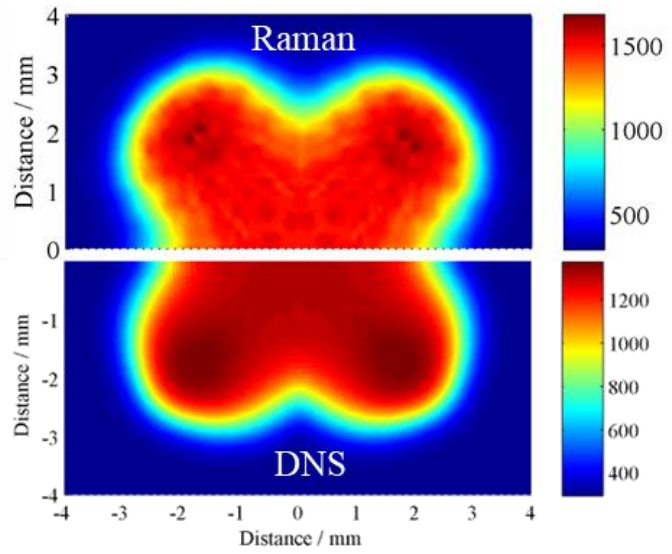

Figure 10: Comparison of Raman Spectroscopy and Direct Numerical Simulation Temperature Data reproduced from [23,24]

The discrepancy in temperature between the Raman and DNS data leads to questions of data validation and possible sources of noise or error. The preferential diffusion is these cellular flames is highly sensitive to the diffusional constants and reaction rates used for simulations. Meanwhile, the tubular burner can provide a highly reflective inner-surface that could lead to laser diagnostic noise.

The results of the tubular flame measurement are found in CHAPTER II. A tubular burner produces a steady flame without any particle or droplet obstructions in the flows. The remaining sub-chapters describes background for post-processing turbulent flame FRS images with particular interest in removing Mie scatter through digital image processing as well as theoretical calculations needed for improved FRS experimental design when particles or droplets are expected in the flow.

1.3 Digital Image Processing

Processing optical diagnostic images using various digital filters is a common practice to reduce the noise in cameras, detectors, and light sources [30]. The application

of digital filters on images obtained from combined PIV and FRS experiments presents unique challenges to the digital filtering process. Ideally, the presence of PIV particles on FRS images is reduced or completely removed while not modifying the underlying gas temperature profile (e.g. remove the particles without smearing the flame). For considerations of maintaining flame structure, non-linear methods are typically used for their edge-preserving capabilities [30-33].

In some prior FRS experiments, the observed flow contained Mie scattering that was too intense to be completely filtered out by the molecular filter. Most and Leipertz conducted combined PIV and FRS on a lean, turbulent CH_4-air V-flame [34]. However, some of the seeding PIV particles leaked through to the FRS detector. In order to mitigate the apparent presence of the particles, a 7x7 digital median filter was applied to the images. The footprint of the particles were reduced, but not completely removed from the images. For median filtering, a window size (odd number ≥ 3) is chosen around a central pixel. The central pixel value is placed into an array along with the neighboring pixel values (e.g. a 3x3 window leads to 9 total pixel values). The median of this array replaces the original central pixel value [35]. A simplified example of median filtering is provided in Figure 11.

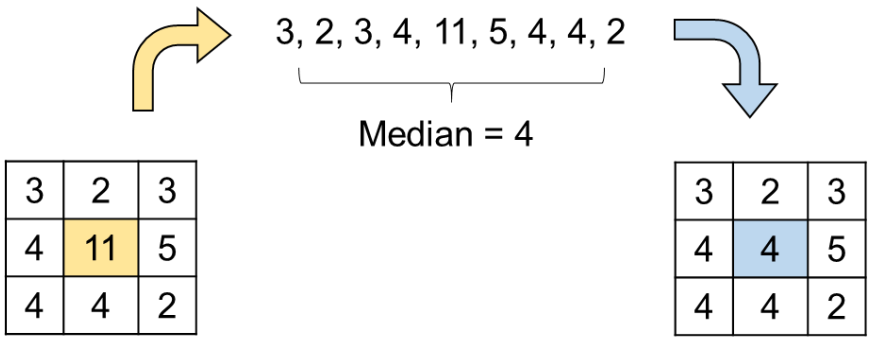

Figure 11: Example of Median Filtering

McManus and Sutton experienced similar Mie scattering from PIV particles reaching an FRS detector [36]. The images were processed in a like fashion with a digital median filter as well as a wavelet-denoising filter. Wavelet denoising or wavelet thresholding has been used to remove Gaussian noise while preserving edges in images [37,38]. Wavelet denoising occurs in three steps: wavelet transform, thresholding, inverse wavelet transform where the type of wavelet and level of thresholding is dependent on the expected noise of the image. The noise is thoroughly reduced, but the particle's influence still remains. A better strategy for mitigating the presence of contaminants in FRS images is needed.

Unfortunately, the applications of these digital filters on filtered Rayleigh scattering have not been analyzed for the effects on the flame structure nor have they related the filter size to applicable physical dimensions like particle diameter. Non-linear digital filters, like median filters, do a better job at preserving edge features in images compared to a linear filter, but some edge smoothing does occur. Additionally, the wrinkling inside of a flame will likely be filtered and smoothed due to having less severe intensity gradients that a filter could interpret as noise. Filters are often implemented in spatial terms such as the 3x3 window described in Figure 11. However, expressing a filter

size in these terms leaves little relation to the structures in the image such as a particle diameter or flame thickness.

Additional digital filtering strategies can also be applied and compared to the more common median filter in terms of reducing contaminant presence. For example, a weighted median filter [39] can be implemented similar to the median filter, but each pixel can be assigned a relative weight coefficient. The relative weights can be assigned as a constant, systematic application (e.g. the central pixel has a coefficient of 1 while the neighboring pixels have coefficients of 2). The relative weights can also be assigned conditionally such assigning lower coefficients to pixels that contain intensities that are too high (unexpected intensities from particle Mie scattering).

A digital filtering strategy was developed specifically for contaminant rejection based on the concept of the weighted median filter. In this strategy, pixel values that were associated with high intensities from contaminants were ignored from the determination of median values (e.g. assigned a weighted value of zero). Two versions of the filter were created: one version to substitute for the median filter and another version that could be processed iteratively and prior to traditional median filtering.

1.4 Mie scattering

The calculation of Rayleigh scattering has been discussed in Chapter 1 along with the effects of the molecular iodine filter. However, the calculation of Mie scattering needs to be addressed. Mie [40] and Debye [41] published the initial solutions to Mie scattering with van de Hulst [42] containing the common notation used in Mie scattering calculations. Equation (8) describes the intensity of scattered unpolarized light, I, as a function of scattering angle, Θ, where I_0 represents the incident light intensity, r is

distance from the center of the sphere, and K is the wavenumber. The numerator term in Eq (8) represents the average of the intensity from parallel polarized light, i_1, and perpendicular polarized light, i_2. If the incident light is polarized, then only the respective i_1 or i_2 is needed in the calculation.

$$I(\theta) = I_0 \frac{1/2(i_1 + i_2)}{K^2 r^2} \tag{8}$$

The intensity parameters, i_1 and i_2, are described in Eqs (9) and (10) where the infinite series terms inside the absolute value bracket are commonly referred to as the amplitude functions, $S_1(\Theta)$ and $S_2(\Theta)$.

$$i_1 = \left| \sum_{n=1}^{\infty} \frac{2n+1}{n(n+1)} (a_n \pi_n + b_n \tau_n) \right|^2 \tag{9}$$

$$i_2 = \left| \sum_{n=1}^{\infty} \frac{2n+1}{n(n+1)} (a_n \tau_n + b_n \pi_n) \right|^2 \tag{10}$$

The calculation of the intensity parameters, i_1 and i_2, are done so following methods used by Mätzler [43] whose MATLAB algorithms have been converted to Python which has been provided in Appendix B. The maximum number of terms, n_{max}, in the infinite series was limited by the size parameter, x, described in Eq (11) as suggested by Bohren and Huffman [44] where n_{max} is rounded to the closest integer.

$$n_{max} = x + 4x^{1/3} + 2 \tag{11}$$

The definitions of π_n, τ_n, a_n, and b_n are provided in Eq (12) – Eq (15). Both π_n and τ_n are dependent upon the cosine of the scattering angle as seen in Eq (12) and Eq (13) where the $P_n(\cos \Theta)$ is a Legendre polynomial fully described in [45]. As seen in Eq (14) and

Eq (15), spherical Bessel functions $\psi(x)$ and $\psi(y)$ along with its derivative are used to calculate the a_n and b_n coefficients.

$$\pi_n(\cos\theta) = \frac{1}{\sin\theta} P_n^1(\cos\theta) \tag{12}$$

$$\tau_n(\cos\theta) = \frac{d}{d\theta} P_n^1(\cos\theta) \tag{13}$$

$$a_n = \frac{\Psi'_n(y)\Psi_n(x) - m\Psi_n(y)\Psi'_n(x)}{\Psi'_n(y)\zeta_n(x) - m\Psi_n(y)\zeta'_n(x)} \tag{14}$$

$$b_n = \frac{m\Psi'_n(y)\Psi_n(x) - \Psi_n(y)\Psi'_n(x)}{m\Psi'_n(y)\zeta_n(x) - \Psi_n(y)\zeta'_n(x)} \tag{15}$$

In these equations, x takes a similar form as described in Eq (1) although often described in wavenumbers such that $x = ka$, while y takes a similar form as $y = mka$. One can now see how the index of refraction, m, influences the determination of the Mie scattering intensity. For further description of Mie scattering derivation, see [42].

1.5 Objective of Study and Method of Presentation

The objectives of this study is to improve the applications of filtered Rayleigh scattering through experimental design of FRS (CHAPTER IV), experimental methods of FRS (CHAPTER II), and data processing of FRS (CHAPTER III). Initial experiments began with applying a new FRS method, continuous wave FRS, and comparing it to two other pulsed FRS strategies with and without an external etalon. FRS measurements were taken of a lean, premixed H_2-air cellular, tubular flame that have been previously studied in experiments and simulations, which provided a good basis for comparison. These various strategies applied different levels of spectral purity and Mie scattering rejection that led to a quality comparison of data and difficulty of experimentation. Additionally,

the axial structure of the cellular, tubular flame was assessed for the first time. The results of this investigation are found in CHAPTER II.

Experiments were conducted on turbulent flame kernels with the hopes of capturing simultaneous velocity and temperature fields using particle image velocimetry (PIV) and FRS. However, difficulty with large contaminants and Mie scattering intensities led to poor quality data. These difficulties led to an investigation of the digital image processing of FRS images, particularly those that contain apparent Mie scattering. A digital filtering method was developed that significantly reduced the presence of contaminants and their influence on anomalous temperature calculations. The description of the digital filter and results are found in CHAPTER III

An additional investigation was conducted into the major factors of PIV particles' influence on FRS measurements. While some relatively successful PIV and FRS experiments have been conducted before, the necessary quality of Mie scattering rejection has not been investigated. Calculations of Rayleigh scattering, Mie scattering, and iodine transmission were conducted to establish the relative intensities of the filtered Rayleigh scattering and filtered Mie scattering in order to provide guidance on PIV and FRS experimentation and the necessary optical density needed for various conditions. CHAPTER IV provides details and conclusions from the theoretical analysis of comparing simultaneous gaseous Rayleigh scattering and particle Mie scattering.

A summary of the investigations is provided in Figure 12 and a summary of the main objectives of each study are listed below. The numeric notation used for the

summaries represents the order of the following chapters. A concluding Chapter 5 highlights the main results and conclusions of each investigation.

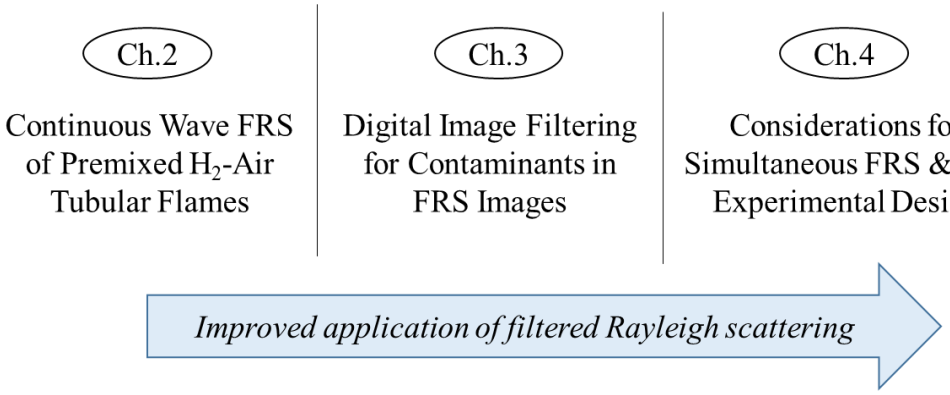

Figure 12: Summary of the investigations

Ch.2 Apply the first known use of continuous wave laser to filtered Rayleigh scattering for measurement of lean, premixed H_2-air flames previously studied by Raman spectroscopy and direct numerical simulation as well as obtain a measurement of the axial structure that has not been quantified by the previous methods mentioned. Additionally, compare the continuous wave FRS strategy to pulsed FRS strategies (with and without an external etalon) in terms of accuracy and operation.

Ch.3 Develop digital filtering methods for reducing or eliminating the presence of contaminant anomalies in filtered Rayleigh scattering images. Compare methods to traditional digital filtering methods, particularly those used in prior FRS studies. Analyze their effectiveness in terms of reducing Mie scattering interference, preserving derived characteristics of the flame, and overall image quality.

Ch.4 Develop an analysis method for comparing Rayleigh scattering and Mie scattering when filtered through an iodine cell of various optical densities. Determine the adequate optical density needed for simultaneous FRS and PIV experiments for a given range of particle conditions. Evaluate the effects of particle size and their

largest influence on Mie scattering reaching FRS detector. Provide suggestions on experimental design based on the results presented.

CHAPTER II

CONTINUOUS WAVE FITLERED RAYLEIGH SCATTERING OF PREMIXED H_2-AIR TUBULAR FLAMES

Filtered Rayleigh scattering can be conducted through various strategies with most methods utilizing a pulsed, Nd:YAG laser often equipped with a seed laser. The additional seed laser is directed into the Nd:YAG flash lamp cavity, and assists in narrowing the spectral linewidth of the laser pulse. In order to decrease the spectral linewidth further, external etalons have been placed downstream of the laser in order to act as a bandpass filter of the incident light before reaching the gas flow of interest [13]. The thinner linewidth enables for effective absorption of Mie scattering rejection by the iodine filter. Fortunately, other solutions exists for achieving more spectrally pure incident light such as continuous wave lasers.

Continuous wave lasers typically have higher spectral purity than pulsed lasers even when external etalon are used, and some experiments have shown that the use of continuous wave lasers approach the maximum absorption of Mie scattering in the molecular iodine filter [13]. However, prior studies have only used continuous wave lasers to validate the I_2 optical density, and continuous wave lasers have not been used for filtered Rayleigh scattering measurements. The experiments in this chapter describe the investigation of using a continuous wave laser for FRS measurements as well as

comparing the data quality to that of pulsed lasers, with and without an external etalon. The FRS strategies are applied to tubular flame conditions that have been studied previously through Raman spectroscopy and direct numerical simulation. The prior data provides a baseline for accuracy of the methods used. Additionally, the FRS methods can be compared for experimental ease and utility. The other advantage of using a continuous wave laser is the rate of energy supplied. A pulsed Nd:YAG laser will deliver the light energy within a 10 ns pulse while a continuous wave laser has a steady, power controlled output. With this steady output, the power through the burner windows can be reduced while the camera exposure time can be increased to compensate for the lower power. This enabled the use a vertical, planar laser sheet produced by the continuous wave laser for axial measurement of the tubular flame. Prior personal attempts with pulsed laser resulted in damaged windows due to the high energy over the short 10 ns pulse needed for adequate signal to be detected on the camera. Below, the experimental setup, results, and conclusion are discussed.

2.1 Experimental Setup and Methods

As mentioned earlier, the different FRS strategies used result in varying levels of I_2 optical density. The maximum optical density of each strategy was measured using the optical configuration given in Figure 13. The lasers were reduced to a lower power setting and tuned to 18787.798cm^{-1} which is the major transition R134(36,0)/P83(33,0) of $B(^3\Pi_{0+u}) \leftarrow X(\,^1\Sigma_g^+)$ electronic system of I_2 [9]. The focused beam was expanded into an approximate 1-inch wide collimated beam before passing through the iodine cell. Downstream of the iodine cell, the collimated beam was focused back down and passed through interchangeable neutral density (ND) filters before reaching a fast photodiode

sensor. This configuration allows avoids saturating the iodine cell with too much focused light as well as the easy adaptation of absorption through the iodine cell.

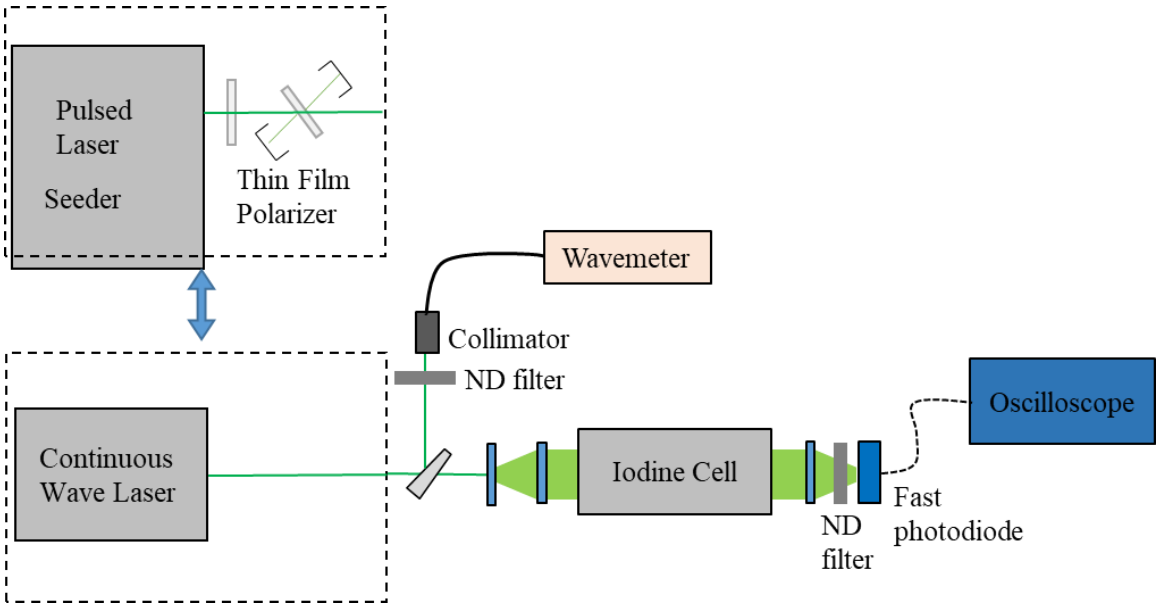

Figure 13: Optical configuration of optical density measurement for the interchangeable pulsed or continuous wave laser.

For the pulsed laser configuration, a maximum optical density of 3 was measured without an etalon while the use of an external etalon produced a maximum optical density of 4. When the continuous wave laser was placed into the configuration (without the half-wave plate and thin film polarizer), the maximum optical density measured was 6. However, the measurement was limited by the available neutral density filters on hand such that a greater OD could have been measured if more neutral density filters with better resolution were available. It is believed that the optical density approached that of the theoretical maximum optical density like that measured in [13]. A plot of the optical density for each method applied is provided in Figure 14.

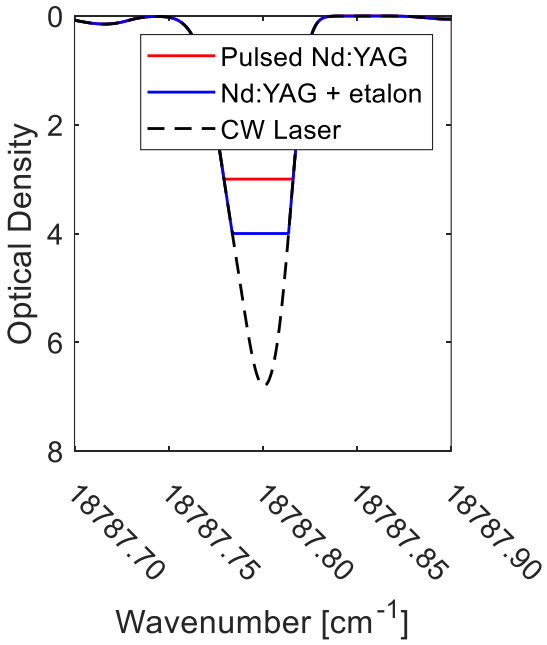

Figure 14: Variation of Optical Density through Different FRS Methods

The flames created for the tubular burner experiments were done so inside a tubular burner previously shown in Figure 7. The dimensions of the burner nozzles along with the flow conditions are provided in Table 1 below. These conditions match those conducted in [23, 24] where prior Raman spectroscopy data and direct numerical simulation data were obtained.

Table 1: Tubular Burner Dimensions and Flow Conditions

Parameter	**Value**
Outer Nozzle Diameter	12 mm
Nozzle Gap	8 mm
Air Flowrate	22 SLPM
H_2 Flowrate	2 SLPM
N_2 Flowrate	24 SLPM
Global Equivalence Ratio	0.25
Lewis Number	0.324
Stretch Rate	200 s^{-1}
Pressure	1 atm

The optical setup for the FRS experiments was arranged such that the lasers used could be interchanged with minimal alteration of the optical apparatus as a whole. A schematic of the optical setup is provided in Figure 15. The lasers {1} used for the experiment include a diode-pumped solid-state Verdi V6 CW laser (0.00017 cm^{-1} or 5 MHz linewidth) and an injection-seeded, pulsed, Q-switched Nd:YAG laser (Continuum Powerlite Precision 8010) that was frequency doubled to produce 532 nm light (linewidth of 0.003 cm^{-1} or 90 MHz). Both lasers were tuned to 18787.798 cm^{-1} to coincide within an absorption band of the molecular iodine also known as the major transition R134(36,0)/P83(33,0) of $B(^3\Pi_{0+u}) \leftarrow X(\ ^1\Sigma_g^+)$ electronic system of I_2 [9]. When the pulsed laser was used, a combination of half-wave plate {2} and thin film polarizer {3} were used for power control while the continuous wave laser allowed for power control directly from the laser head. The energy for both lasers were appropriately modified to produce 40 mJ during the respective gate times. The air-spaced Fabry-Perot external etalon {10} manufactured by SLS Optics (high power coating and finesse of 23.5) was

only used for pulsed laser experiments. The etalon was mounted to a high-precision gimbal mount for fine resolution control of the etalon face angle with respect to the laser light axis. For all configurations, two low energy beams were pulled from the main incident light using a 5° wedge beam splitter {4}. One of these low energy beams was used to verify the laser centerline via a High Finesse WS-6UV wavemeter {9} while the other low energy beam was sent through a iodine cell 125 mm in length {6} to a fast photodiode {7} for I_2 transmission validation. The wavemeter has a resolution of 30 MHz (0.001 cm^{-1}) along with an absolute accuracy of 600 MHz (0.02 cm^{-1}). Based off the measurements from the wavemeter, the Verdi CW laser was frequently adjusted to be within ± 30 MHz (± 0.001 cm^{-1}) in order to prevent drifting over time [46]. The pulsed laser experienced no noticeable drift but was subject to pulse-to-pulse spectral variations that are described later. The remaining high-energy beam after the beam splitter was used to excite the gas of the combusting flow in the tubular burner. Images of the excited flame were captured on a PCO 2000 CCD camera (2048 x 2048 pixel) with a 532 nm ±2 nm band-pass filter {12}. Prior to reaching the camera, the scattered light was filtered through an ISSI iodine cell {11} that was 250 mm in length and temperature controlled to 85 C. Not shown in the schematic is the Coherent Field Max II power meter used to check the incident energy into the tubular burner prior to measuring. Additionally, Hastings flow meters were used to control the air, hydrogen fuel, and nitrogen co-flow rates. A summary of the equipment accuracy is provided in Table 2. A description of the FRS thermometry measurement uncertainty is provided in the results section below.

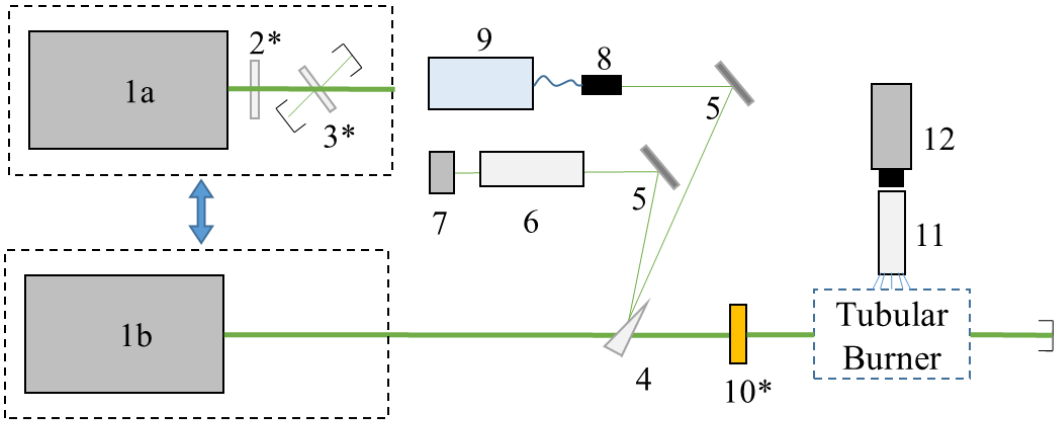

1	Pulsed Laser (a) or CW Laser (b)	7	Photodiode
2*	Half-wave plate	8	Collimator to fiber optic
3*	Thin film polarizer	9	Wavemeter
4	Wedge	10	Fabry-Perot Etalon*
5	Mirror	11	Iodine cell (250 mm), test
6	Iodine cell (125 mm), reference	12	CCD with 532 nm bandpass filter

Figure 15: Optical configuration of FRS strategies with {2},{3}, and {10} only be used during pulsed laser configuration

Table 2: Accuracy and Specification of Instrumentation

Measurement	**Instrument**	**Accuracy**
Volumetric flow rate – Air	Hastings Flow Controller (0-30 SLPM)	0.35% of reading
Volumetric flow rate – H_2	Hastings Flow Controller (0-3 SLPM)	0.05% of reading
Volumetric flow rate – N_2	Hastings Flow Controller (0-100 SLPM)	0.08% of full scale (30 psia)
Iodine Cell Temperature	PID with K-type thermocouple	± 1.1 °C
Wave Meter	High Finesse UV-6	1% of full scale
Power Meter	Coherent Field Max II	3% of reading + 0.005 FSN

The iodine cells used in this experiment are designed such that the temperature and pressure are not independently controlled. The internal pressure and amount of iodine is set prior to experimentation. During the experiments, the cell is heated to cause the

iodine to vaporize which also leads to increase of cell pressure. The cell pressure was not measured during experimentation, and the effects on the optical density for the results discussed here are considered negligible.

For all laser measurements, 100 images were averaged at each location. The CW laser images and pulsed laser images had an exposure time of 10 ms and 10 μs, respectively. The power of each laser was adjusted accordingly to allow 40 mJ of incident light energy per exposure for all laser methods. For the pulsed laser method utilizing a downstream etalon, the energy was measured post-etalon in order to account for the minor transmission loss (approximately 10% at proper tuning angle) through the etalon. For seeded, pulsed Nd:YAG lasers, it is not uncommon to have intermittent loss of frequency control and linewidth narrowing supported by the seed laser. When this occurs, the linewidth becomes significantly broader such that the FRS images are obviously brighter across the entire field of view due to less rejection of the iodine filter. These occurrences were removed from the measurement samples during post-processing of the data with simple algorithms to remove images with significantly higher average intensities.

An additional assumption was made to the Rayleigh cross-section in the combusting field measured. In previous Raman spectroscopy measurements for lean, premixed H_2-air tubular flames, the major species in the peak temperature zones were found to be N_2, O_2, and H_2O with their respective mole fractions given in Table 3. These species have also be measured or calculated for Rayleigh cross-section when excited with 532 nm light [47], which is also provided in Table 3. One can see that Nitrogen has a

substantially larger presence than the other species in addition to having the largest Rayleigh cross-section amongst the major species. This observation leads to the possibility of assuming the combustion field to be 'nitrogen dominant' in reference to the Rayleigh cross-section. The signal-to-temperature ratio can be determined when only considering the N_2 cross-section since influence by the remaining species' cross-section would be negligible. Figure 16 displays the relationship between signal ratio and temperature for the nitrogen dominant assumption as well as for all major species, which shows a minor shift in the relation. This assumption has been further validated by a previous study by Monje and Sutton [48] where FRS thermometry was conducted on lean, premixed hydrogen flames in this study. Only mild temperature differences were found through an equivalence ratio of 0.24 – 0.50 when comparing the nitrogen-dominant assumption against consideration for all major species. Further comparison of consideration of all major species and the nitrogen dominant assumption is provided in the proceeding results.

Table 3: The major species mole fraction in peak temperature zones [23] and respective Rayleigh cross-section (295K, 532 nm) [47]

Species	Mole fraction	Rayleigh cross-section [cm^2/sr]
N_2	0.73	6.24×10^{-28}
O_2	0.11	5.30×10^{-28}
H_2O	0.17	4.43×10^{-28}

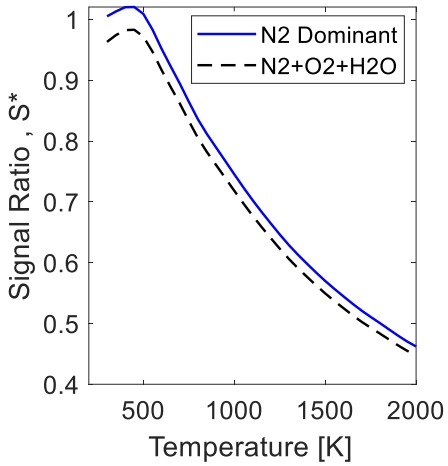

Figure 16: Comparison of Rayleigh Cross-section Influence on Signal Ratio for Lean H_2-Air Mixture

2.2 Continuous Wave FRS Results

The CW-FRS measurements were taken over an exposure time of 10 ms with 100 shots taken at each position along the flame. In order to gain insight into the axial structure of the cellular, tubular flame, the CW laser was used to form a planar laser sheet, 200 µm thick and 1000 µm high (Z direction in Figure 7 and Figure 8) into the cellular, tubular flame. The vertical structure of these flames has only be speculated or qualitatively observed, but not measured quantitatively. Figure 17 displays the planar temperature measurement. While curvature can be clearly seen in the radial direction on the prior chemiluminescence images in Figure 9, no significant curvature exists in the axial plane as seen in Figure 17. This demonstrates that buoyancy effects are negligible for high curvature values ($k > 100s^{-1}$). Slightly higher temperatures can be seen on the right side compared to the left depicting a good comparison the planar Reaction Zone and planar Extinction Zone, which are further discussed later. Measurement of the axial plane was not attempted with a pulsed laser method due to likelihood of window damage when passing through the high energy in the short exposure time for such planar measurements.

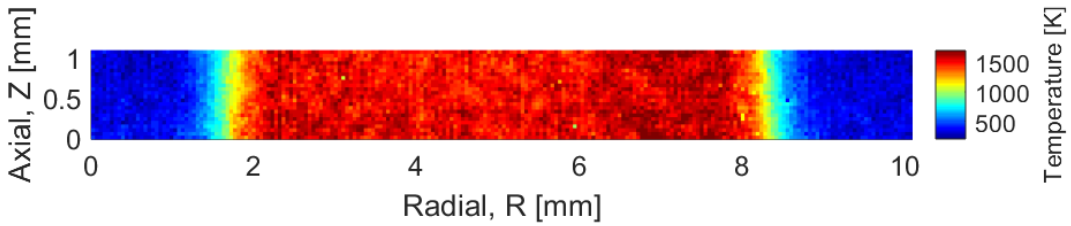

Figure 17: Temperature measurement of axial plane

For measurements in the radial plane, the CW planar sheet was raster scanned in increments of 200 μm until measurements of the Extinction Zone and Reaction Zone (previously labeled in Figure 9) were completed. Since no significant variation in temperature existed in the axial direction, the planar images were averaged to compute a 'line measurement' at each raster scanned location. The raster scan of the planar-averaged line measurements from the CW laser can be seen in Figure 18. In this image, the raster scanned direction, Radial – x, had a 0.2 mm resolution, while the laser line direction, Radial – y, had a spatial resolution of 0.06 mm per pixel. The 4-cell flame structure of the flame can be clearly seen in the image with the Reaction Zone and Extinction Zone labeled again for clarity. The right lobe in the cellular flame appears to be slightly off from symmetry. This aberration from symmetry is due to a small wire used to anchor the flame. The wire prevents the flame from rotating about the exhaust axis [23]. Otherwise, raster scanning across a steady flame would be impossible with a steadily rotating flame. Regardless of the wire presence, the symmetry about the top and bottom lobes is apparent.

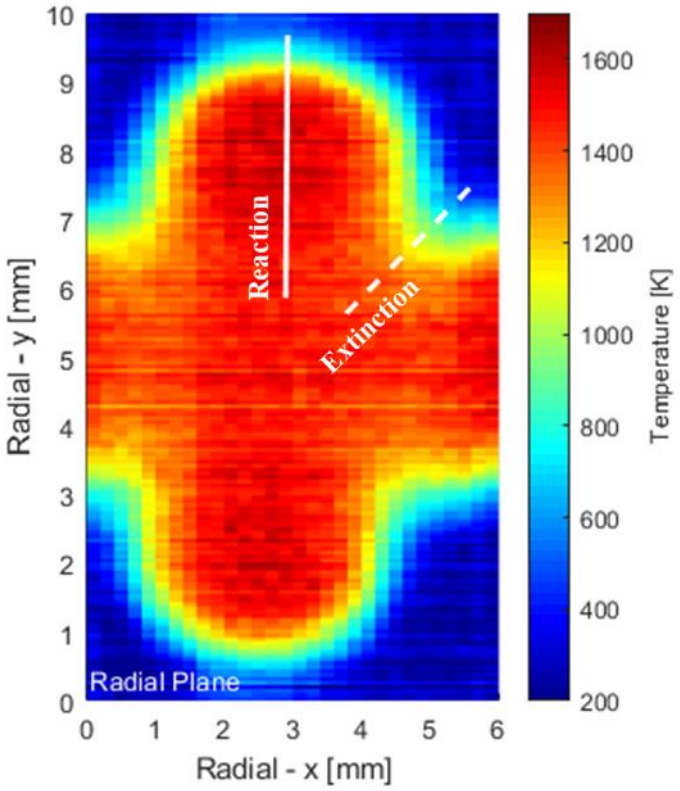

Figure 18: Raster scan of continuous wave laser line measurements in the radial plane (solid line represents 'Reaction Zone' and dashed line represents 'Extinction Zone')

For better understanding of the temperature field of the cellular flame as measured by filtered Rayleigh scattering, the temperature profiles measured along the radial Reaction Zone and Extinction Zone have been compared to the previous Raman spectroscopy data along with previous direct numerical simulation data. The comparison is provided in Figure 19. The FRS determined temperature agrees quite well with the previous Raman spectroscopy data throughout both the Reaction Zone and Extinction Zone. The peak temperatures in the Reaction Zone as determined by FRS were approximately 1575 K while the previous Raman strategy measured approximate peak temperatures of 1625 K with peak temperature for both methods occurring near radial distance of 1 mm. The temperature rise in the Raman measurements is steeper near the

flame boundary, approximately 2 mm in radial distance. Much tighter agreement of the FRS and Raman data exists in the Extinction Zone with the only apparent deviation occurring in the cool temperature regions of the incoming, unburned H_2-air mixture. These coolers region have a slight dip in FRS measured temperature by approximately 50 K near the radius of 3.75 mm. The direct numerical simulation results of peak temperatures disagree with both the FRS and Raman data along the Reaction Zone and Extinction Zone by nearly 200 K. Even with the discrepancy of peak temperatures, the simulation results agree with both the FRS and Raman measurements on the location of temperature drop off between 2 mm and 4 mm.

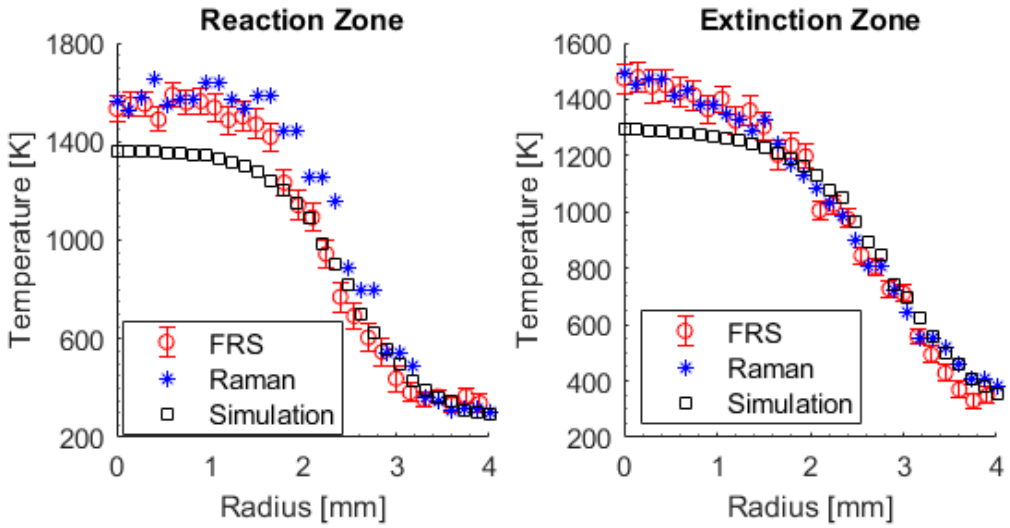

Figure 19: Comparison of FRS, Raman, and Simulation Results

The error in the FRS measurement was analyzed through signal-to-noise ratio (SNR), standard deviation (δ), and standard error of the mean (SEM). With a collection of 100 shots taken at each measurement location, these statistical methods provide a good representation of the uncertainty. In Figure 19, the error bars along the FRS data in the Reaction Zone and Extinction Zone indicate the standard deviation along those profiles.

The maximum standard deviation for the continuous wave FRS was found to be ± 60 K which occurred in proximity to the peak temperatures near the radial distance of 1.8 mm at the edge of the temperature drop-off. Using the standard deviation and the number of samples taken at each location (n), the standard error of the mean, where SEM = $\delta / (n^{1/2})$, was found to be ± 6.0 K at the same radial location of peak temperatures. The SEM value is 10x smaller than the standard deviation, which is substantially less than the scatter seen in the thermometry data. This indicates the noise in the experiment is not randomly distributed. The SNR value was determined to be 51 for the continuous wave FRS, proving to be a low-noise strategy. The systematic error in the experiment is mostly contributed to the nitrogen dominant assumption discussed earlier. When the other major species, H_2O and O_2, are accounted for, the peak temperature determined drops by 80 K (5%). This error is higher than the standard deviation, but can be accounted for without the use of the nitrogen dominant assumption. All other major sources of systematic error are reduced by the use of normalizing the flame image intensities by a reference image intensity in the derivation of Eq (6) as discussed in CHAPTER I.

2.3 Comparison of FRS Strategies

In order to shed light on the differences of FRS methods, three filtered Rayleigh scattering strategies were conducted on the previous premixed H_2-air tubular flames discussed previous. The FRS methods includes continuous wave FRS, pulsed FRS, and pulsed FRS with an external etalon. These strategies have a magnitude or more difference between their resulting optical densities of the molecular I_2 filter as seen in Figure 14. The three FRS strategies were compared in terms of agreement and ease of operation.

The raster scanning method was repeated for the pulsed FRS strategies with the exception of vertically averaging a planar sheet. Instead, the pulsed laser was focused down to a line, approximately 220 μm wide.. The pulsed FRS strategies were compared to the continuous FRS data. The agreement of the pulsed FRS strategies to the continuous FRS data is provided in Figure 20. The continuous wave FRS method contains the highest spectral purity (e.g. lowest background noise) and does not suffer from shot-to-shot noise, which provides a good reference for comparison.

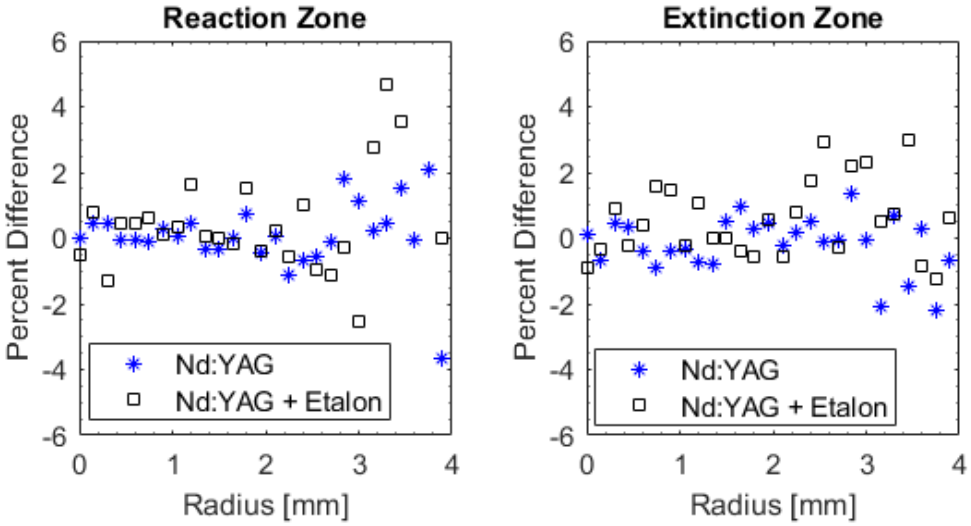

Figure 20: Agreement Comparison for Alternative FRS Methods

The agreement of the pulsed FRS methods to the continuous wave FRS data decreases after the peak temperature decline as seen by the increase scatter in Figure 20 when the radius > 2 mm. The pulsed Nd:YAG with external etalon demonstrates more disagreement than the pulsed Nd:YAG by itself. The standard deviation and signal-to-noise ratio (SNR) for the pulsed FRS methods at the location of peak temperature were determined. The contrast in standard deviation and SNR of the pulsed methods as well as the continuous wave method discussed earlier is provide in Table 4.

Table 4: Signal-to-noise ratio (SNR), standard deviation, and systematic error for each FRS method at peak temperatures (40 mJ of laser energy, 100 measurements)

Method	SNR	Standard Deviation
Pulsed laser	40	± 85 K
Pulsed laser with etalon	28	± 130 K
CW Laser	51	± 60 K

While it was expected for the pulsed FRS methods to have more noise than the continuous wave method, the use of an external etalon with pulsed FRS was anticipated to provide better quality data than pulsed FRS without an etalon. However, both the SNR and standard deviation worsen when an external etalon is utilized which compliments the larger scatter seen in the agreement with continuous wave FRS results. The external etalon acts a bandpass filter for the light leaving the laser, and essentially increases the spectral purity of the light passing through (e.g. further narrowing the linewidth). The narrower linewidth should increase optical density of the molecular I_2 filter, as measured and depicted in Figure 14, and further prevent the burner's wall scatter noise from reaching the FRS camera. However, the transmission profile of the external etalon and shot-to-shot spectral noise of the pulsed Nd:YAG used was not accounted for in that expectation. Using the specifications of the Fabry-Perot etalon in these experiments, the ideal etalon transmission can be calculated using Eq (16) and Eq (17) where F is the finesse of the etalon, m is the etalon material refractive index, t is the etalon thickness, θ is the angle of incidence, and λ is the light wavelength [49]. The resulting transmission is displayed in Figure 21 for the air spaced.

$$\tau_{etalon} = \frac{1}{1 + F * \sin^2(\varphi/2)} \tag{16}$$

$$\varphi = 4\pi mt \ * \cos(\theta)/\lambda \tag{17}$$

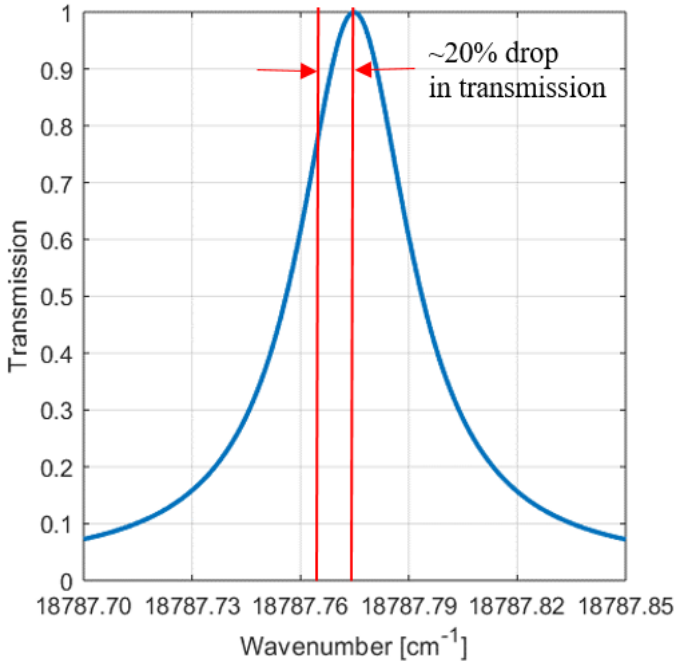

Figure 21: Change in Etalon Transmission (Finesse = 23.5) due to Change of Centerline Wavenumber

The transmission profile falls drastically with minor changes in wavenumber. For example, a change of only 0.010 cm^{-1} (300 MHz) results in an approximate 20% drop in transmission through the etalon, also depicted in Figure 21. The shot-to-shot variation in the FRS experiments were determined to be approximately ±0.003 cm^{-1} (90 MHz) resulting in a maximum ± 6% transmission drop between each shot of the 100 shot sample.

The external etalon was successful in increasing the spectral purity of the incident light as determined by increase in optical density from 3 to 4 of the pulsed FRS methods, but it also provided the complication of increasing the noise due to the coupling of the

etalon transmission profile and host-to-shot variations in the laser frequency. The optical configuration for future experiments needs to be able to adapt to this sensitivity and suggestions are provided later in this chapter.

2.4 Conclusion

The measurements taken have demonstrated, for the first time, filtered Rayleigh scattering can be conducted using a continuous wave laser when diagnosing a steady-state flame. Additionally, the use of a CW laser allows the exposure time of each shot to be longer, reducing the power going through burner windows. This reduction of power enabled the ability to capture the axial structure of the tubular flame with a planar sheet. Furthermore, the nitrogen dominant assumption displayed reasonable accuracy for lean, premixed hydrogen flames. However, all major species should be considered if richer conditions were explored. The comparison of the FRS data with Raman scattering data, and direct numerical simulation data confirms earlier findings by Hall and Pitz [24]. The preferential diffusion is under predicted by the direct numerical simulations when compared to experimental results. More diffusion of H_2 will lead to increasing the local equivalence ratio and temperature of the local area. This under prediction is speculated to be caused by inaccuracies in diffusion rate constants for light species such as H and H_2 [50]. However, a sensitivity study of the diffusion rates on these simulations could provide insight to that speculation. The FRS temperature relation to S^* was not monatomic at low temperature, but future experiments can avoid this problematic nature by tuning the laser slightly off center (~ 200 MHz) of the iodine absorption band [11]. This study was concerned with the high temperature regions, and further investigation into the cooler regions was not explored.

The continuous wave FRS method provided a stable, accurate method of FRS thermometry when used for steady state flames when high spectral purity or optical density is needed. However, the continuous wave FRS method may not always be a viable option. When short exposure times are needed for transient conditions, a pulsed FRS method is preferred. However, one needs to consider the expected Mie scattering occurring the field and the optical density provided by the FRS system. An external etalon can improve the optical density of a pulsed FRS system by acting as a bandpass filter for the incident light and further increasing the spectral purity of the light. However, if the measurements are subject to image averaging, then shot-to-shot noise and fluctuating light intensity downstream of the etalon needs to be considered. The light intensity fluctuations could be accounted for if the energy is simultaneously measured downstream of the etalon, possibly using another beam splitter to measure a small percentage of the overall energy. If this is also done during the reference conditions imaging, the energy fluctuations in the flame images could be appropriately adjusted. A summary of the FRS method characteristics for the equipment used in this study is provided in Table 5.

Table 5: Summary of experimental considerations for FRS methods

Method	**Maximum Optical Density**	**Exposure**	**Operation**
CW Laser	6+	Long (ms)	Active tuning of laser
Pulsed Nd:YAG	3	Short (μs)	Intermediate loss of frequency control (unlocked seeding)
Pulsed Nd:YAG with Etalon	4	Short (μs)	Intermediate loss of frequency control (unlocked seeding) and susceptible to shot-to-shot frequency noise

CHAPTER III

DIGITAL IMAGE FILTERING FOR CONTAMINANTS IN FRS IMAGES

3.1 Background

The FRS experiments discussed thus far have only involved steady-state flames with the major noise source being the laser scattering from the burner walls. However, transient, turbulent flames can also be optically diagnosed using filtered Rayleigh scattering. For steady flames, multiple shot averaging can be used while transient flames are likely limited to measurement by a single-shot. Other than temperature, the velocity profile of turbulent flames are also of interest. A benefit of using FRS thermometry for these turbulent flames is the ability to obtain simultaneous measurements of velocity using Particle Image Velocimetry (PIV) [34, 51]. The combination of these two measurements provides temperature and velocity data of fields that could be utilized in closure terms for turbulent flame modeling [52].

Simultaneous FRS and PIV measurements were attempted for premixed CH_4-air turbulent flame kernels. A side view and top view of the wind tunnel schematic and optical configuration is displayed in Figure 22 and Figure 23, respectively. Methane gas was injected midstream into the airflow of a wind tunnel that flows across a diamond patterned active or passive turbulent grid. The methane flow rate was adjusted to set an equivalence ratio of 0.7 while the wind tunnel operated at a velocity of 30 m/s in atmospheric pressure. Downstream of the turbulent grid, an ignition laser is focused down to ignite the CH_4-air mixture at the radial midpoint of the tunnel.

Observation windows are downstream of the ignition point for optical diagnostic implementations. For the experiments considered here, 532 nm light was formed into a 25 mm wide, 0.2 mm thick planar sheet in order to acquire a 2-D measurement of the turbulent flame kernel's temperature field. The laser light was fine-tuned to 18787.798 cm^{-1}, the same iodine transmission band used in the previously discussed tubular flame experiments. The FRS images were captured with a PCO 2000 camera downstream of a 25.4 cm iodine cell. The images captured contained an approximate pixel resolution of 0.08 mm in both horizontal and vertical directions.

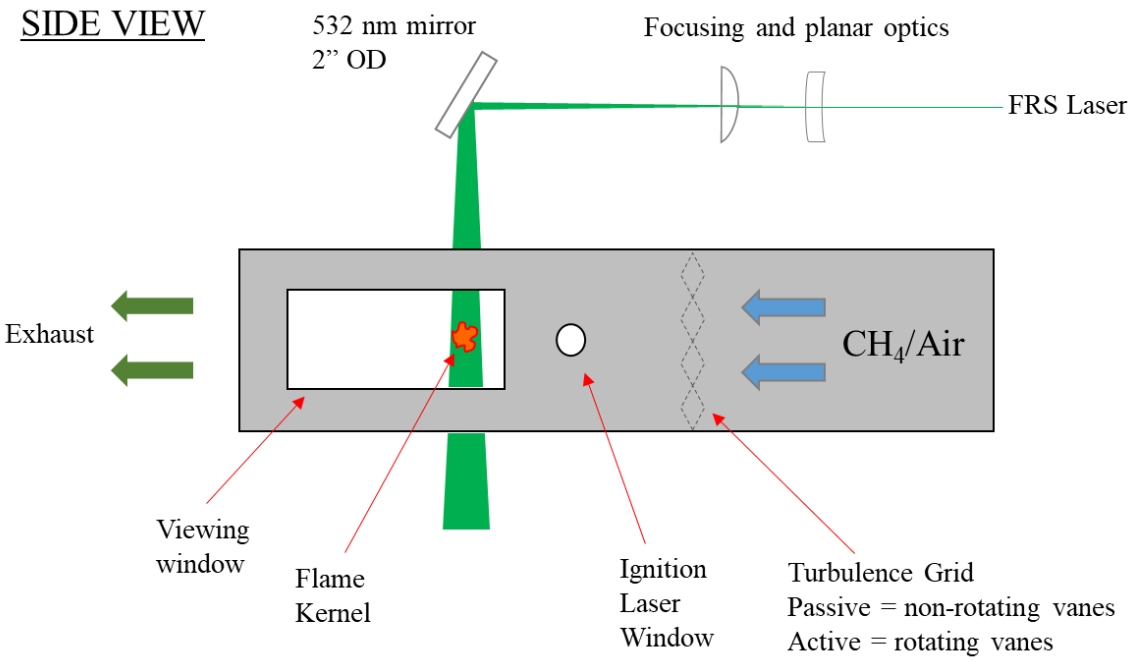

Figure 22: Side view of turbulent flame kernel experimental apparatus

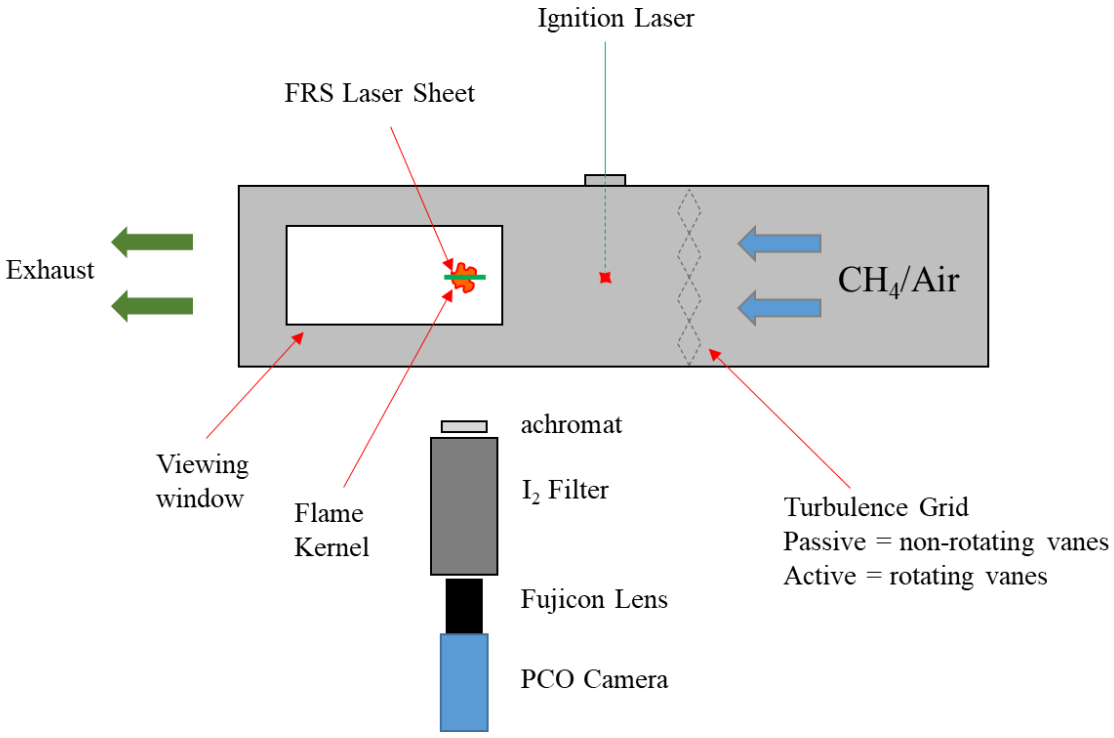

Figure 23: Top view of turbulent flame kernel experimental apparatus

One hundred images were recorded at operating conditions with only flowing air and no ignition laser operation. These images were then averaged to provide a representation of the reference image ($R_{j,k}$). Afterwards, fuel flow and flame kernel ignition were initiated. Several single-shot images were captured of the turbulent flame kernels ($F_{j,k}$), but averaging was not conducted due to the single-shot nature. The nomenclature of $R_{j,k}$ and $F_{j,k}$ is used here for consistency with the representation of Eq (5) and Eq (6). An example raw image of the background-subtracted averaged reference flow ($\bar{R}_{j,k}$) and background-subtracted turbulent flame kernel ($\bar{F}_{j,k}$) is displayed in Figure 24 along with the FRS determined temperature. The recorded intensity of the images are displayed in arbitrary units and are representative of the intensity counts measured on each camera pixel.

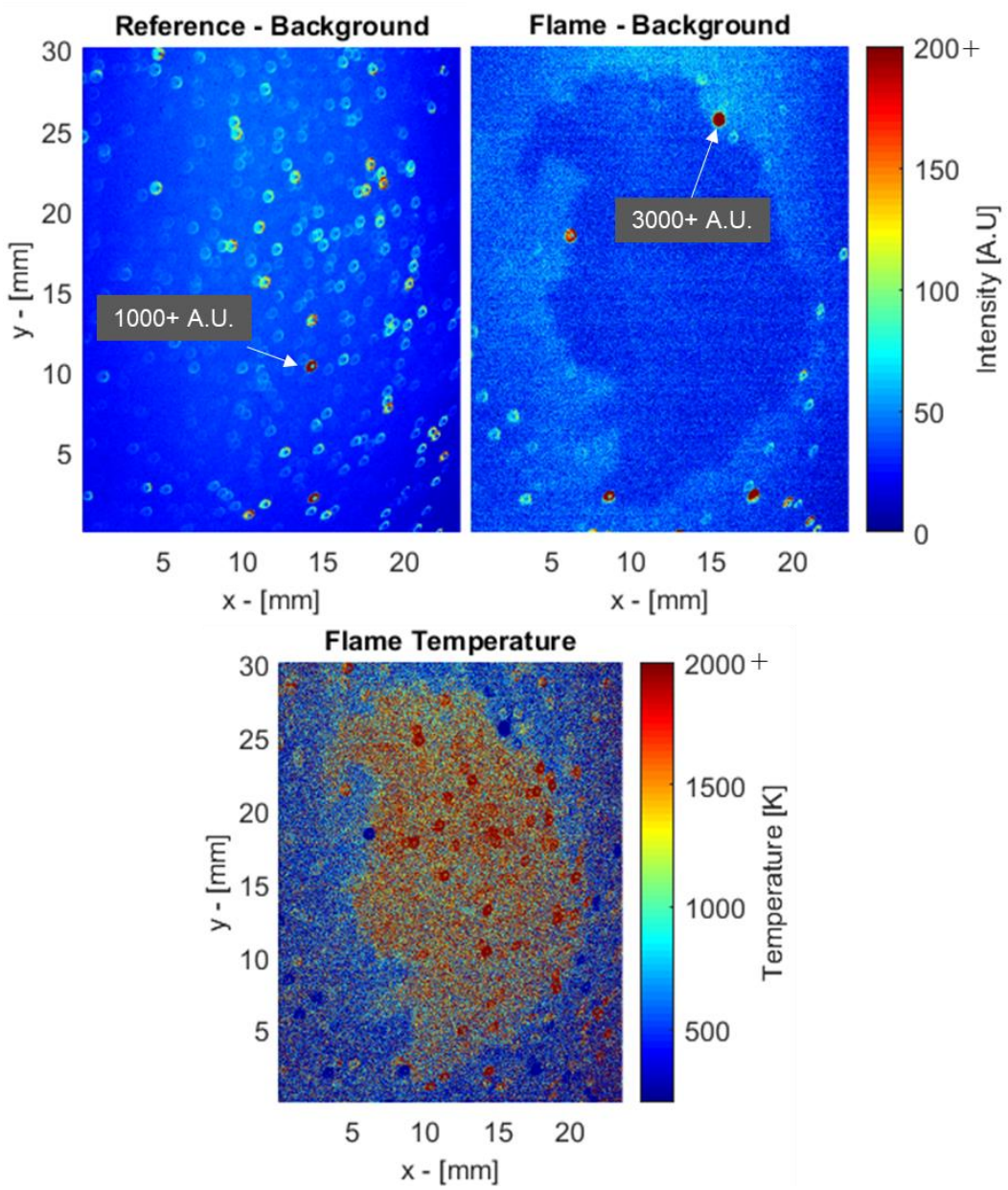

Figure 24: Average of 100 Reference Images (Top Left), Single Shot Image of Flame Kernel (Top Right), and Derived Temperature (Bottom) of a Premixed CH_4-air Turbulent Flame Kernel with Equivalence Ratio of 0.7 and an adiabatic flame temperature of 1830 K.

Both the reference flow image and the flame kernel image contain high intensity anomalies. The averaged reference flow appears to contain many contaminants in the flow path when compared to the flame image, but this is due to averaging the array of 100 reference images with each single reference image containing the approximate

contaminant count seen in the flame image but at different locations. However, the flame image is grainier when compared to the averaged reference flow and does not have the benefit of smoothing out noise through averaging. Unfortunately when these two image sources are used derive the FRS determined temperature, the spherical artifacts from both sources appear in the temperature profile as spherical anomalies of low and high temperature.

After these experimental efforts, it was learned that the wind tunnel had been used for prior PIV experiments, and the tunnel could contain residual, agglomerated particles. Additionally, some evidence exists that the contaminants come from a liquid source such as water or oil due to the 'eyelet' appearance that is displayed later as well as the lack of contaminants inside the flame. Typically, liquid droplets interact with these high temperature flames and evaporate in the case of water or used as fuel in the case of oil. Regardless of the source, the artifacts are treated as Mie scattering contaminants in the images captured. The differentiation as particles or droplets does not affect the investigation approach or results in this study. When the data is post-processed, false, high-temperature regions obscure the actual gas temperature in the region. This phenomenon occurs when the molecular I_2 filter is not optically dense enough for the intensity of Mie scattering in the field, and Mie scattering leaks through to the FRS detector.

Digital image processing and digital filtering can provide useful tools when managing recorded images that are flawed or tainted in some capacity. Some past PIV and FRS work have used digital median filters to reduce the camera noise and leaked Mie scattering detected with mild success [53, 54]. Applying digital filtering to FRS data has

some unique concerns such as the relative digital filter size to contaminant size or flame structure that has not be reported in other studies. Additionally, FRS images with residual contaminants will need digital filters that can adapt to localized aberrations while avoiding modifications of the observed surrounding gas (e.g. mitigate contaminants but maintain flame structure). The remainder of the chapter is dedicated to adaptation of digital filtering that can be applied to contaminant-laden FRS images. Analysis is provided on the prior methods as well as an original method specifically targeted at removing the contaminant footprint on the images.

3.2 Digital Filtering Setup

The median filters used in prior studies provide a great ability for reducing noise of an image while maintaining the apparent edges in the image. Additionally, the values used to replace the central pixel of the filter window are values already present in the image (unlike that of an averaging filter). However, when intensity anomalies are sufficiently widespread compared to the applied digital filter size, the median filter essentially detects the anomaly as an edge to preserve. The filter size can be increased to encompass the anomalies, but the remaining image without anomalies will also be influenced by this increase in window size, likely smoothing out features more than desired.

For FRS images without contaminants, the highest intensities detected should come from cooler, non-reacting gas temperature, which is often the surrounding air flow at room temperature and pressure. When flames pass through the field of observation, the detected signal decreases as described by in Eq (6) in Chapter I. However, when large

contaminants are also present in the field, intensities can be recorded that are magnitudes greater than the reference image of air, especially when the FRS system does not have the adequate OD to reduce the Mie scattering. This unidirectional increase in intensity allows the recognition of contaminants in the flow and provides opportunity for image processing to have systematic recognition and filtering capabilities. A schematic of the relative intensity changes is provided in Figure 25 with the appropriate signals labeled for filtering out or maintaining.

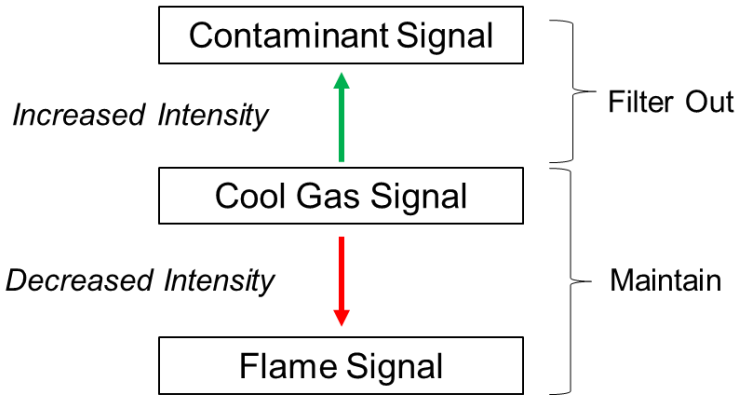

Figure 25: Schematic of Expected Signal in Contaminant-Laden FRS Images without Adequate Optical Density

The concept of median filtering has been modified for the mitigation of undesirable anomalies while preserving the gas structure edges in the remaining image. A traditional median filter replaces the central pixel in the filter window with the median of all the values in the filter window. The modified concept takes a similar approach, but ignores all values above a particular threshold (e.g. pixel values associated with contaminant scatter intensity). Since the filter was designed to reduce the footprint of the apparent contaminants in FRS images, the filter will be referred as a "Contaminant Rejection" filter or a CR filter for the remainder of the paper. An example of the Contaminant Rejection filter is provided in Figure 26 below. In this example, the hot

flame, cool air, and pixel intensities are arbitrary values of proportional differences. A 3x3 filter window is marked to provide a display of the pixels considered into the median determination, and the boldened value is the pixel being replace by the filter. As seen in Figure 26, the median filter preserves the contaminant edge with only a mild change of 252 to 220 in value while the contaminant rejection filter significantly drops the pixel value down to 65. This demonstrates the ability to replace the contaminant appearance with the surrounding gas.

Figure 26: Example of Contaminant Rejection Filter

The threshold was determined from an image sub-section containing no apparent contaminant signal. In this sub-section, the average intensity (μ) and standard deviation (δ) were determined. The threshold (TH) was determined from adding three standard deviation values (δ) to the average or $TH = \mu + 3\delta$. This criterion was chosen to set the threshold outside of the limits of Gaussian noise (more than 99% of noise below threshold). Since pixel values above the threshold were not considered in median calculations, the contaminant boundaries can be replaced by the median of the

surrounding environment. This strategy is particular useful when the filter window is undersized relative to the artifact to be filtered out. Because the signal of the non-reacting flow and combusting gas is expected to be well below the threshold, this filtering strategy does not affect the underlying gas structure more than a traditional median filter would. Essentially, the new filtering process could be described as a threshold median filter or a weighted median filter that conditionally applies a weight of zero to values above the threshold.

For large contaminants, sufficiently large filter sizes may be needed to reduce the apparent contaminant area and its influence on the FRS determined temperature. However, increasing the filter size increases the likelihood of smoothing out the subtle edges of detected gas and wrinkled flame structures. To mitigate this concern, a second version of the Contaminant Rejection filter was created that only filters the anomalous contaminants and could work in conjunction with the a traditional median filter instead of replacing it. This other version applied a logical capability to the original CR filter that only filtered the anomalous contaminant intensities and not the remaining gas intensity. An example of this filter application is provided in Figure 27.

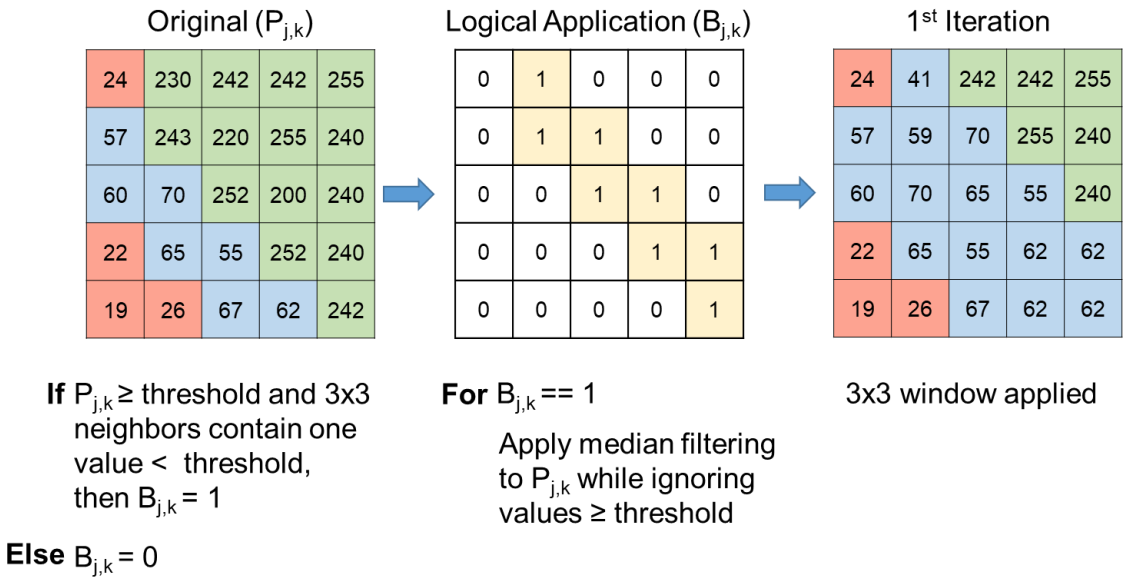

Figure 27: Example of 3x3 Iterative Contaminant Filter with Symmetrical Boundary

As seen in Figure 27, all pixels were identified that satisfied two conditions: 1) pixel intensity is greater than the threshold and 2) the neighbors in the filter window contained at least one value less than the threshold. A median filter was applied for each pixel flagged with the same disregard for all pixel values above the threshold when computing the median as previously discussed. For filter windows that contained all values above the threshold (such as the top-right portion of the original example in Figure 27), the filter is not applied until a later iteration of the filter. This iterative ability is beneficial when the filter window is significantly smaller than the contaminant area. This version of the Contaminant Rejection filter can be applied iteratively until the anomalous signal is reduced below the threshold value while the surrounding gas structure is retained. Essentially, the new filtering process is an iterative and logical adaptation of the previously discussed Contaminant Rejection filter, and it will be identified as “iterative Contaminant Rejection” filter or iCR for the remainder of the paper.

As previously discussed, the process of determining temperature from the filtered Rayleigh signal involves normalizing the signal from the experimental flow (turbulent flame) by the signal from a reference flow (free flowing air with no flame) which were previously labeled as $\bar{F}_{j,k}$ and $\bar{R}_{j,k}$, respectively. These images are the primary data for calculating the FRS determined temperature as indicated in Eq (6). The effects of digital filtering will be analyzed by the effects on the $\bar{R}_{j,k}$ and $\bar{F}_{j,k}$ images, separately, prior to the discussing the effects on the derived temperature.

3.3 Results – Reference Imaging

These images of flowing air at atmospheric pressure and room temperature were recorded as previously discussed. A total of 100 images were taken to establish the signal of the reference image, $R_{j,k}$, which were then averaged to form a single reference image. For clarity of later discussion and visual references of the individual pixels, a subsection of the averaged reference image will be used for the visual comparison of the digital filtering effects. The particular subsection of the averaged referenced image is displayed in Figure 28.

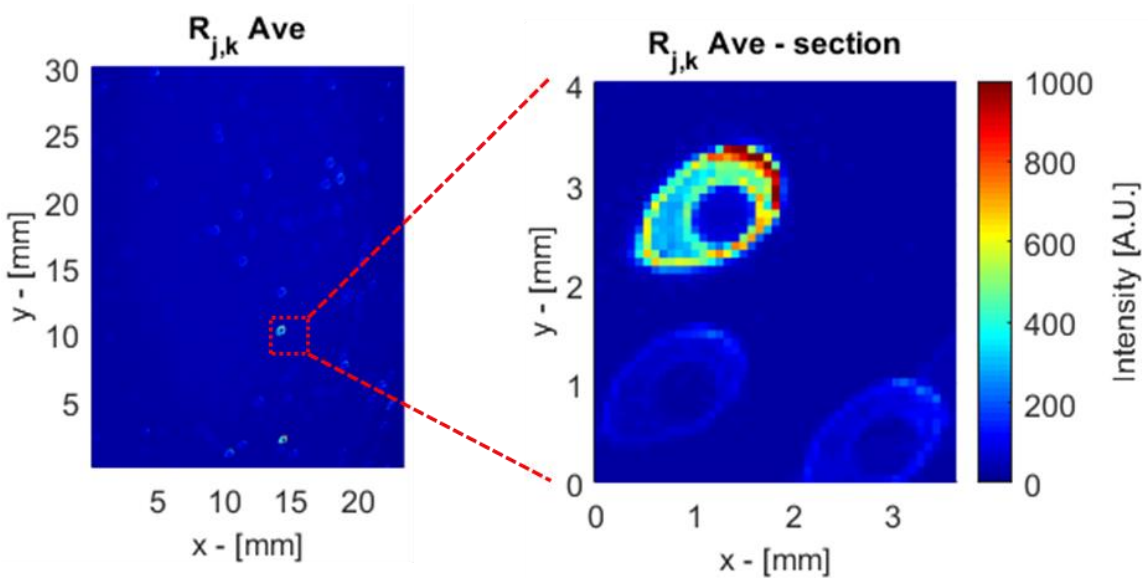

Figure 28: Subsection of Reference Image and Close-up of Contaminant

In this subsection, the contaminants in the flow are seen more clearly. One can see that the contaminants are mostly spherical with a slight edge toward the left of the image and peak intensities consistently in the upper portion (location that incident light is directed from). The contaminants appear to have a void in the center that was assumed to be related to the liquid nature of the contaminant, but it was considered outside the scope of this study. The contaminants vary with intensity with values peaking up to nearly 1000 A.U after background subtraction and averaging. For perspective, the gas flow contains intensities ranging from 40-50 A.U. after background subtraction. The results of the Contaminant Rejection filter (CR) and iterative Contaminant Rejection (iCR) on this subsection and the reference images as a whole are discussed below.

3.3.1 Contaminant Rejection Filtering

A traditional median filter as well as the previously discussed Contaminant Rejection filter were applied individually to all 100 reference images prior to averaging them all to a single image. The filter window size was kept square and varied from 3x3 to

15x15 to establish the effects of filter size. The post-processed subsection, utilizing both the median and CR filter, can be seen in Figure 29.

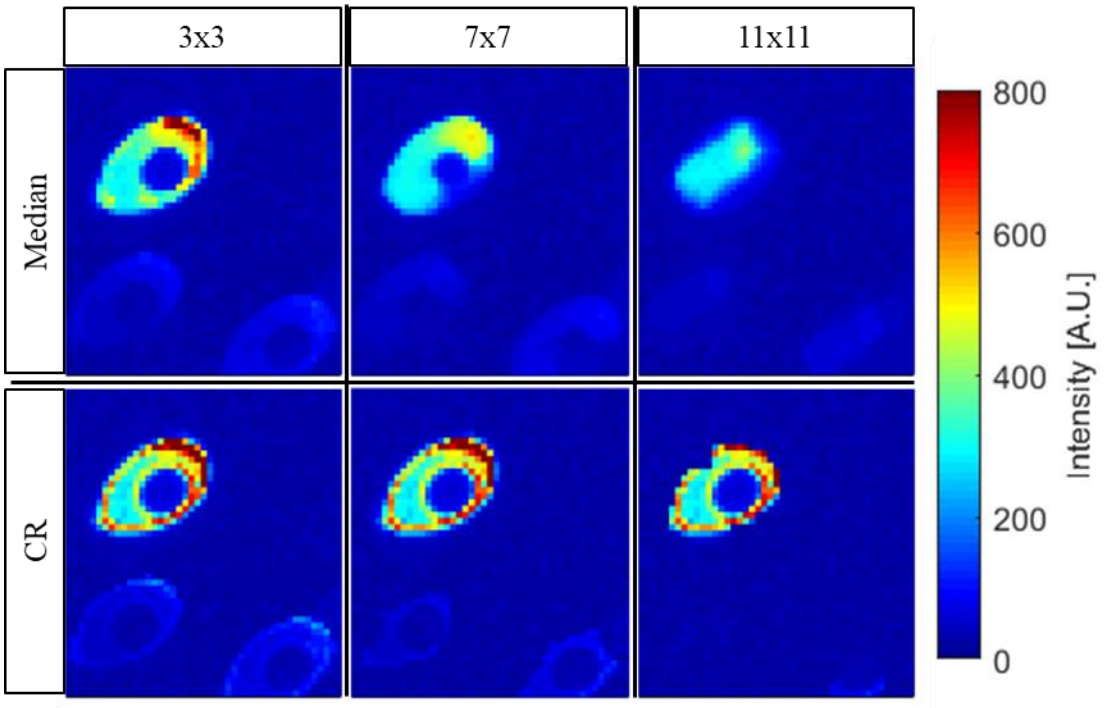

Figure 29: Comparison of Median and Contaminant Rejection (CR) for Filter Size of 3x3, 7x7, and 11x11

The median filter appears to reduce the apparent contaminant area and peak intensities of the more intense contaminant better than the CR filter. However, the CR filter begins to penetrate the edges of the contaminant once the filter size reaches 11x11. Additionally, the CR filter has nearly eliminated the presence of the less intense contaminants in the bottom of the sub-section, especially at the larger filter size of 11x11. A more thorough analysis of the filtering effects was conducted through the entire range of filter sizes. The contaminant area (A_c), maximum contaminant intensity (I_{max}), and average signal-to-noise ratio (SNR) was determined for each filtering process and normalized by the values determined from the original averaged reference ($A_{c,o}$, $I_{max,o}$,

SNR_o) image displayed in Figure 24. The contaminant area was determined by the area of pixels above the threshold, TH, described earlier. The filter size (L_f) was also normalized by the diameter of the apparent contaminants (d_c) in order to provide insight to the relative filter size to contaminant size (L_f / d_c). The normalized contaminant area, maximum contaminant intensity, and average SNR for each digital filtering process as a function of normalized filter size is provided in Figure 30.

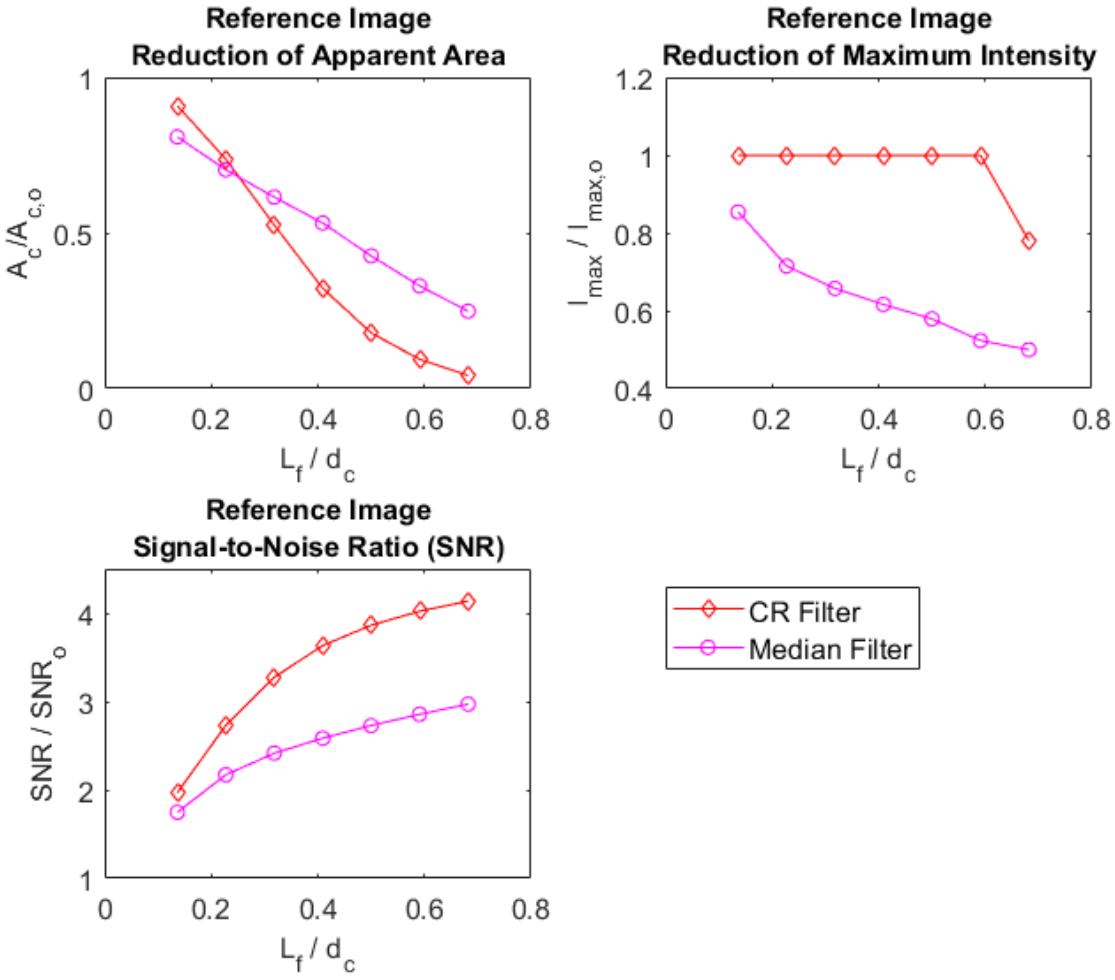

Figure 30: Relative Change of Apparent Contaminant Size (top left), Maximum Contaminant Intensity (top right), and Signal-to-Noise Ratio (bottom left)

The traditional median filter reduces the apparent contaminant area better than the Contaminant Rejection filter at smaller filter sizes (L_f / $d_c \leq 0.23$), but the Contaminant

Rejection filter is more effective at reducing the apparent contaminant area for the remaining filter size range. As seen earlier, the median filter steadily reduces the maximum intensities of the contaminants as filter size increases. The CR filter requires reaching an $L_f / d_c > 0.59$ before the highest intensities are affected by the filter. While both filters increase the SNR with increasing filter size, the CR filter is more effective throughout the entire range even though the highest intensities remain at the small filter sizes.

The previous Contaminant Rejection filter displayed mild success in reducing the apparent contaminant area and maximum contaminant intensity. However, large filter sizes were needed to achieve significant results, which runs the risks of smearing or smoothing the gas structure edges such as wrinkles in the flame and subtle flame edges. Ideally, an effective contaminant rejection filter would be nearly size dependent (e.g. a 3x3 filter and a 7x7 filter would have the same result) and could target the pixels containing contaminants while not modifying the remaining pixels. The contaminant rejection filter strategy was revised to create a 2nd version that would satisfy both of those objectives.

3.3.2 Iterative Contaminant Rejection Filtering

An iterative Contaminant Filter, iCR Filter, was created that specifically targeted pixels above the determined threshold, TH, while no filtering is done on the remaining gas structure. The iCR filter could be iterated until the apparent contaminant area was replaced with surrounding gas intensity values. Additionally, pixels not containing contaminants had no modification. More description of this process is provided earlier. A visual comparison can be seen in Figure 31 which includes processed 7x7 iterative

Contaminant Rejection (iCR), the original averaged subsection, and a 7x7 median filtered subsection. A dashed outline of the intense contaminant in the image is provided for spatial reference.

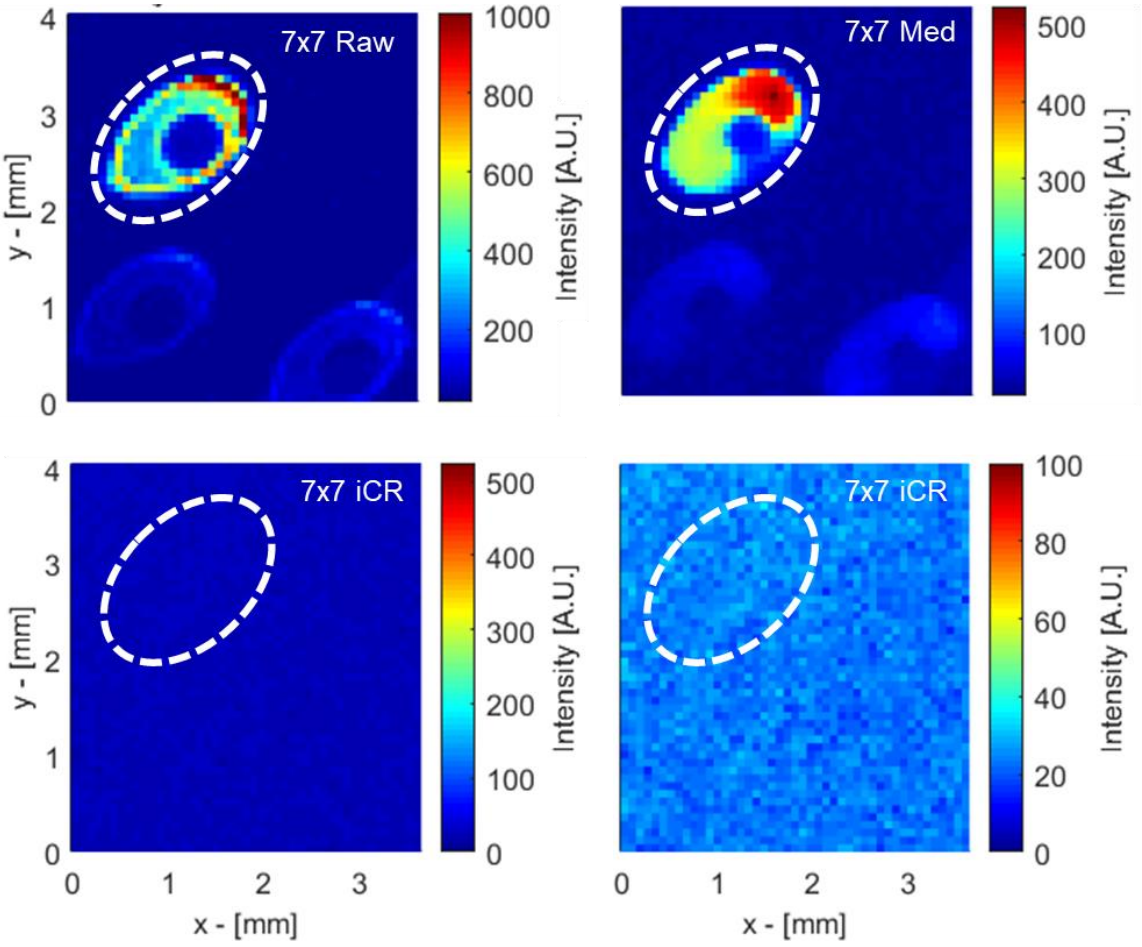

Figure 31: Comparison of Average Sub-Section of Raw Reference Image (top left) with 7x7 Median Filter (top right) and 7x7 Iterative Contaminant Rejection filter (bottom left and right) at two different intensity scales

The iCR filter does a successful job in removing the high intensity values caused by the contaminant and replacing those with pixel values in the immediate surrounding locations. As seen in the bottom right image of Figure 31, the scale of the intensity bar requires drastic rescaling to interpret differences in pixel intensities compared to the peak values seen in the averaged reference image as well as the median filtered image. The

pixel values just outside of the contaminant boundaries not affected by the high intensities of the contaminant that would be seen with large size median filters. Combining filtering methods is not uncommon in digital image processing, and the combination of the iCR filter and median filter was also analyzed in both orders: iCR filtering followed by median filtering (iCR → median) as well as median filtering followed by iCR filtering (median → iCR). The iterative contaminant rejection filter and its various combined methods were compared to traditional median filtering in terms of apparent contaminant size, maximum contaminant intensity, and signal-to-noise ratio with the results provided in Figure 32.

As seen in Figure 32, the iCR filter and both combined methods with the median filter reduces the apparent contaminant size and maximum contaminant intensity to a constant relative value at all filter sizes due to the iterative nature. This constant value is dependent upon the threshold chosen and expected since the iCR filter iterates until threshold values are no longer present. While there are no discernable differences in the iCR, median → iCR, and iCR → median filters for reduction of contaminant area and maximum contaminant intensity, variation amongst the three methods can be seen in their effects on SNR. The iCR filter mildly improves the SNR, at a constant level again, which is to be expected since only a small portion of the image (where contaminants are located) is affected. The combined median → iCR provides the best SNR increase at small filter sizes ($L_f / d_c \leq 0.23$) that is reflective of the median filtering reducing the contaminant area more than the iCR filter at the same filter size range. For larger filter sizes, the iCR → median filtering strategy is the most effective to increase SNR.

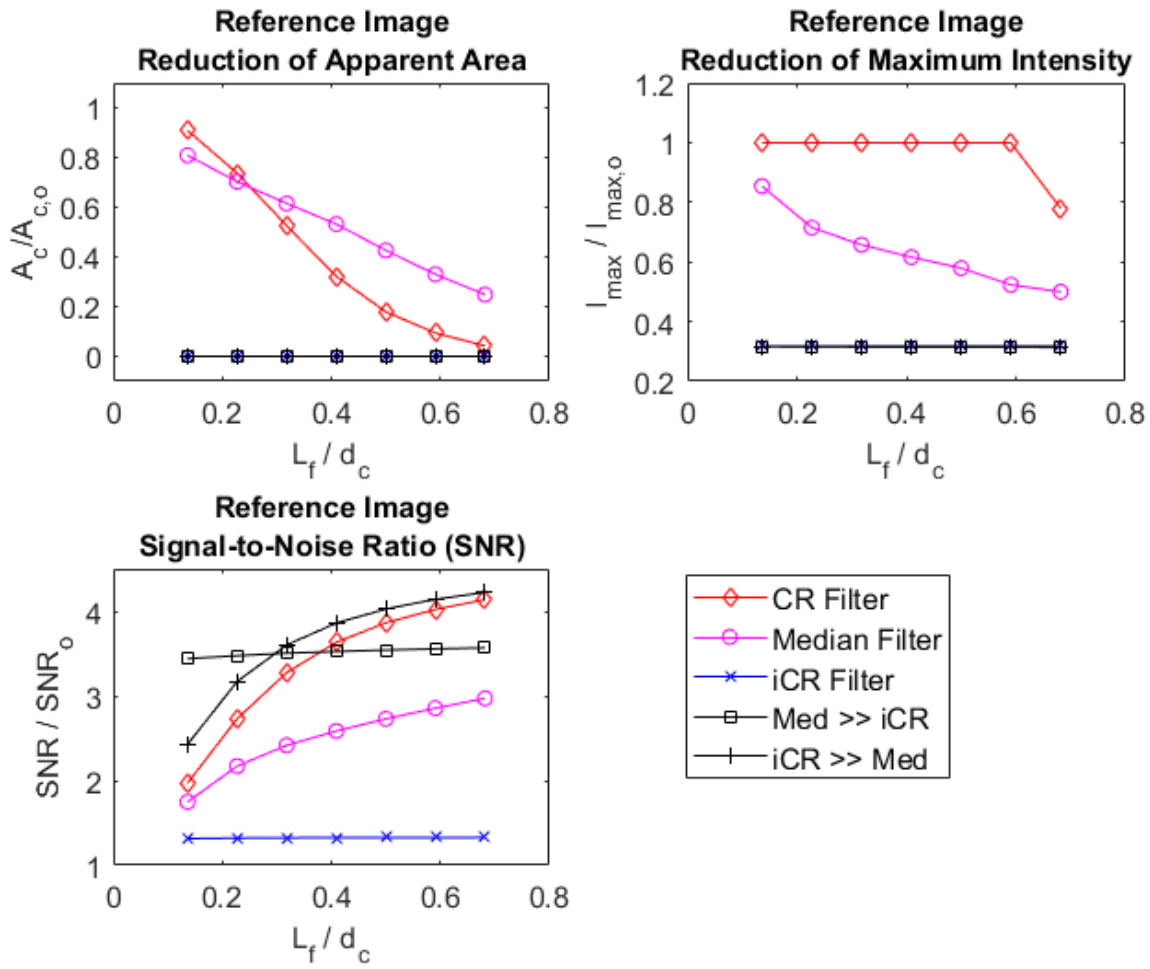

Figure 32: Effects of Filtering Methods on Contaminant Size (top left), Maximum Contaminant Intensity (top right), and Signal-to-Noise Ratio (bottom left)

The iterative Contaminant Rejection (iCR) filter reduced the maximum contaminant intensity and apparent contaminant area more than median filtering alone at all comparable filter sizes. The combination of the two filtering methods, particularly when first processing through the iCR and then followed by median filtering (iCR → median) displayed the greatest result in increasing the signal-to-noise ratio while benefiting from the reduced contaminant intensity and apparent area. The impact of the iCR → median filtering on the reference image can be emphasized by viewing its influence on the determined flame temperature. A contrast of the original flame

temperature determined from raw images and the flame temperature determined with a 7x7 iCR → median filtered reference image is provided in Figure 33 without any flame image processing. The majority of the spherical anomalies in temperature are eliminated by processing the reference images through the iCR → median filter.

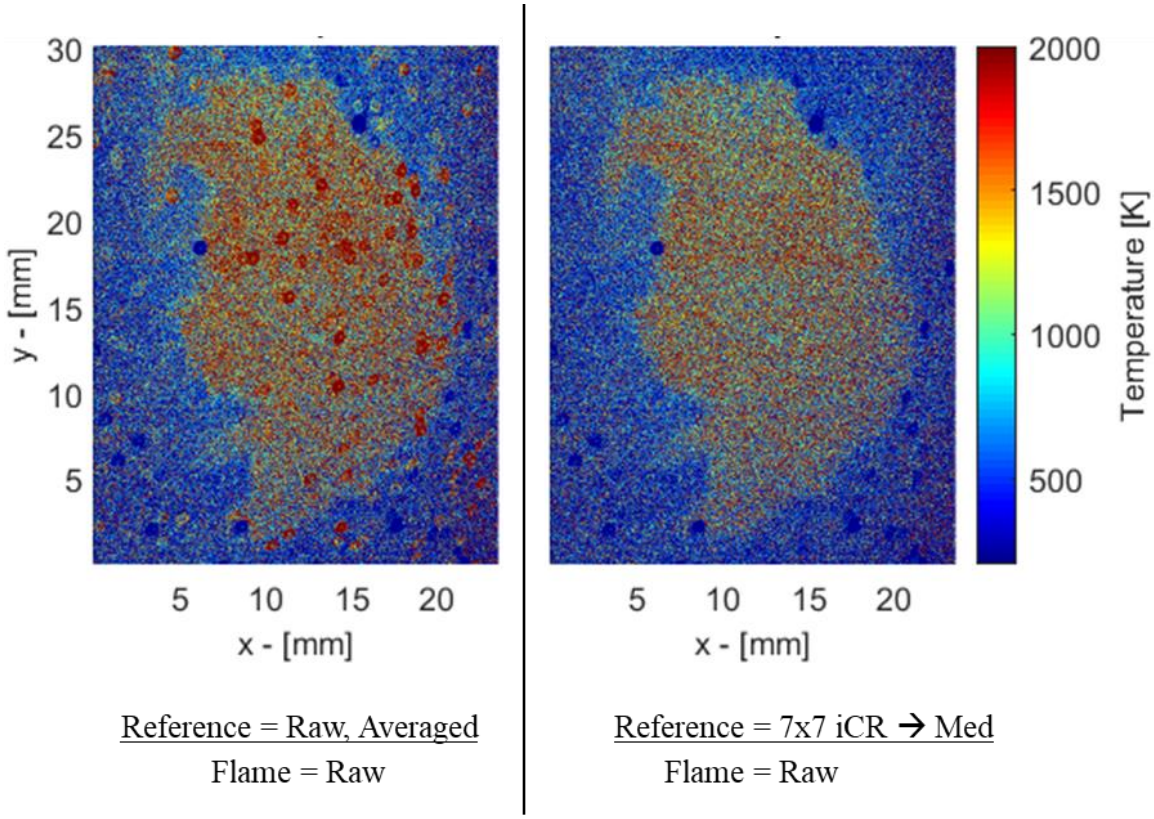

Figure 33: FRS Determined Temperature after Applying 7x7 iCR → median filtering to only the Reference Image while using the raw Flame Image

Through comparative analysis of processing the reference image, the iterative Contaminant Rejection (iCR) filter was determined to be more effective than the non-iterative version (CR). When filter sizes 7x7 or above ($L_f / d_c \geq 0.32$) are used, the combined iCR → median filter has shown to be the better of the combined filtering methods. For conciseness, the remaining analysis on the flame image processing will only consider the iCR filtering and iCR → median filtering.

3.4 Results – Flame Imaging

Similar to the reference images, a comparison analysis of the iCR filter, median filter, and combined iCR → median filter was applied to the flame image. A visual contrast of the effects of the different filtering methods and variation of filter size on the flame image is displayed in Figure 34 with an arrow pointing to the location of a contaminant with high intensity in the raw image. With median filtering, the noise in the image is reduced, but the edges of the flame begin to become less distinct as seen when the filter size is increased to 11x11. The median filter also allows severe contaminant intensities, even at large filter sizes such as 11x11. When the iCR filter is applied, the contaminant intensities drastically reduce along with the apparent contaminant area. The reduction of the contaminant area and maximum contaminant intensity of the flame image follows the same trend seen with the reference image as seen in Figure 35. Median filtering reduces the contaminant size and maximum intensity with increasing filter size while the iterative Contaminant Filter stays constant and near zero for all filter sizes. However, some appearance of the contaminant footprint remains even after eliminating all the high contaminant intensities. The flame image does not have the benefit of averaging 100 digitally filtered images, which mitigates much of this residual footprint in the averaged reference image. While the maximum contaminant intensity and area above TH are drastically reduced, a visual inspection can still determine the location of the contaminants, particularly those contaminants that did not have a high intensity and were not affected by the iCR filter.

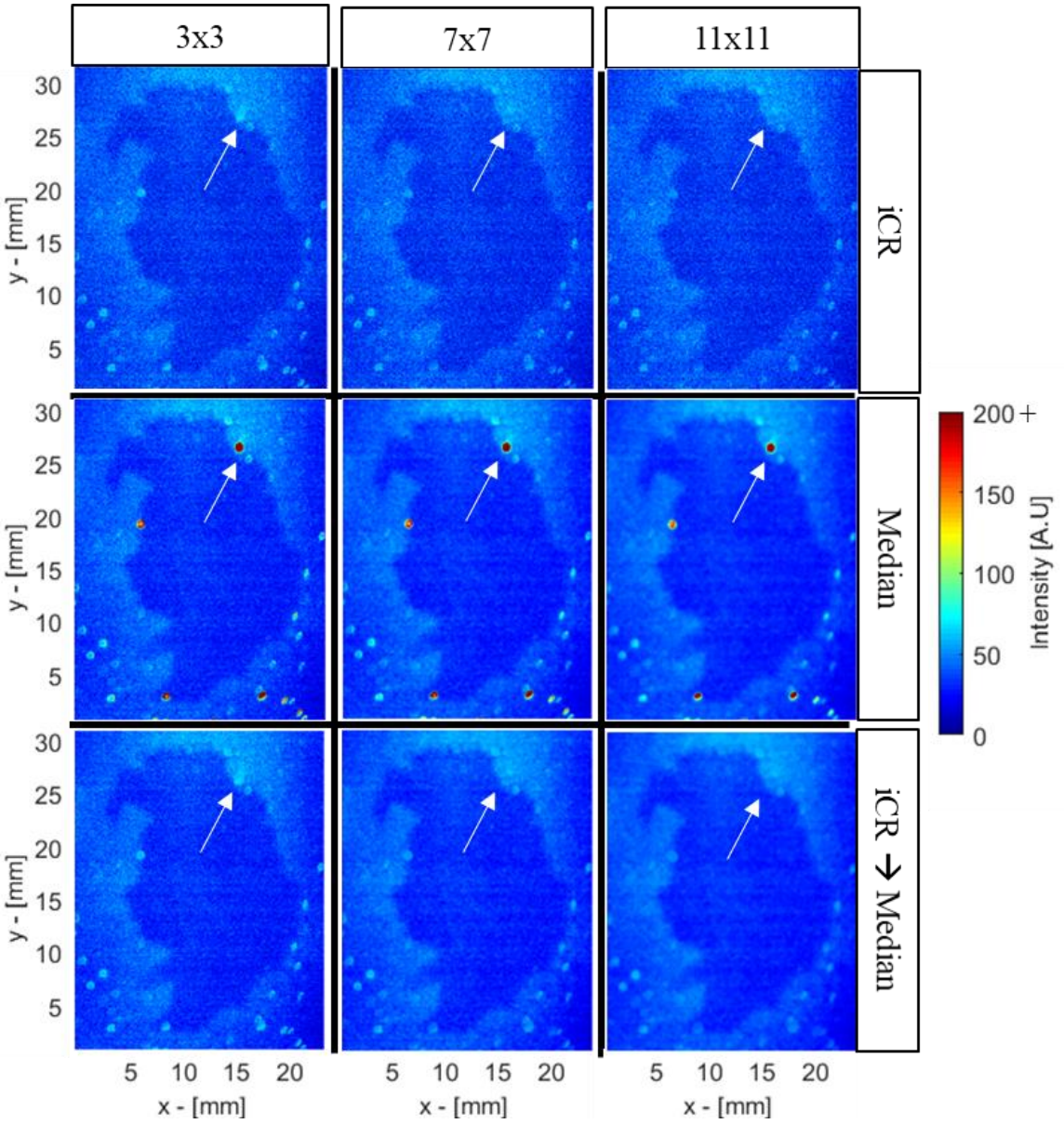

Figure 34: Flame Image with Iterative Contaminant Rejection Filter, Median Filter, and Combined iCR → Median Filtering for filter sizes of 3x3, 7x7, and 11x11. Arrow notation used to point out location of contaminant with high intensity

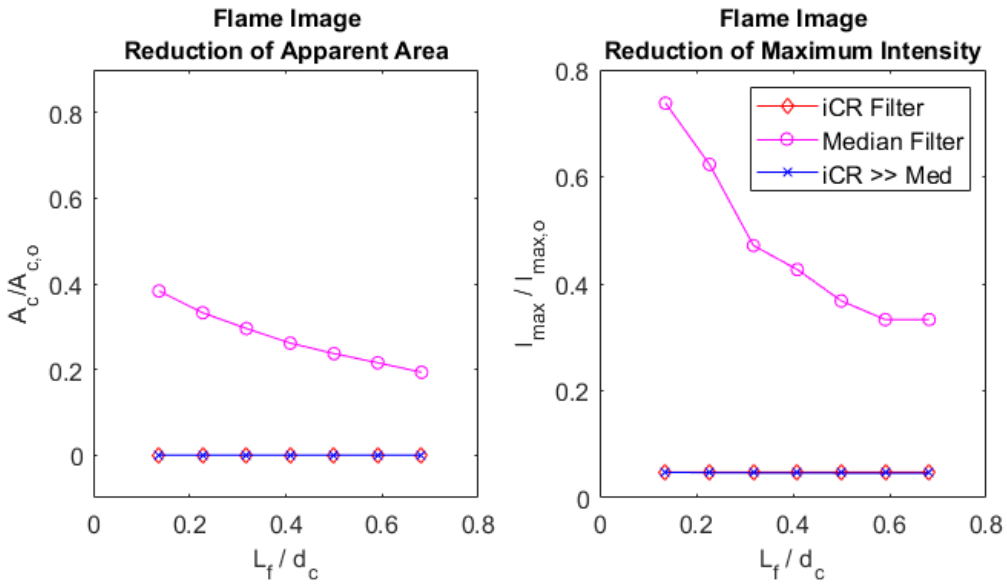

Figure 35: Relative Change in Contaminant Size (left) and Maximum Contaminant Intensity (right) from iCR Filtering, Median Filtering, and iCR → Median Filtering.

With the digital filtering effects establish for both the reference image signal as well as the flame image signal, the filtering effects on the FRS determined temperature can now be assessed. The propagating influence of the digital filtering on both the reference image and flame image for FRS determined temperature can be seen in Figure 36. In Figure 36, horizontal positions represent various filtering methods applied to the reference image, $R_{j,k}$, while vertical positions represent various filtering methods applied to the flame image, $F_{j,k}$ with images numbered for clarity of description.

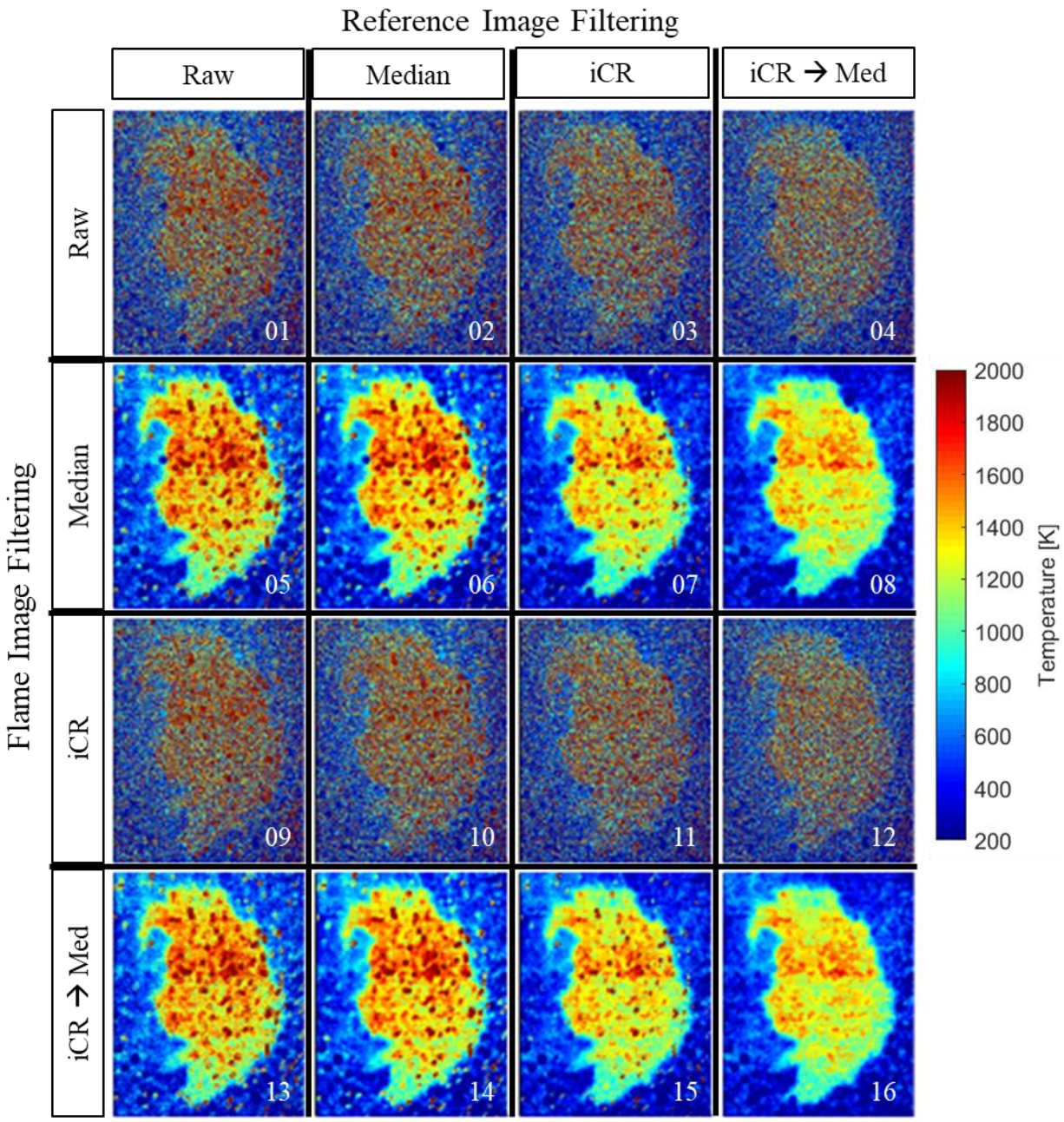

Figure 36: Effects of Various Filtering Methods on FRS Temperature
(7x7 filter size or $L_f / d_c = 0.32$)

The adiabatic flame temperature for the CH_4-air flames at equivalence ratio of 0.7 is 1830 K, which is noticeably higher than the measured temperatures here. Some discussion is provided on this discrepancy in the concluding remarks. The digital filtering effects are the main focus of this study, and will be discussed for now. The effects of both

the iCR and Median filter are clearly seen in the FRS determined temperature. The median filter provides the majority of noise reduction while the iCR reduces the apparent contaminant presence. The flame image has the greatest benefit from median filtering (compare images 1-4 to images 5-8) since the single image does not contain many contaminants, particularly in or near the flame boundary. Comparing images 8 and 16, you can see there is no apparent gain in applying the iCR → median filter on the flame image instead of only a median filter due to background noise being more of an issue instead of the number of contaminants. For the reference image, the combine iCR → median filter produces the best results as seen by comparing images 5 and 8 or images 13 and 16. Digitally filtering the reference image through the iCR → median filter has the greatest influence on reducing the contaminant presence. Averaging the array of 100 images inherently reduces the noise once the contaminants are removed.

Observing the flame area is useful in analyzing flame stretch ($dA_f/A_f \cdot dt$). The temperature profiles were converted over into binary images to observe the flame area. All pixel area of 1000 K was considered area of the flame since this temperature represents the approximate 50% difference between the ambient air and adiabatic flame temperature. The binary images can be seen in Figure 37.

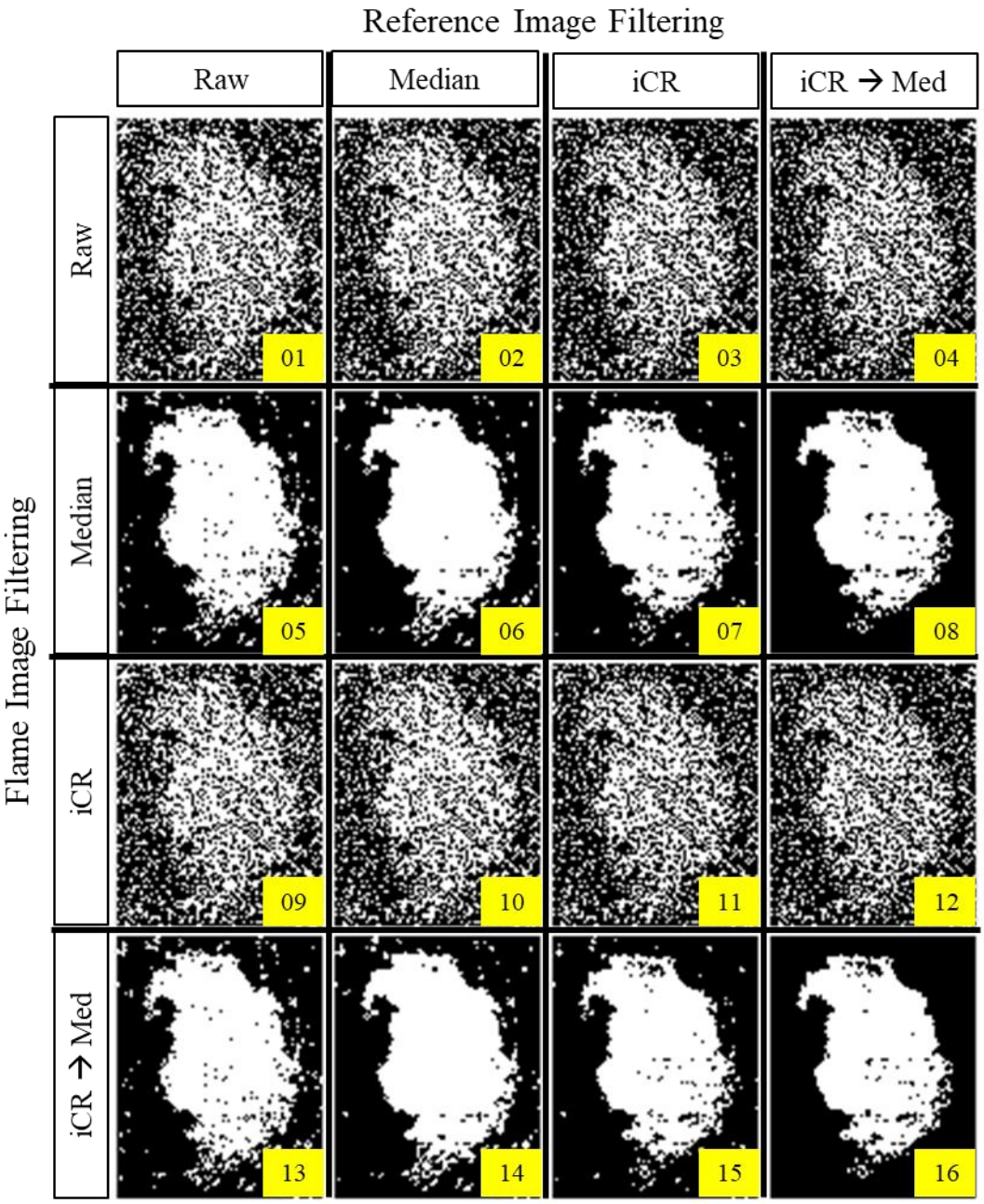

Figure 37: Effects on Flame Boundary with Various Filtering Methods
(Filter Size = 7x7)

In the binary images, the median filter greatly reduces the noise surrounding the flame. However, the use of the iCR → median produces the clearest flame boundary edges with most of the effects seen by filtering the reference image. With the cleaned up

flame boundaries, an automated image processing scheme could be conducted to determine the flame area with a significant reduction in uncertainty and error.

3.5 Conclusions

A digital image filtering technique was created in order to increase the quality of FRS images that contained Mie scattering from contaminants. The new technique utilized the strategy of a weighted median filter, but applied it logically and iteratively in order to target pixels suspected of Mie scatter from contaminants. This iterative Contaminant Rejection filter successfully replaced anomalous, high intensity pixels with the neighboring median values, essentially replacing the signal from the contaminant with signal from the near surrounding gas. The area of the apparent contaminant size, maximum contaminant intensity, and signal-to-noise ratio improves with the application of the iterative Contaminant Filter. Even greater results were achieved when the iterative Contaminant Rejection filter was followed by median filtering. With this technique, the quality of the flame temperature data and flame boundary data was improved.

Some improvements can be made to the iCR filter. Currently, a user must select a sub-section of the image that does not contain the anomalous intensities and is representative of the expected noise. Future improvements could include an automated method of evaluating non-contaminant related noise in order to reduce the possibly of user error. The automated method can be compared to various flame types and burner/wind tunnel configurations to validate the use in multiple applications. The data used in this study contains contaminants that lack characterization. The use of digital filtering applied to FRS containing such contaminants would benefits from a follow up

study on contaminants of known size, index of refraction, etc. The following chapter discusses the effects of these contaminant characteristics on simultaneous PIV/FRS experiments and the necessary considerations to prevent Mie scattering leakage onto the FRS images.

While analysis of the flame temperature was not the primary focus of the digital filtering efforts, some comments are necessary on the measured temperature. CH_4-air flames with $\Phi = 0.7$ have an adiabatic flame temperature of approximately 1830 K. The majority of the measured flame temperature has some peak temperatures of approximately 1700 K, but the majority of the flame remains near 1500 K, significantly lower that the adiabatic flame temperature. However, there are a few possible causes for the lower temperature. The primary motivator for the image processing efforts were the contaminants in the flow. The contaminants observed are likely water in the flow due to condensation in the wind tunnel. Interaction between the flame kernels and the water droplets will lower the flame temperature, particularly with droplet vaporization near or in the flame. Additionally, the temperature of the flow was measured with a thermocouple in the flow, essentially measuring stagnation temperature instead of static temperature. This method can leads to lower temperatures measured for the reference image, possibly adding bias to the FRS temperature determination. Further investigation is needed.

CHAPTER IV

CONSIDERATIONS FOR SIMULTANEOUS FRS & PIV EXPERIMENTAL DESIGN

4.1 Background

Rayleigh scattering is limited to particles that are small enough to experience a uniform electric field at any moment in time (e.g. the particle size is many times smaller than the incident light wavelength). The Rayleigh criteria requires $x << 1$ where x is defined in Eq (1) in CHAPTER I. This criteria works well for gases, but combusting flows can create large, solid carbon particles due to soot formation, which do not fit this criterion. Prior studies have applied Filtered Rayleigh scattering to combusting fields producing soot in order to measuring the underlying gas temperature [55, 56]. However, some fields measured with FRS have droplets or particles that are intentionally injected into the field such as droplets from a liquid fuel injection or solid particles for Particle Image Velocimetry (PIV) measurements [34, 57]. Nearly all of the droplets and particles mentioned are sufficiently large to fall outside the Rayleigh criteria. Instead, Mie scattering theory is appropriately applied to these droplets and particles.

Filtered Rayleigh scattering is often used to measure these droplet-laden or particle-laden flows since it has the ability to simultaneously measure gas properties such as temperature through FRS alongside velocity measurements through PIV. For experiments seeking this simultaneous measurement of Rayleigh scattering and Mie scattering, separate detectors are used: one set of detectors for PIV image sequences and another detector combined with a molecular filter for the FRS imaging. An example of such an experimental setup is provided in Figure 38.

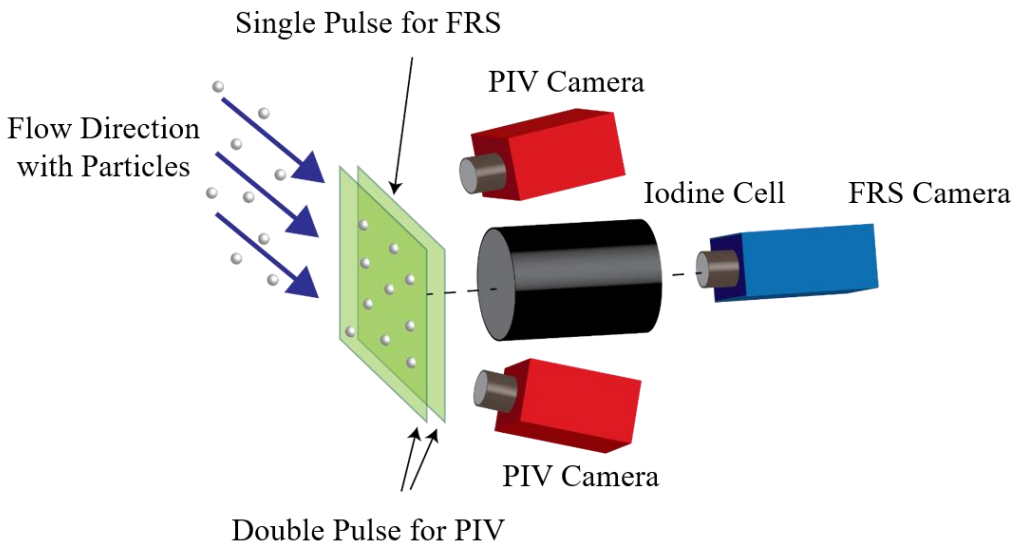

Figure 38: FRS and PIV Measurement Apparatus

In this figure, one can see that the flow field contains solid particles that will be probed by a laser sheet: a single pulse for the FRS image and a double pulse to collect sequential PIV images with a known time gap. PIV cameras may include a neutral density filter if the desired Mie signal is too high, but only the FRS camera will be equipped with a molecular filter such as the vaporous iodine cell previously discussed.

Many variables exist that contribute to the intensity of the Mie signal and the iodine filter's optical density. The particle cross-section, particle number density, particle index of refraction, and incident light intensity factor into the unfiltered Mie scattering signal. The optical density of the iodine cell is determined by the incident light's spectral purity, the incident light's centerline frequency, and the molecular filter's number density is controlled by the pressure and temperature of the cell. In order to evaluate a proper experimental design, the adequate optical density needed for expected flow conditions must be determined. Theoretical calculations have been conducted to predict the expected Mie scattering intensities and Rayleigh scattering intensities from a variety of conditions,

which enables an experimentalist to conduct proper experimental design. The models used in the calculations were described in CHAPTER I. Further description of the calculations and assumptions is provided in the next section.

4.2 Model Setup

Optical diagnostics are conducted on a wide range of observable areas. For the determination of Mie scattering and Rayleigh scattering in these calculations, an area of $1mm^2$ was considered. This constant area provides the basis of how many particles and gas molecules can be accounted for a range of number densities, but the results are normalized to provide extrapolation for various area sizes. From an assumed gas composition, temperature, and pressure, the Rayleigh cross-section, σ_R, and gas number density, ND_R, can be determined. The particle or droplet cross-section, σ_M, and number density, ND_M, must be directly or indirectly chosen for the experimental design with such considerations for the desired PIV signal. The particle or droplet material will have an index of refraction value, m, which will influence the Mie scattering intensity as seen in Eq (14) and Eq (15). The field of observation will include both Rayleigh and Mie scattering from the gas and particles influenced by their respective cross section and number densities values as represented by the example schematic in Figure 39.

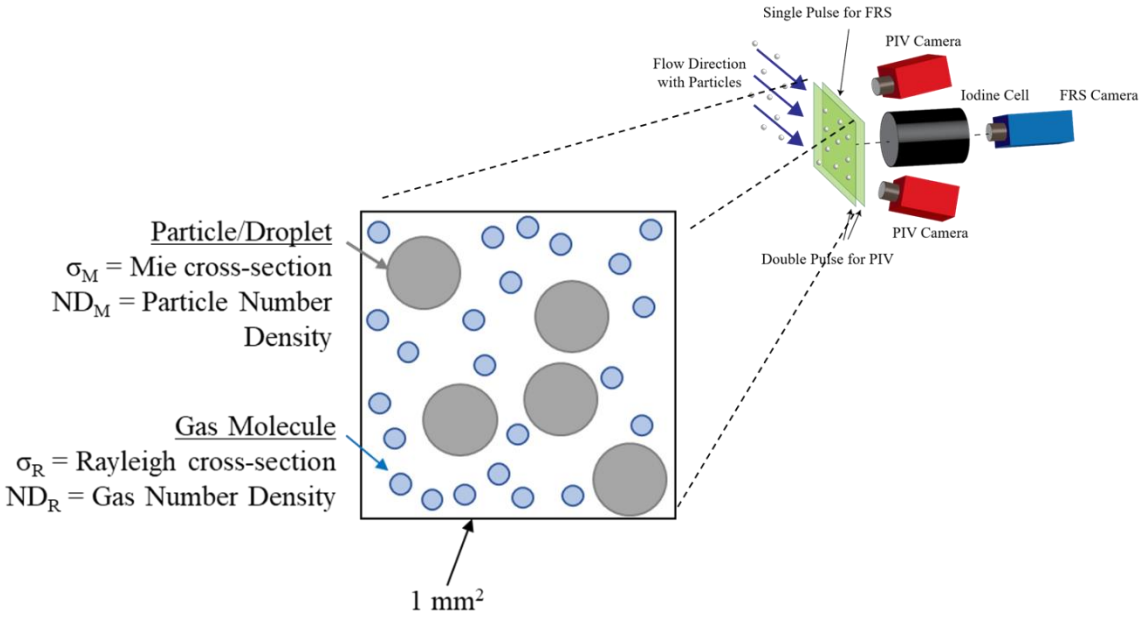

Figure 39: Schematic of Observable Area

For an observable area, the accumulated Mie scattering signal can be computed using the equations in CHAPTER I along with the adaptation of molecular iodine transmission for the filtered Mie scattering signal, in a manner similar to that seen with filtered Rayleigh scattering discussed previously. It is worth reminding that the linewidth of the incident light, and therefore the Mie scattering, is thin in comparison to the width of the iodine transmission. An example of the non-filtered intensity profiles is provided in Figure 40 with the Mie scattering computed from Al_2O_3 particles (m=1.76) containing a particle density of 25 particles/mm^2 and constant diameter of 4 microns as well as the Rayleigh scattering computed from nitrogen gas at 300 K and 1 atm. The iodine transmission band is also provided in Figure 40 for perspective of spectral width.

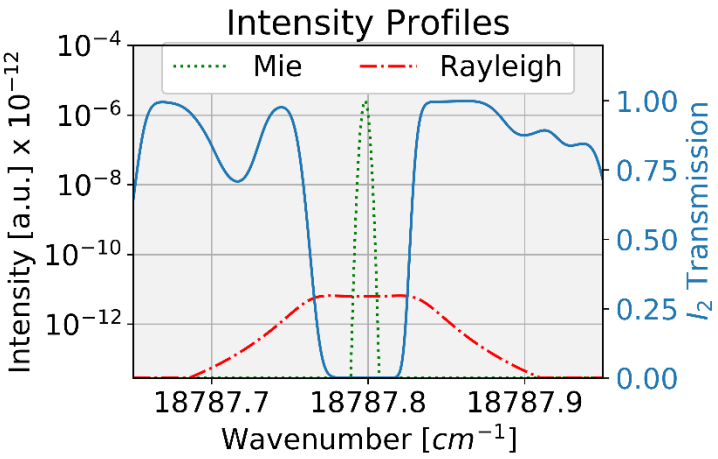

Figure 40: Intensity Profiles of Mie scattering (Al_2O_3, 4 micron, 25 particles/mm^2) and Rayleigh Scattering (N_2 at 300 K, 1 atm) without Application of Molecular Filter.

The Rayleigh scattering is several orders of magnitude less intense than the Mie scattering but substantially wider in terms of spectral range. However, for a proper comparison of scattering light reaching the FRS detector, the filtered Mie scattering intensity needs to be compared to the filtered Rayleigh scattering intensity in order to evaluate if the Mie scattering is too intense for FRS measurements. The filtered Rayleigh scattering in the field must contain a greater integrated intensity than the filtered Mie scattering for quality FRS images. Using the spectral profiles provided in Figure 40 and applying the iodine transmission values up to a maximum optical density of 6, the relative intensities of the spectral profiles drastically change as seen in Figure 41. In this instance, the spectrally integrated signal of the filtered Rayleigh scattering is far greater than the integrated signal of the filtered Mie scattering. In order to assess the ratio of the sources of scattering, the accumulated filtered Rayleigh scattering, I_R, in the observable area can be divided by the accumulated filtered Mie scattering, I_M, in the same observable area in order to evaluate an intensity ratio, I_R / I_M.

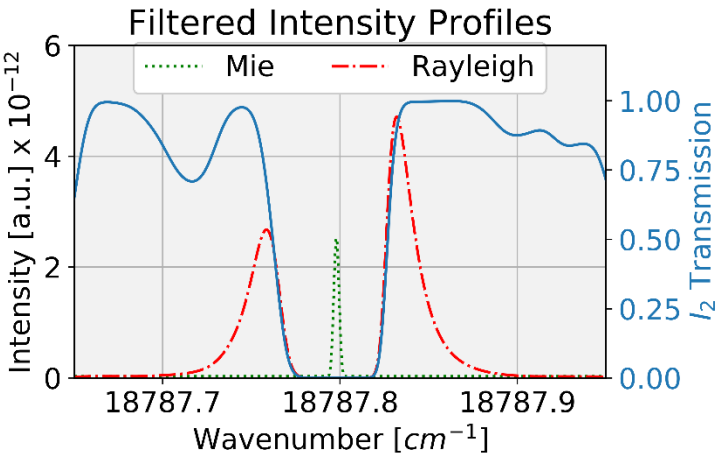

Figure 41: Filtered Intensity Profiles of Mie scattering (Al_2O_3, 4 micron, 25 particles/mm^2) and Rayleigh Scattering (N_2 at 300 K, 1 atm) with OD = 6

For the simulations considered in this investigation, the gaseous conditions were held constant with a composition of air at 300 K and 1 atm.. Solid Al_2O_3 particles with an index of refraction of 1.76 was chosen to represent the Mie scattering with a range of particle diameters and number densities found in prior PIV experiments [58]. Similar to before, Forkey's model was used to calculate vaporous I_2 transmission at the conditions of 85 C and 1 Torr. The incident light characteristics in the calculations represent that commonly seen with seeded, pulsed Nd:YAG laser with a laser linewidth of 0.003 cm^{-1} and tuned to a centerline of 18787.798 cm^{-1}. A summary of all assumed values used in the combine Mie and FRS calculations are provided in Table 6. Mätzler [43] proposed a stable limit of the dimensionless size parameter $x < 10^4$ in order to avoid unstable solutions for the Mie scattering algorithms were x was originally defined in Eq (1). For the majority of calculations below, the maximum particle diameter considered was 5 microns which results in $x = 59$. Some further calculations in the maximum number density and influence of index of refraction extends the maximum particle size to 20 microns, which results in $x = 239$. Both of these conditions are well under the stable limit.

Table 6: Values for Optical Density Calculations

Parameter	Value
Particle Diameter	0.05 – 5 microns
Particle Number Density	5 – 50 particles/mm^2
Particle Index of Refraction	1.76
Gas Species	Air
Gas Temperature	300 K
Gas Pressure	1 atm
Iodine Pressure	1 Torr
Iodine Temperature	85 C
Iodine Cell Length	25.4 cm
Laser Centerline	18787.798 cm^{-1}
Laser linewidth (FWHM)	0.003 cm^{-1}

In most optical diagnostic experiments, the intensity captured by any detector is directly correlated to the intensity of the incident light source used. For all the calculations discussed, the intensity values reported are relative to an incident light source with an intensity value of 1 arbitrary unit or 1 A.U. (e.g. the laser light will have an intensity of 1 A.U while filtered Rayleigh scattering has an approximate intensity of 10^{-9} A.U)

4.3 Results

The filtered Mie scattering was first analyzed without a comparison to filtered Rayleigh scattering. Calculations for filtered Mie scattering intensity were conducted for a constant particle diameter of 5 microns while the particle number density was varied between 5 – 50 particles/mm^2, which is represented by the solid line in Figure 42. This analysis was followed by a similar calculation of holding the particle number density constant at 25 particles/mm^2 while varying the particle diameter 0.05 μm – 5 μm as represented by the dashed line in Figure 42.

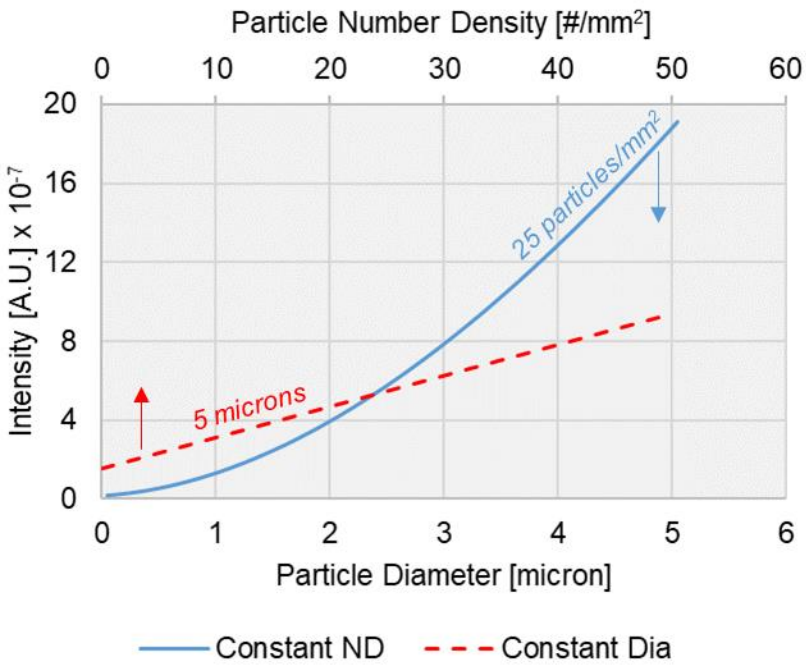

Figure 42: Influence of Particle Number Density and Particle Diameter on Filtered Mie Scatter Intensity

The intensity of the filtered Mie scattering scales linearly with particle number density while a non-linear relation exists between intensity on the particle diameter. For a variation on particle diameter, the intensity changes non-linearly with the slope steadily increasing with the increase of particle diameter. Distinguishing the isolated effects of particle diameter and particle number density on filtered Mie scattering provides better insight when the variation of particle diameter and variation in particle number density are used to assemble a contour plot of filtered Mie scattering intensity as seen in Figure 43.

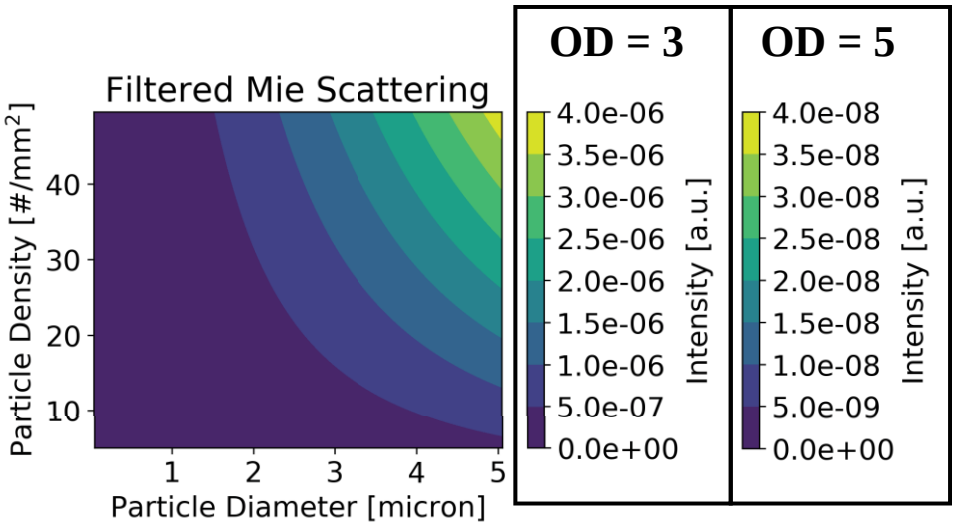

Figure 43: Map of Filtered Mie Scattering Intensity for Different Optical Densities

As expected, an increase in the particle density or particle diameter resulted in an increase in filtered Mie intensity with a non-linear relation seen for variation of particle diameter. Two optical densities were analyzed for the contour plot as noted by the dual colorbars in Figure 43. The tick marks of the colorbars are the same, but the magnitude scale is different for each one, 10^{-6} for OD = 3 and 10^{-8} for OD = 5, which corresponds to the 100x difference in transmission for change in optical density.

The filtered Mie scattering values were compared to the filtered Rayleigh scattering values of air at 1 atm, 300 K. In order to create a relative, normalized scale, the gas number density (ND_R) of air at these conditions was divided by the range of particle number density (ND_M) discussed prior. Similarly, the Rayleigh cross-section (σ_R) was also divided by the cross-section of the Mie particles (σ_M). These normalized scales, ND_R/ND_M and σ_R/σ_M provided an x-axis and y-axis for a similar contour plot as seen in Figure 44. In this plot, the color bar now represents the ratio of filtered Rayleigh intensity, I_R, to filtered Mie intensity, I_M, which is further labeled as Intensity Ratio,

I_R/I_M. A directional notation for increasing/decreasing particle density and increasing/decreasing particle size is provided in Figure 44.

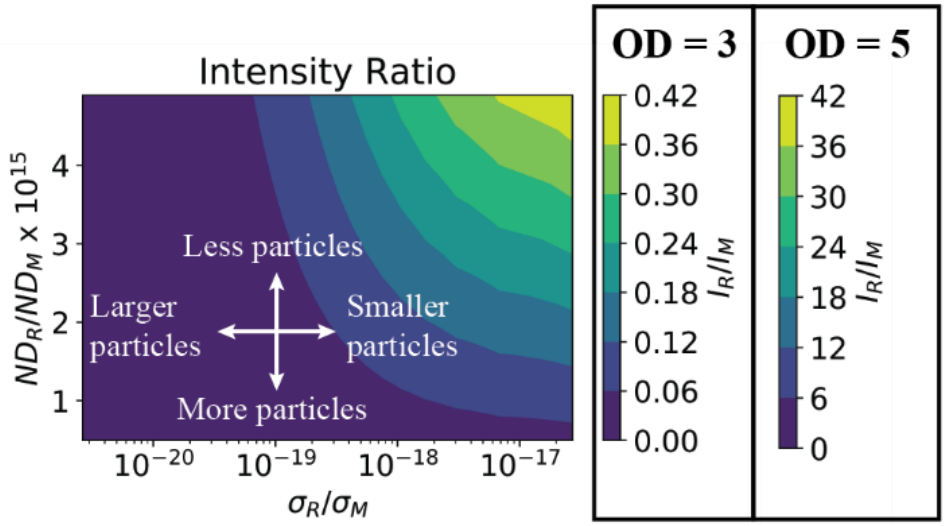

Figure 44: Intensity Ratio for Rayleigh to Mie with directional arrows for more/less particle density or larger/smaller particles (see Table 6 for range of particle variation)

For larger particles or denser particle number, the intensity ratio drops but decreasing the particle number density or size results in higher intensity ratios, as expected. When an optical density of 3 is applied, the entire range of particle density and particle diameter does not produce a condition where the filtered Rayleigh intensity is greater than the filtered Mie intensity. The filtered Rayleigh detector would likely suffer Mie scattering interference in this situation. However, when an optical density of 5 is applied, the intensity ratio greatly increases, which reduces the likelihood of Mie scattering interference.

Knowing the expected intensity ratio of a given experiment provides assistance in determining the quality of the data to expect in given conditions and equipment while also informing an experimentalist whether the experimental effort is worth pursuing as planned. However, designing the experiment to deliver the desired quality of data is ideal.

The calculations performed previously can be iterated for various optical densities until a desired intensity ratio is reached. While the desired I_R/I_M is likely to be much greater than 1, a comparison is drawn between the necessary optical density for I_R/I_M =1 and I_R/I_M = 20. The result of adequate optical density for a minimum intensity ratio of 1 is provided in Figure 45.

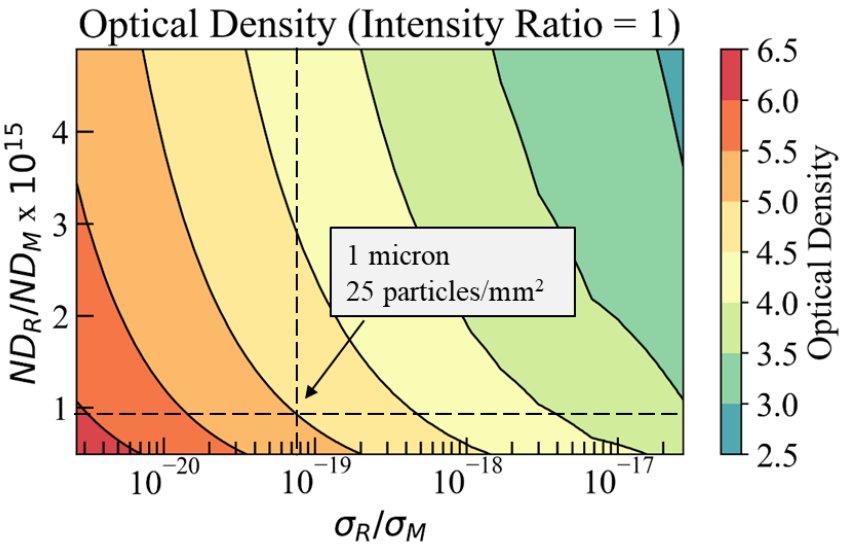

Figure 45: Optical density for a minimum intensity ratio of one

One can see that the needed optical density to achieve a minimum I_R/I_M of 1 can be significant. For example, a seeded flow that contains 1 µm particles with a number density of 25 particles/mm^2 would need an approximate optical density of 5 as noted by the dashed lines in Figure 45. To achieve this level of optical density with a pulsed Nd:YAG laser, one would likely need an external etalon to increase the spectral purity of the laser as seen in [13]. While a minimum intensity ratio of 1 may be acceptable, it is likely that a much higher intensity ratio would be preferred. For further investigation, the optical density iterations were also calculated for a minimum intensity ratio of 20 as seen in Figure 46.

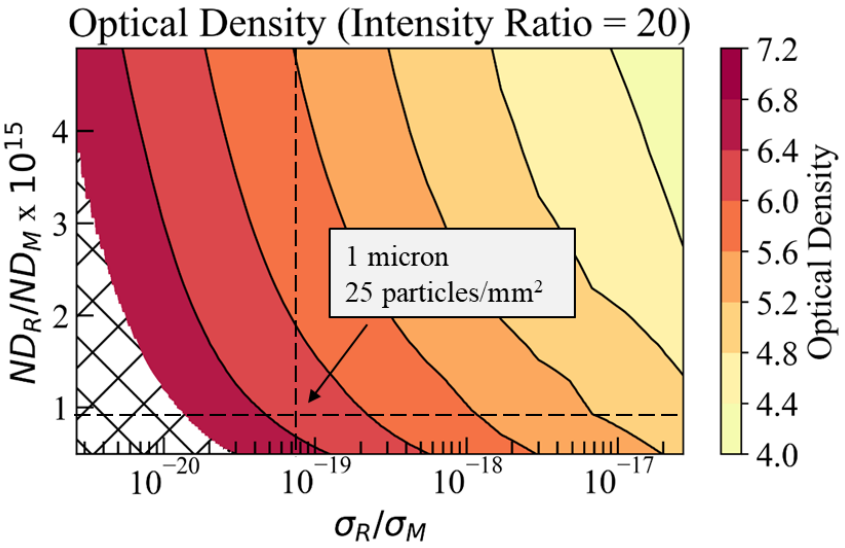

Figure 46: Optical density for minimum intensity ratio of 20

For the same example of 1 µm particles with 25 particles/mm^2, the necessary optical density has increased from 5 to 6.3. This increase in optical density would likely require the spectral purity found in continuous wave lasers. However, continuous wave FRS could have flame-streaking issues if used for transient flames like turbulent flame kernels. Increasing the incident light power and gating the laser would need to be addressed in order to utilize a continuous wave laser for singe-pulse images. The crosshatch area in Figure 46 portrays the optical density values that are above the maximum theoretical OD for a 25.4 cm iodine cell (1 Torr, 85 ºC) near the 18787.798 cm^{-1} absorption band. If the experiment requires optical densities greater that the maximum 6.7 OD in this absorption band, the best solution is likely tuning the incident light to a different absorption of greater optical density. For example, the band centered on 18788.44 cm^{-1}, also known as the major transition P159(39,0)/P103(34,0)/P53(32,0) of $B(^3\Pi_{0+u}) \leftarrow X(\,^1\Sigma_g^+)$ electronic system of I_2 [9], can reach a maximum OD of 12 at the same iodine temperature and pressure.

One of the major assumption made during analysis of PIV particles in FRS measured flow was evaluating the signal at a range of *constant* number density and *constant* diameter. In reality, the particle density is distributed across a range of particle diameters. Liquid droplet size distribution is typically similar to a normal distribution due to droplet break-up and collisions. Solid particle size distribution takes the form a gamma distribution due to particle agglomeration [61-63]. The solid particle distribution can be represented by a randomly generated gamma distribution across 1000 points with shape = 3 and scale = 3, which is provided in Figure 47.

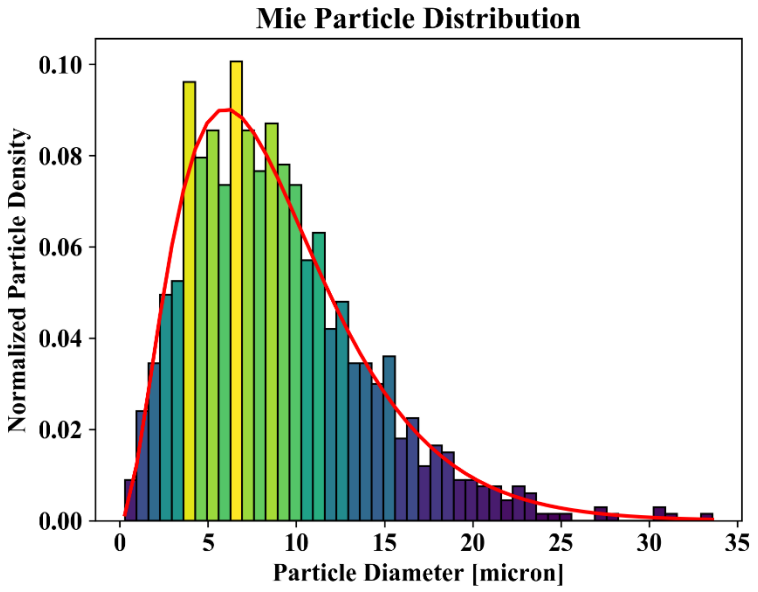

Figure 47: Normalized Mie Particle Distribution

This type of distribution comes from a specified nominal PIV particle size (5 microns) with some uncertainty in the manufacturing of the particles diameter providing a normal distribution. However, after the particle injection and interaction with the flow field, particles collide and stick to each other, essentially forming a small percentage of larger particles. This agglomeration results in the long tail on the right side of the size

distribution where few particles exists, but the particles are significantly larger than the average. The large particles may seem insignificant at first glance. However, more is revealed when each particle size bin is calculated for particle intensity that is scaled to the respective normalized particle count as seen in Figure 48.

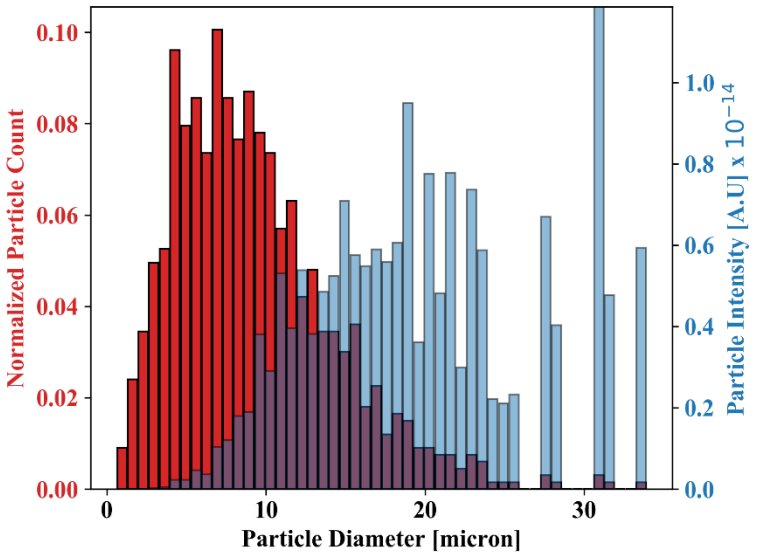

Figure 48: Normalized Particle Count and Particle Intensity

While the majority of particles are less than 12 microns, the intensity from these smaller particles are quite negligible compared to the larger particles. Much greater intensity comes from the larger particles even though few exists in relative terms. This contrast stresses the important of particle control in PIV experiments although many factors make this difficult [64]. If the particle or droplet size is allowed to grow too large due to interactions in the flow, significant light scatter can be expected, which could interfere with FRS images.

CHAPTER V

CONCLUSIONS

The previously discussed studies provide improvements in each facet of conducting filtering Rayleigh scattering: the design of the experiment, the experimental strategy, and the processing of experimental data. The determination of adequate optical density for expected flow conditions is critical for experimental design of simultaneous PIV and FRS experiments. The continuous wave FRS strategy can improve upon FRS experimentation in terms of data quality and operability. Finally, adapting novel digital image filtering techniques that can mitigate particle presence further improves data processing and quality. A concluding statement for each of these investigations is provided below.

5.1 Continuous Wave Filtered Rayleigh Scattering of Lean, Premixed H_2-Air Tubular Flames

The application of continuous wave lasers for filtering Rayleigh scattering provides a method to use more spectrally pure light in comparison to the pulsed laser method that has been the historical standard for FRS. The higher spectral purity of the continuous wave laser leads to greater optical density of the iodine filter and better filtering of laser scattering from the burner wall. When compared to the pulsed laser methods, the continuous wave FRS has better uncertainty and signal-to-noise ratio for the same input energy. Additionally, the continuous wave method enables an easier operation

for planar measurement inside the tubular burner and likely other burners. This configuration enabled an axial measurement of H_2-air tubular flames structure that have only been observed qualitatively until now. The axial structure does not display the curvature seen in the radial plane of the cellular, tubular flames, which is due to the dominant momentum over buoyancy effects at a stretch rate of 200 s^{-1}. The FRS temperature measurements in the radial plane agree with prior Raman spectroscopy temperature measurements of premixed H_2-air, cellular tubular flames.

Possible improvements for the continuous wave FRS include adapting the system for transient flames where a pulse system is typically used for the short exposure times. The continuous wave FRS would need to have high power to achieve the same energy over time seen in pulsed systems. Additionally, the continuous laser system would need to be gated or chopped in order to achieve the 'pulse like' nature.

5.2 Digital Image Filtering for Particles in Filtered Rayleigh Scattering Images

Filtered Rayleigh scattering suppresses Mie scattering by use of a molecular iodine filter that absorbs the Mie scattering while allowing the Rayleigh scattering to pass. However, Mie scattering may still reach the FRS detector, particularly in the case of large particles or droplets that produce Mie scattering too intense for the molecular filtering to absorb. Digital image processing provides methods to reduce the influence of Mie scattering signals on the FRS determined temperature. Median filtering has been used to reduce the Gaussian noise in the FRS images in prior studies, but it does not mitigate the particles' presence in the images. An iterative Contaminant Rejection filter was developed with a similar approach as weighted median filtering but with two major

changes: (1) logical application to pixels that contain high intensities from particle Mie scattering and (2) the filter could be iterated until the particle presence was reduced without filtering the remaining image of the gas structure. By selecting an area of the image that contains the expected image signal and noise (no apparent Mie scattering present), the threshold value of the iterative Contaminant Rejection filter could be calculated from image values.

Turbulent flame kernel images were taken that contained many large contaminants that were approximately 1 mm in diameter. The iCR filter was applied iteratively to completely replace the presence of particles with signals of the gas surrounding the particles. The iterative Contaminant Rejection filter demonstrated a drastic improvement on reducing the apparent particle area and peak intensities of the particles as well as improving the signal-to-noise ratio of the FRS images. Even better results were achieved when the iterative Contaminant Rejection filter preceded the application of a traditional median filter. This combination severely reduced the presence of the particles and smoothed out the noise in the image without smoothing out the gas structure and flame edges. After processing through both filters, the flame kernel's temperature and flame boundary were more clearly defined when compared with the temperature and boundary determined from raw images.

For future development of the particle rejection filter, several considerations could be made. An automated method to determine the expected signal magnitude and noise level without the presence of particles could be beneficial when compared to the user defining an image section to determine this from. The user-defined option leaves more opportunity for human error in the process. Additionally, the filter size could be

modified between iterations of the particle rejection filter. For sufficiently large particles, the possibility exists of the same median values being propagated into the particle area if filter size is kept the same for each iteration, although the overall effect of reusing median values has not been evaluated.

5.3 Considerations for Simultaneous Filtered Rayleigh Scattering and Particle Image Velocimetry

While strategies exist to mitigate the presence of particles in FRS images, proper experimental design should be conducted first to prevent the severity of Mie scattering. While mildly successful FRS experiments have been conducted simultaneously with PIV experiments, the criteria for such successful experiments have not been well defined. Calculations were conducted using Tenti S6 model [7] to determine Rayleigh scattering signals, Mätzler algorithms [43] for Mie scattering signals, and Forkey's model [9] for iodine transmission. The filtered Rayleigh scattering signal and filtered Mie scattering signal were determined for a range of conditions.

The ratio of the filtered Rayleigh scattering signal to filtered Mie scattering signal was determined to predict the quality of the image data on an FRS detector. A desired signal ratio of Rayleigh scattering to Mie scattering could be set in order to determine the necessary optical density needed for a successful experiment. These values are necessary for a proper experimental design and deciding the right equipment for the experiment such as laser specs (centerline, linewidth, and spectral purity), molecular filter length, the PIV particle's nominal size, particle number density and predicted distribution, and particle material (index of refraction). This experimental design approach would benefit from the adaptation to a distribution of particle or droplet sizes. Additionally,

experiments would need to be conducted in order to validate the theoretical predications calculated.

REFERENCES

[1] R. B. Miles, W. R. Lempert and J. N. Forkey, "Laser Rayleigh Scattering," *Meas. Sci. Technol.*, vol. 12, pp. R33 - R51, 2001.

[2] F. Zhao and H. Hiroyasu, "The applications of laser Rayleigh scattering to combustion diagnostics," *Progress in Energy and Combustion Science,* vol. 19, no. 6, pp. 447-485, 1993.

[3] G. S. Elliot, N. Glumac and C. D. Carter, "Molecular filtered Rayleigh scattering applied to combustion," *Meas. Sci. Technol.*, vol. 12, pp. 452-466, 2001.

[4] S. P. Kearney, S. J. Beresh, T. W. Grasser and R. W. Schefer, "Filtered Rayleigh scattering diagnostic for multi-parameter thermal-fluids measurements SAND2004-0158," Sandia National Labs, 2004.

[5] J. N. Forkey, "Development and Demonstration of Filtered Rayleigh Scattering: A Laser Based Flow Diagnostic for Planar Measurement of Velocity, Temperature and Pressure," Ph.D. Thesis, Princeton University, 1996.

[6] R. W. Pitz., R. Cattolica, F. Robben and L. Talbot, "Temperature and densities in a hydrogen-air flame from Rayleigh scattering," *Combustion and Flame,* vol. 27, pp. 313-320, 1976.

[7] G. Tenti, C. D. Boley and R. C. Desai, "On the Kinetic Model Description of Rayleigh-Brillouin Scattering from Molecular Gases," *Canadian Journal of Physics,* vol. 52, no. 4, 1974.

[8] T. A. McManus, I. T. Monje and J. A. Sutton, "Experimental assessment of the Tenti S6 model for combustion-relevant gases and filtered Rayleigh scattering

applications," *Applied Physics B,* vol. 125:13, no. https://doi.org/10.1007/s00340-018-7121-8, 2019.

[9] J. N. Forkey, W. R. Lempert and R. B. Miles, "Corrected and calibrated I_2 absorption model at frequency-doubled Nd:YAG laser wavelengths," *Applied Optics,* vol. 36, no. 27, pp. 6729 - 6738, 1997.

[10] A. Yalin and R. Miles, "Ultraviolet filtered Rayleigh scattering temperature measurements using a mercury filter," *Optics Letters,* vol. 24, no. 9, pp. 590-592, 1999.

[11] M. Boguszko and G. S. Elliot, "On the use of filtered Rayleigh scattering for measurements in compressible flows and thermal fields," *Experiments in Fluids,* vol. 38, pp. 33 - 49, 2005.

[12] M. Boguszko and G. S. Elliot, "Property measurement utilizing atomic/molecular filter-based diagnostics," *Progress in Aerospace Sciences,* vol. 41, pp. 93-142, 2005.

[13] J. A. Sutton and R. A. Patton, "Improvements in filtered Rayleigh scattering measurements using Fabry-Perot etalons for spectral filtering of pulsed, 532-nm Nd:YAG output," *Appl. Phys. B,* vol. 116, pp. 681-698, 2014.

[14] R. A. Patton and J. A. Sutton, "Seed laser power effects on the spectral purity of Q-switched Nd:YAG lasers and implications for filtered rayleigh scattering measurements," *Applied Physics B,* vol. 111, no. 3, pp. 457-468, 2013.

[15] S. Ishizuka, "Characteristics of Tubular Flames," *Prog. Energy Combust. Sci.,* vol. 19, pp. 187-226, 1993.

[16] P. Wang, J. A. Wehrmeyer and R. W. Pitz, "Stretch Rate of Tubular Premixed Flames," *Combustion and Flame,* vol. 145, pp. 401-414, 2006.

[17] Y. Wang, R. Hu and R. W. Pitz, "Extinction and cellular instability of premixed tubular flames," *Proceedings of the Combustion Institute,* vol. 32, no. 1, pp. 1141-1147, 2009.

[18] C. A. Hall and R. W. Pitz, "Experimental and numerical study of H_2-air non-premixed cellular tubular flames," *Proceedings of the Combustion Institute,* vol. 36, no. 1, pp. 1595-1602, 2017.

[19] S. Hu, P. Wang, R. W. Pitz and M. D. Smooke, "Experimental and numerical investigation of non-premixed tubular flames," *Proceedings of the Combustion Institute,* vol. 31, pp. 1093-10999, 2007.

[20] H. Devathi, C. A. Hall and R. W. Pitz, "Numerical study of the structure and NO emission characteristics of N_2- and CO_2-diluted tubular diffusion flames," *Energies,* vol. 12, no. 8, 2019.

[21] D. C. Tinker, "Partially premixed tubular flames: an experimental survey," M.S. Thesis, Vanderbilt University, 2016.

[22] C. A. Hall, D. K. Waruna, N. Jiang, J. R. Gord and R. W. Pitz, "Minor-species structure of premixed cellular tubular flames," *Proceedings of the Combustion Institute,* vol. 35, no. 1, pp. 1107-1114, 2015.

[23] C. A. Hall and R. W. Pitz, "A structural study of premixed hydrogen-air cellular tubular flames," in *Proceedings of the Combustion Institute,* 2013.

[24] C. A. Hall and R. W. Pitz, "Numerical simulation of premixed H_2-air cellular tubular flames," *Combustion Theory and Modelling,* vol. 20, no. 2, pp. 328-348, 2016.

[25] R. W. Pitz, S. Hu and P. Wang, "Tubular premixed and diffusion flames: Effect of stretch and curvature," *Progress in Energy and Combustion Science,* vol. 42, pp. 1-34, 2014.

[26] V. N. Kurdyumov, "Diffusive-thermal instability of premixed tubular flames," *Combustion and Flame,* vol. 158, no. 9, pp. 1718-1726, 2011.

[27] C. D. Carpenter and R. W. Pitz, "Filtered Rayleigh scattering measurements of temperature in cellular tubular flames," *Experiments in Fluids,* vol. 61, no. 45, 2020.

[28] C. A. Hall, "Instability of premixed lean hydrogen laminar tubular flames," Ph.D. Thesis, Vanderbilt University, 2016.

[29] M. P. Burke, M. Chaos, Y. Ju, F. L. Dryer and S. J. Klippenstein, "Comprehensive H2/O2 kinetic model for high-pressure combustion," *International Journal of Chemical Kinetics*, vol. 44, pp. 444-472, 2012.

[30] R. C. Gonzalez and R. E. Woods, Digital Image Processing, New York: Pearson, 2008.

[31] T. R. Crimmins, "Geometric filter for speckle reduction," *Applied Optics*, vol. 24, no. 10, pp. 1438 - 1443, 1985.

[32] F. Banterle, M. Corsini, P. Cignoni and R. Scopigno, "A low-memory, straightforward and fast bilateral filter through subsampling in spatial domain," *Computer Graphics forum*, vol. 31, no. 1, pp. 19 - 32, 2012.

[33] C. Tomasi and R. Manduchi, "Bilateral Filtering for Gray and Color Images," in *IEEE International Conference on Computer Vision*, Bombay, 1998.

[34] D. Most and A. Leipertz, "Simultaneous two-dimensional flow velocity and gas temperature measurements by use of a combined particle image velocimetry and filtered Rayleigh scattering technique," *Applied Optics*, vol. 40, no. 30, pp. 5379 - 5387, 2001.

[35] J. W. Tukey, Exploratory Data Analysis, Reading: Addison-Wesley, 1974.

[36] T. A. McManus and J. A. Sutton, "Simultaneous Velocity and Temperature Measurements in Turbulent Nonpremixed Flames Using Particle Image Velocimetry and Filtered Rayleigh Scattering," in *11th U.S. National Combustion Meeting*, Pasadena, 2019.

[37] S. Sardy, P. Tseng and A. Bruce, "Robust wavelet denoising," *IEEE Transacations on Signal Processing*, vol. 49, no. 6, pp. 1146-1152, 2001.

[38] P. Hedaoo and S. Godbole, "Wavelet thresholding approach for image denoising," *International Journal of Network Security & Its Applications*, vol. 3, no. 4, pp. 16-21, 2011.

[39] W. K. Pratt, Digital Image Processing, New York: John Wiley and Sons, Inc., 1978.

[40] G. Mie, "Pioneering mathematical description of scattering by spheres," *Annalen der Physik,* vol. 25, no. 377, 1908.

[41] P. Debye, "Der Lichtdruck auf Kugeln von beliebigem Material," *Annalen der Physik,* vol. 30, no. 57, 1909.

[42] H. C. van de Hulst, Light Scattering by Small Particles, New York: Dover Publications Inc., 1951.

[43] C. Mätzler, "MATLAB functions for Mie scattering and absorption," *IAP Res. Rep.,* Vols. No. 02-08, 2002.

[44] C. F. Bohren and D. R. Huffman, Absorption and scattering of light by small particles, New York: John Wiley & Sons, 1983.

[45] E. Kreyzig, Advanced Engineering Mathematics, 9th ed, New York: John Wiley & sons, Inc., 2006.

[46] N. Beverini, N. Poli, D. Sutyrin, F. Y. Wang, M. Schioppo, M. G. Tarallo and G. M. Tino, "Absolute frequency measurement of unstable lasers with optical frequency combs," in *Proc. SPIE 7993, ICONO 2010: International Conference on Coherent and Nonlinear Optics 79931I*, 2010.

[47] J. A. Sutton and J. F. Driscoll, "Rayleigh scattering cross sections of combustion species at 266, 355, and 532 nm for thermometry applications," *Optics letters,* vol. 29, no. 22, pp. 2620-2622, 2004.

[48] I. T. Monje and J. A. Sutton, "Filtered Rayleigh scattering thermometry in premixed flames," *2018 AIAA Aerospace Sciences Meeting, AIAA SciTech Forum,* Vols. AIAA 2018-1772, 2018.

[49] E. Hecht, Optics, 5th ed., New York: Pearson Education, Incorporated, 2017.

[50] N. J. Brown, L. A. J. Bastien and P. N. Price, "Transport properties for combustion modeling.," *Progress in Energy and Combustion Science,* vol. 37, pp. 562-582, 2011.

[51] G. Stockhausen, U. Doll and C. Willert, "Combined filtered Rayleigh and Mie scattering for simultaneous planar temperature and velocity measurements," in *15th Int. Symp. on Applications of Laser Techniques to Fluid Mechanics*, Lisbon, 2010.

[52] O. Gulder, "Turbulent premixed flame propagation models for different combustion regimes," *Symposium (International) on Combustion,* vol. 23, no. 1, pp. 743-750, 1991.

[53] M. Dieter and A. Leipertz, "Simultaneous two-dimensional flow velocity and gas temperature measurements by use of a combined particle image velocimetry and filtered Rayleigh scattering technique," *Applied Optics,* vol. 40, no. 30, pp. 5379-5387, 2001.

[54] R. Patton and P. Sutton, "Development of Gas-Phase Mixing Measurements in Turbulent Spray Flows Using Filtered Rayleigh Scattering," in *51st AIAA Aerospace Sciences Meeting*, Grapevine, 2013.

[55] D. Hoffman and A. Leipert, "Temperature field measurements in a sooting flame by filtered Rayleigh scattering," *Symposium (International) on Combustion,* vol. 26, no. 1, pp. 945-950, 1996.

[56] D. Hoffman, K. Munch and A. Leipertz, "Two-dimensional temperature determination in sooting flames by filtered Rayleigh scatering," *Optics Letters,* vol. 21, no. 7, pp. 525-527, 1996.

[57] L. Most, F. Dinkelacker and A. Leipertz, "Direction determination of the turbulent flux by simultaneous application of filtered Rayleigh scattering thermometry and particle image velocimetry," *Proceedings of the Combustion Institute,* vol. 29, pp. 2669-2677, 2002.

[58] D. Dabiri, "Digital particle image thermometry/velocimetry: a review," *Experiments in Fluids,* vol. 46, pp. 191-241, 2009.

[59] J. R. DeVore, "Refractive indices of rutile and sphalerite," *Journal of the Optical Society of America,* vol. 41, no. 6, pp. 416-419, 1951.

[60] R. Zakaria and P. Bryanston-Cross, "Light scattering efficiency of oil smoke seeding droplets in PIV systems," in *Photonics Global Conference (PGC)*, Singapore, pp. 1-5, 2012.

[61] M. Legrand, J. Nogueira, P. A. Rodriguez, A. Lecuona and R. Jimenez, "Generation and droplet size distribution of tracer particles for PIV measurements in air, using propylene glycol/water solution," *Experimental Thermal and Fluid Science*, vol. 81, pp. 1-8, 2017.

[62] T. van Overbrüggen, M. Klass, J. Soria and W. Schröder, "Experimental analysis of particle sizes for PIV measurements," *Measurement Science and Technology*, vol. 27, p. 094009, 2016.

[63] S. Burgmann, N. Van Der Schoot, C. Asbach, J. Wartman and R. Lindken, "Analysis of tracer particle characteristics for micro PIV in wall-bounded gas flows," *La Houille Blanche*, vol. 4, pp. 55-61, 2011.

[64] F. Scarano, "Overview of PIV in supersonic flows," *Topics in Applied Physics*, vol. 112, pp. 445-463, 2008.

APPENDIX A

PYTHON CODE FOR TENTI S6

```
import numpy as np
import math
import scipy
from scipy.integrate import quad
import gasProp as gp

#-------------------------------------
# CRBS main routine
#-------------------------------------
def crbs_main(temp,p_atm, species, theta,lam):
    """
    temp = temperature of gas [Kelvin]
    p_atm = pressure of gas [atm]
    species = species name (i.e. O2, H2) - must be string recognized in gasProp
    theta = angle between incident and detection [degrees]
    """
    #non-dimensional resolution
    n_xi = 300
    xi_lef = -3.0
    xi_rgt = 3.0

    #-------------------------------------
    # laser parameters
    #-------------------------------------

    kb = 1.38E-23
    angle = (theta/2.)*(np.pi/180.)
    k = np.sin(angle)*4.*np.pi/lam

    #-------------------------------------
    # gas quantities
    #-------------------------------------
    #retrieve gas properties
    m_m, visc, bulk_vis, thermal_cond, c_int, n, rhov, Ra, xN2 = gp.getData(species)
    v0 = np.sqrt(2.0*kb*temp/m_m)

    p_pa = p_atm* 101325.
    #gas molecule number density (per 1 m^3)
    n0 = p_pa / (temp*kb)

    #-------------------------------------------------
    # dimensionless numbers calculated from gas dynamics
    #-------------------------------------------------

    y = n0*kb*temp/(k*v0*visc)
    c_tr = 3.0/2.0
    gamma_int = c_int/(c_tr + c_int)
    rlx_int = 1.5 * bulk_vis/(visc*gamma_int)
    eukenf = m_m*thermal_cond/(visc*kb*(c_tr + c_int))
```

```
    #resolution between steps
    dxi = (xi_rgt - xi_lef)/(2.0*n_xi)

    #xi(i) is the dimensionless frequency
    xi = []
    om = []
    wn = []
    c0 = 299792458. #speed of light
    for i in range(0, 2*n_xi, 1):
        dmxi = xi_lef+dxi*(i)
        xi.append(dmxi)
        om.append(dmxi*k*v0/(2*np.pi))
        wn.append(dmxi*k*v0/(2*np.pi)/(c0*100.))

    cohsig, cohsigN, coharea, sptsig, sptsigN, sptarea \
        = crbs6(y,rlx_int,eukenf,c_int,c_tr,xi,n_xi)

    return abs(np.array(cohsig)), abs(np.array(cohsigN)), np.array(wn), coharea,np.array(xi)

#-------------------------------------------------------------------------------
# crbs6
#-------------------------------------------------------------------------------
def crbs6(y6,rlx_int,eukenf,c_int,c_tr,xi,n_xi):
    """
    crbs6 calculate the coherent Rayleigh-Brillouin scattering line
    shape using the six moment model described by Xingguo Pan
    "Coherent Rayleigh-Brillouin Scattering," PhD Thesis, Princeton University
    ------------------------------------------------------------
    calls:
    w0_func to calculate w0(xi+i*y)
    gaussj to solve the linear equations using Gaussian elimination
    ------------------------------------------------------------
    input parameters:
    y: the 'y' parametr
    rlx_int: the internal relaxation number
    eukenf: the Euken factor, c_int and c_tr: internal and translational
    heat capacities. All above are dimensionless
    xi[-n_xi:n_xi]: the dimensionless frequency array omega/(k*v0^2)
    cohsig[-n_xi:n_xi]:the CRBS lineshape
    sptsig[-n_xi:n_xi]: the spontaneous RBS lineshape using s6 model
        Area under the curve is normalized to one
    Adapated from FORTRAN code: Xingguo Pan, Princeton University, 2002.
    ------------------------------------------------------------
    """
    gamma_int = c_int / (c_tr + c_int)
    k020 = -y6
    k100 = -gamma_int * y6 / rlx_int
    k001 = k100 * c_tr/c_int
    k100001 = k100*np.sqrt(c_tr/c_int)
    k110 = k100*5.0/6.0 + k020*2.0/3.0
```

```
k011110 = k100*np.sqrt(5.0/(8.0*c_int))
k_nu = 0.4*(1.5+c_int)+(3.0+c_int) / (2.0*rlx_int) \
   + 9.0*eukenf/(16*rlx_int**2)
k_de = -1.0+(4.0/15.0)*eukenf*(1.5+c_int)+(c_int/3.0)*eukenf/rlx_int
k_co= -y6*(2.0*gamma_int/3.0)
k011 = k_co*k_nu/k_de

#initialize area and list of coherent and spontaneous scatter
coharea = 0.
sptarea = 0.
coha = []
spta = []
cohsig = []
sptsig = []

#iterate
for i in range(0,2*n_xi,1):
   z = xi[i]+1j*y6
   w0 = w0_func(xi[i],y6)
   w1 = -math.sqrt(np.pi)+z*w0
   w2 = z*w1
   w3 = -0.5*math.sqrt(np.pi)+z*w2
   w4 = z*w3
   w5 = -3.*math.sqrt(np.pi)/4.+z*w4
   w6 = z*w5

   # I coefficient
   i0000 = w0/(math.sqrt(np.pi))
   i0100 = (z*w0-math.sqrt(np.pi))*math.sqrt(2./np.pi)
   i0001 = i0100

   i0010 = (2.*w2-w0)/(math.sqrt(6.*np.pi))
   i1000 = i0010
   i0011 = (2.*w3 -3.*w1)/(math.sqrt(5.*np.pi))
   i1100 = i0011

   i0101 = 2.*w2/math.sqrt(np.pi)
   i0110 = (-w1 +2.*w3)/math.sqrt(3.*np.pi)
   i1001 = i0110

   i0111 = (-3.*w2 +2.*w4)*math.sqrt(2./(5.*np.pi))
   i1101 = i0111
   i1111 = (13.*w2 -12.*w4 +4.*w6)/(5.*math.sqrt(np.pi))

   i1010 = (5.*w0 -4.*w2 +4.*w4)/(6.*math.sqrt(np.pi))
   i1110 = (7.*w1 -8.*w3 +4.*w5)/math.sqrt(30.*np.pi)
   i1011 = i1110

   # The equation to sovle is Ax = B
   # matrix A
```

```
        am = np.matrix(\
        [[-k020*i0000+1j,-k020*i0100  ,(k020-k110)*i1100  ,(k020-k100)*i1000  ,k100001*i1000
,k011110*i1100],
         [-k020*i0001  ,-k020*i0101+1j,(k020-k110)*i1101  ,(k020-k100)*i1001  ,k100001*i1001
,k011110*i1101],
        [-k020*i0011  ,-k020*i0111  ,(k020-k110)*i1111-1j,(k020-k100)*i1011  ,k100001*i1011
,k011110*i1111],
        [-k020*i0010  ,-k020*i0110  ,(k020-k110)*i1110  ,(k020-k100)*i1010-1j,k100001*i1010
,k011110*i1110],
        [0.         ,0.         ,-k011110*i0100    ,-k100001*i0000    ,(k001-k020)*i0000+1j,(k011-
k020)*i0100],
        [0.         ,0.         ,-k011110*i0101    ,-k100001*i0001    ,(k001-k020)*i0001  ,(k011-
k020)*i0101+1j]])

        #matrix B
        #1st col = coherent Rayleigh-Brillouin scattering
        #2nd col = spontaneous Rayleigh-Brilloin scattering
        bm = np.matrix([[-i0100,-i0000],
                        [-i0101,-i0001],
                        [-i0111,-i0011],
                        [-i0110,-i0010],
                        [0.,0.],
                        [0.,0.]])

        #get inverse of a and solution for A*b = C
        bSol = np.linalg.solve(am,bm)

        cohsig.append(bSol[0,0] * np.conjugate(bSol[0,0]))
        sptsig.append(2.*bSol[0,1].real)

        coharea = coharea + abs(cohsig[i])
        coha.append(cohsig[i])
        sptarea = sptarea + sptsig[i]
        spta.append(sptsig[i])
        #end of loop

    cohsigN=[]
    sptsigN=[]

    for k in range(0,2*n_xi):
        cohsigN.append(cohsig[k]*2*n_xi/(coharea*(xi[2*n_xi-1]-xi[0])))
        sptsigN.append(sptsig[k]*2*n_xi/(sptarea*(xi[2*n_xi-1]-xi[0])))

    cohsigN = np.array(np.real(cohsigN))
    sptsigN = np.array(np.real(sptsigN))
    coha = np.array(np.real(coha))
    spta = np.array(np.real(spta))

    return cohsig, cohsigN, coharea, sptsig, sptsigN, sptarea
#
```

```
#-----------------------------------------------------------------------
# w0_func
#-----------------------------------------------------------------------
def w0_func(xi,y):
   eps = 1E-5 #tolerance for integration error
#    j = complex(0.,1.)

   z = xi+y*1j
   if y < 0.02:
      #solve differential for small y's
      w0 = -1j*np.pi

      #two step integration scheme
      z1 = 0. +1j*y
      h1 = np.absolute(z1)/5.
      hmin = 0.

      h1 = np.absolute(z-z1)/5.
      w0,nok,nbad = cpxode(w0,z1,z,eps,h1,hmin)

   elif y > 0.02:
      #for large y's, use direct integration
      #precision controlled Simpson's rule
      left = -20.
      right = 20.
#       w0 = qsimp(z,left,right,eps)
      w0 = complex_quadrature(lambda q: np.exp(-q*q)/(z-q), left, right)
   else:
      print('y must be greater than or equal to zero.')

   return w0

#-----------------------------------------------------------------------
# cpxode
#-----------------------------------------------------------
def cpxode(ystart,x1,x2,eps,h1,hmin,nok,nbad):
#Runge-Kutta driver with adaptive stepsize control. Integrate the
#starting value ystart from xl to x2 with accuracy eps, storing the
#intermediate results in the common block /path/, h1 should be set
#as a guessed first stepsize, hmin as the minimum allowed stepsize
#(can be zero). On output nok and nbad are the number of good and bad
#(but retried and fixed steps taken, and ystart is replaced by vlues at
#the end of the integration interval, derivs is the user-suppliedXX=2
#subroutine for claculating the right-hand side derivative, while
#rkqs is the name of the stepper routine to be used. /path/ contains
#its own information about how often an intermediate value is to
#be stored.
   maxstp = 10000
   kmaxx = 200
   tiny = 1*10**-30
```

```
x = x1
h = abs(h1)

#don't bother if the endpoint is the starting
if (np.real(x2) == np.real(x1)) and (np.imag(x2) == np.imag(x1)):
   return ystart,x1,x2,eps,h1,hmin,nok,nbad

cdirec = (x2-x1)/abs(x2-x1)
cstep = h*cdirec
nok = 0
nbad = 0
kount = 0
kmax = 0
y = ystart
xp = [None]*kmaxx
yp = [None]*kmaxx
xsav = 0
dxsav = 0

#assure storage of first step
if kmax > 0: xsav = x - 2.0 *dxsav

#take at most MAXSTP
for step in range(0,maxstp):
   dydx = derivs(x,y)

   #scaling used to monitor accuracy
   yscal = abs(y)+abs(cstep*dydx)+tiny
   if kmax > 0:
      if abs(x-xsav) > abs(dxsav):
         #store intermediate results
         if kount < (kmax - 1):
            kount = kount + 1
            xp[kount] = x
            yp[kount] = y
            xsav = x

   #if stepsize can overshoot, decrease
   if abs(x+cstep-x1) > abs(x2-x1):
      h = abs(x2-x1)-abs(x-x1)
   hdid, hnext = rkqs(y,dydx,x,h,cdirec,eps,yscal)
   if hdid == h:
      nok = nok + 1
   else:
      nbad = nbad + 1

   if abs(x-x1) > abs(x2 - x1):
      #are we done yet?
      ystart = y
```

```
            if kmax != 0:
               kount = kount = 1
               xp[kount] = x
               yp[kount] = y
            return
         if abs(hnext) < hmin:
            print('stepsize smaller than minimum is odeint')
         h = hnext
      print('too many steps in cpxode')
      return ystart,x1,x2,eps,h1,hmin,nok,nbad

#-----------------------------------------------------------------------
# rkqs
#-------------------------------------------------------------
#Fifth-order Runge-Kutta step with monitoring of local truncation
#error to ensure accuracy and adjust stepsize. Input are the
#dependent variable y and its derivative dydx at the starting
#value of the independent variable x. Also input are the stepsize
#to be attempted htry, the required accuracy eps, and the vector
#yscal against which the error is scaled. On output, y and x are
#replaced by their new value, hdid is the stepsize that was
#actually accomplished, and hnext is the estimated next stepsize.
#derivs is the user-supplied subroutine that computes the right-
#hand side derivatives.
def rkqs(y,dydx,x,htry,cdirec,eps,yscal):
   safety = 0.9
   pgrow = -0.2
   pshrnk = -0.25
   errcon = 1.89*10**-4

   #set stepsize to the initial trial value
   h = htry
   cstep = h*cdirec
   ytemp,yerr = rkck(y,dydx,x,cstep)

   #evaluate accuracy
   errmax = 0.
   errmax = max(errmax,abs(yerr/yscal))

   #scale relative to required tolerance
   errmax = errmax/eps
   if errmax > 1:
      #truncation error too large, reduce stepsize
      htemp = safety*h*(errmax**pshrnk)
      h = max(abs(htemp),0.1*abs(h))*np.sign(h)
      #no more than a factor of 10 reduce
      xnew = x + h*cdirec
      if xnew is x:
         print('stepsize underflow in rkqs')
         #goto line with cstep = h*cdirec
```

```
    else:
       #step succeeded. Compute size of next step.
       if errmax > errcon:
          #no more than a factor of 5 increase.
          hnext = safety*h*(errmax*pgrow)
       else:
          hnext = 5.*h
       hdid = h
       x = x+h*cdirec
       y = ytemp

    return hdid, hnext

#-----------------------------------------------------------------------
# derivs
#-------------------------------------------------------------
#The differential equation for wO. See "The Plasma Dispersion Function"
#by B. D. Fried and S. D. Conte, Academic Press (1961) for details.
#w0'(z) = 2*sqrt(np.pi)-2*z*w0, with w0(0)= -i*np.pi.

def derivs(z,w0):
    dwdz = 3.54490770181103 - 2.0*z*w0
    return dwdz
#-----------------------------------------------------------------------
# rkqs
#-------------------------------------------------------------
def rkck(y,dydx,x,cstep):
    a2 = 0.2
    a3 = 0.3
    a4 = 0.6
    a5 = 1.0
    a6 = 0.875

    b21 = 0.2

    b31 = 3./40.
    b32 = 9./40.

    b41 = 0.3
    b42 = -9.
    b43 = 1.2

    b51 = -11./54.
    b52 = 2.5
    b53 = -70./27.
    b54 = 35./27.

    b61 = 1631./55296.
    b62 = 175./512.
    b63 = 575./13824.
```

```
    b64 = 44275./110592.
    b65 = 253./4096.

    c1 = 37./378.
    c3 = 250./621.
    c4 = 125./594.
    c6 = 512./1771.

    dc1 = c1 - 2825./27648.
    dc3 = c3 - 18575./48384.
    dc4 = c4 - 13525./55296.
    dc5 = -277./14336.
    dc6 = c6 - 0.25

    #first step
    ytemp = y + b21*cstep*dydx
    #second step
    ak2 = derivs(x+a2*cstep,ytemp)
    ytemp = y+cstep*(b31*dydx+b32*ak2)
    #third step
    ak3 = derivs(x+a3*cstep,ytemp)
#    ytemp = y+cstep*(b41+dydx+b42*ak2+b43*ak3) <-- i think this is correct
    ytemp = y+cstep*(b41+dydx+b42*ak2+b43*ak3)
    #fourth step
    ak4 = derivs(x+a4*cstep,ytemp)
    ytemp = y+cstep*(b51*dydx+b52*ak2+b53*ak3+b54*ak4)
    #fifth step
    ak5 = derivs(x+a5*cstep,ytemp)
    ytemp = y+cstep*(b61*dydx+b62*ak2+b63*ak3+b64*ak4+b65*ak5)
    #sixth step
    ak6 = derivs(x+a6*cstep,ytemp)
    yout = y+cstep*(c1*dydx+c3*ak3+c4*ak4+c6*ak6)
    # estimate error as difference between fourth and fifth order methods
    yerr = cstep*(dc1*dydx+dc3*ak3+dc4*ak4+dc5*ak5+dc6*ak6)

    return yout, yerr

#
# complex quadrature
#
def complex_quadrature(func, a, b, **kwargs):
    def real_func(x):
        return scipy.real(func(x))
    def imag_func(x):
        return scipy.imag(func(x))
    real_integral = quad(real_func, a, b, **kwargs)
    imag_integral = quad(imag_func, a, b, **kwargs)
    return (real_integral[0] + 1j*imag_integral[0])
```

APPENDIX B

PYTHON CODE FOR MIE SCATTERING

```
import numpy as np
import scipy.special as sp

def specProf(center,linewidth):
    wn1 = center - 10*linewidth
    wn2 = center + 10*linewidth
    step = 0.0001
    wavenumber = np.arange(wn1,wn2,step)
    sigma = linewidth*0.5
    mu = center
    intensity = np.zeros(len(wavenumber))
    for idx,x in enumerate(wavenumber):
        intensity[idx] = 1/(sigma*np.sqrt(2*np.pi))*np.exp(-(x-mu)**2/(2*sigma**2))
    return intensity,wavenumber

def mie_s12(m,x,u):
    """
    Computation of Mie Scattering functions S1 and S2 for ...
    complex refractive index m= m'+im,
    size parameter x=k0*a
    u = cos(scattering angle)
    k0 = vacuum wave number
    a = sphere radius
    """
    nmax = int(np.round(2+x+4*x**(1/3)))

    # get coefficients for amplitude functions s1 & s2
    [an,bn,cn,dn] = mie_abcd(m,x,nmax)

    # get pi & tau coefficients for amplitdue functions s1 & s2
    [pin,taun] = mie_pt(u,nmax)

    n2 = np.zeros(nmax)

    for n in np.arange(1,nmax+1):
        n2[n-1]=(2*n+1)/(n*(n+1))
    pin = np.multiply(n2,pin)
    taun= np.multiply(n2,taun)
    s1 = np.dot(an,pin)+np.dot(bn,taun)
    s2 = np.dot(an,taun)+np.dot(bn,pin)
    return s1,s2

def mie_abcd(m,x,nmax):
    """
    Computes a matrix of Mie Coefficients (an, bn, cn, dn) of orders
    n=1 to nmax
    complex refractive index m= m'+im,
    size parameter x=k0*a
    u = cos(scattering angle)
    k0 = vacuum wave number
```

```
    a = sphere radius
    p. 100, 477 in Bohren and Huffman (1983)
    C. Matzler, June 2002
    """
    n = np.arange(1,nmax+1)
    nu = n+0.5
    z= m*x
    sqx = np.sqrt(0.5*np.pi/x)
    sqz = np.sqrt(0.5*np.pi/z)
    bx = sp.jv(nu,x)*sqx # bessel function of first kind * sqx
    bz = sp.jv(nu,z)*sqz # nu = equation order & x or z = functional domain (array)
    yx = sp.yv(nu,x)*sqx # bessel function of second kind * sqx
    hx = bx+1j*yx
    b1x = np.insert(bx[0:nmax-1],0,np.sin(x)/x)
    b1z = np.insert(bz[0:nmax-1],0,np.sin(z)/z)
    y1x = np.insert(yx[0:nmax-1],0,-np.cos(x)/x)
    h1x = b1x+1j*y1x
    ax = x*b1x-n*bx
    az = z*b1z-n*bz
    ahx = x*h1x-n*hx

    an = ((m*m)*bz*ax-bx*az)/((m*m)*bz*ahx-hx*az)
    bn = (bz*ax-bx*az)/(bz*ahx-hx*az)
    cn = (bx*ahx-hx*ax)/(bz*ahx-hx*az)
    dn = m*(bx*ahx-hx*ax)/((m*m)*bz*ahx-hx*az)
    return an,bn,cn,dn

def mie_pt(u,nmax):
    """
    pin and taun, -1<= u=cos? <= 1, n1 integer from 1 to nmax
    angular functions used in Mie Theory
    Bohren and Huffman (1983), p.94-95
    """
    p = np.zeros(nmax)
    t = np.zeros(nmax)
    p[0] = 1
    t[0] = u
    p[1] = 3*u
    t[1] = 3*np.cos(2*np.arccos(u))
    for n1 in np.arange(3,nmax+1):
        p1 = (2*n1-1)/(n1-1)*p[n1-2]*u
        p2 = n1/(n1-1)*p[n1-3]
        p[n1-1] = p1-p2

        t1 = n1*u*p[n1-1]
        t2 = (n1+1)*p[n1-2]
        t[n1-1] = t1-t2

    return p,t
```

```
def mie_angle_intensity(m,kval,u,x,a):
    """
    Calculates the intensity at an angle theta from the exact Mie scattering
    amplitudes, S(theta), by the formula from van de Hulst. Takes the input
    arguments: m = refractive index, kval = wavenumber [cm-1],
    dia_m = diameter [microns], theta = angle [degrees]
    Uses function mie_s12 by C. Matzler in beginning of function
        complex refractive index m= m'+im,
        size parameter x=k0*a
        u = cos(scattering angle)
        k0 = vacuum wave number
        a = sphere radius
    """
    ### Mie_s12 ###
    nmax = int(np.round(2+x+4*x**(1/3)))

    # get coefficients for amplitude functions s1 & s2
    [an,bn,cn,dn] = mie_abcd(m,x,nmax)

    # get pi & tau coefficients for amplitdue functions s1 & s2
    [pin,taun] = mie_pt(u,nmax)

    n2 = np.zeros(nmax)

    for n in np.arange(1,nmax+1):
        n2[n-1]=(2*n+1)/(n*(n+1))
    pin = np.multiply(n2,pin)
    taun= np.multiply(n2,taun)
    s1 = np.dot(an,pin)+np.dot(bn,taun)
    s2 = np.dot(an,taun)+np.dot(bn,pin)
    ################
    #real Mie scattering
    i1 = np.square(np.abs(s1))
    i2 = np.square(np.abs(s2))
    im = (i1+i2)/(2*kval**2)
    return im,s1,s2
```

APPENDIX C

MATLAB CODE FOR PARTICLE REJECTION FILTER

```
function [imCR] = partRejectfilt2(im,fs,threshold)

% get size of image and create copy
[H,W,~] = size(im);
imCR = im;

% get half of window size (rounded down) for range of application
q = floor(fs/2);
start = 1+q;
finRow = H-q;
finCol = W-q;

% get indices for applying filter and remove those near border
[row, col, ~] = find(imCR > threshold);
r = row > start & row < finRow;
row = row(r); col = col(r);
c = col > start & col < finCol;
row = row(c); col = col(c);

for z = 1:100
    if isempty(row) == 0
        % iterate through indices
        for n = 1:length(row)
            box = imCR(row(n)-q:row(n)+q,col(n)-q:col(n)+q);
            med = median(box(box<threshold));
            if isnan(med) == 1
                continue
            else
                imCR(row(n),col(n),1) = med;
            end
        end
    else
        break
    end
    [row, col, ~] = find(imCR > threshold);
    r = row > start & row < finRow;
    row = row(r); col = col(r);
    c = col > start & col < finCol;
    row = row(c); col = col(c);
end
```